PLANETARY SCIENCE INSTITUTE

(NASA-CR-142085) SMALL BODIES AND THE OUTER PLANETS AND APPENDICES 1 AND 2 Final Report (Planetary Science Inst., Tucson, Ariz.) 163 p HC $6.25 CSCL 03B

N75-17267

Unclas
G3/90 17322

SMALL BODIES AND THE OUTER PLANETS

NASW 2521

Final Report
August, 1974

APPENDICES I, II

Submitted by:

Planetary Science Institute
252 W. Ina Road, Suite D
Tucson, Arizona 85704

William K. Hartmann
Manager

APPENDIX I

Preprint of paper to be submitted to Icarus, entitled:

"Correlations of Asteroid Spectrophotometry with Orbital Parameters"

D. R. Davis

CORRELATIONS OF ASTEROID SPECTROPHOTOMETRY WITH ORBITAL PARAMETERS

D. R. Davis
Planetary Science Institute
Tucson, Arizona 85704

Received_____

No. of Copies: 3

No. of MS Pages: 14

No. of Figures: 11

No. of Tables: 2

Proposed Running Head: ASTEROID SPECTRA AND ORBITS

Names and mailing address of author/person to whom proofs are to be sent:

Dr. Donald R. Davis
Planetary Science Institute
252 W. Ina Road, Suite D
Tucson, Arizona 85704

ABSTRACT

Correlations of asteroid spectral reflectivity characteristics with orbital parameters have been sought. Asteroid proper elements and extreme heliocentric distance were examined. Only general trends were noted, primarily red asteroids and asteroids with IR (.95 μm) absorption bands are concentrated toward the inner part of the belt. Also, asteroids with the pyroxene band tend to have larger proper eccentricities relative to non-banded asteroids.

I. INTRODUCTION

Recently spectrophotometric studies of asteroids have been carried out by several investigators (McCord, Adams, Johnson, 1970; Chapman et al., 1973; McCord and Chapman, 1974). These studies have yielded a wealth of new data concerning the asteroids, much of which is diagnostic of the surface mineralogy of such bodies. Correlations of spectral reflectivity types and possible mineralogical composition with orbital parameters have been sought in previous studies (Chapman, 1971; McCord and Chapman, 1974). Those studies indicate a general but imperfect correlation of spectral type with semimajor axis. In particular redder asteroids appear to have smaller semimajor axes, and asteroids with absorption bands at .95 μm (pyroxene) occur most frequently in the inner part of the belt.

In this study correlations were sought between spectral reflectivity characteristics and the extreme heliocentric distances from the Sun. The correlations noted above with semimajor axes likely reflect variations in the conditions under which the asteroids formed as a function of heliocentric distance since the semimajor axis given is the average distance of the body from the Sun. If indeed it is heliocentric distance that is an important factor in determining mineralogical composition then perhaps the extreme heliocentric distances are significant rather than just the average distance. However the minimum (perihelion) and maximum (aphelion) distances depend

also on the eccentricity and since many asteroids have a significant eccentricity, the aphelion and perihelion distance may be quite different. One complication exists in investigating possible such correlations and that is that the perihelion and aphelion distance undergoes significant perturbations due to the planets, primarily Jupiter and Saturn, whereas the semi-major axis undergoes only very small, periodic perturbations and has been relatively little unchanged in the lifetime of the solar system. The approach used to account for these perturbations in perihelion and aphelion distance is to utilize the results of secular perturbation theory. Secular perturbation theory calculates the long period variation in the orbital elements eccentricity, inclination, longitude of node and longitude of perihelion due to perturbations by other bodies. For our purpose the elements of interest are primarily eccentricity and inclination. Hence the quantities proper eccentricity and proper inclination, which are the eccentricity and inclination with the perturbations arising from forced oscillations due to disturbing bodies removed, are needed. These quantities were calculated and tabulated by Brouwer (1951). In addition to the proper elements, which are constants in secular perturbation theory, the maximum eccentricity is of interest for this parameter and determines the minimum perhilion distance and the maximum aphelion distance of the asteroid. If positional variations are important it might be expected that these extremes of heliocentric distance would correlate with spectral data.

II. NUMERICAL DATA AND CORRELATIONS WITH SPECTRAL DATA

The asteroid spectral reflectivity data and orbital data for the 94 asteroids listed in Table I was used. Column 2 and 3 of Table I give the semimajor axis and current eccentricity of the asteroid orbit, columns 4 and 5 give the proper eccentricity and proper inclination as calculated by Brouwer (1951) with corrections noted by Kiang (1966). Columns 6-8 give the maximum eccentricity calculated from secular perturbation and the corresponding minimum perihelion distance and maximum aphelion distance. Columns 9 and 10 give the R/B color parameter, defined as the ratio of the reflectivity at 0.7 μm to that at 0.4 μm, and the IR band depth, which is the ratio of the reflectivity at the bottom of the band to the highest reflectivity on the short wavelength side of the band.

Figure 1 shows the distribution of colors with semimajor axis. Asteroids with significant pyroxene bands are denoted by open symbols; those without such bands are indicated by filled symbols. The correlation noted earlier, namely towards higher R/B values toward the inner part of the belt, particularly for that subset of asteroids having a significant pyroxene band. For asteroids whose R/B is < 1.25 the mean value of a is 2.74 A.U., for $1.25 \leq R/B < 4.50$, the mean a is 2.66 A.U., for $1.50 \leq R/B < 1.75$, the mean a is 2.57 A.U. and when $R/B > 1.75$ the mean a drops to 2.45 A.U. The mean semimajor axis for those asteroids whose spectral reflectivity curve shows an IR absorption band is 2.58 A.U. whereas for those with no band the mean a is 2.67. This is also reflected

TABLE I. ASTEROID SPECTRAL REFLECTIVITY AND ORBITAL DATA

Asteroid Number	Semimajor Axis(A.U.)	Current Eccentricity	Proper Eccentricity	Proper Inclination	Maximum Eccentricity	Minimum Perihelion Distance (A.U.)	Maximum Aphelion Distance	R/B	IR Band Depth
1	2.77	.079	.111	9.51	.162	2.32	3.22	0.95	-
2	2.77	.237	.255	34.57	.036	1.92	3.62	1.02	-
3	2.67	.257	.229	12.81	.288	1.90	3.44	1.56	0.90
4	2.36	.089	.100	6.38	.156	1.99	2.73	1.33	0.74
5	2.58	.187	.217	4.75	.271	1.88	3.28	1.63	0.84
6	2.43	.203	.170	14.22	.223	1.89	2.97	1.46	0.89
7	2.39	.230	.210	6.36	.266	1.75	3.02	1.64	-
8	2.20	.156	.139	5.68	.211	1.74	2.67	1.79	0.81
9	2.39	.123	.125	4.77	.180	1.96	2.81	1.56	-
10	3.15	.100	.136	5.01	.186	2.57	3.74	1.14	0.89
11	2.45	.102	.072	3.95	.126	2.14	2.76	1.52	-
12	2.34	.219	.193	9.12	.250	1.75	2.92	1.62	-
13	2.58	.085	.274	15.90	.329	1.73	3.42	1.11	-
14	2.59	.164	.196	8.08	.251	1.94	3.24	1.47	(0.83)
15	2.64	.188	.095	12.77	.217	2.07	3.21	1.54	0.93
16	2.92	.135	.100	2.58	.150	2.49	3.36	1.21	-
17	2.47	.138	.138	4.89	.191	2.00	2.94	1.65	(0.92)
18	2.30	.218	.184	10.03	.244	1.74	2.86	1.59	(0.93)
19	2.44	.145	.132	2.20	.185	1.99	2.89	{1.09 {2.26	-
21	2.43	.162	.129	2.18	.183	1.99	2.88	1.14	-
22	2.90	.103	.085	12.71	.134	2.52	3.30	1.24	(0.91)
23	2.62	.236	.258	9.26	.336	1.74	3.50	1.52	?
24	3.14	.121	.157	1.09	.207	2.49	3.79	1.04	-
25	2.40	.255	.230	22.19	.286	1.72	3.09	1.76	0.88
27	2.35	.172	.186	.84	.242	1.78	2.92	1.82	0.88
28	2.78	.153	.173	8.70	.224	2.16	3.40	1.64	(0.88)
29	2.55	.074	.067	6.26	.120	2.25	2.86	1.41	0.93
30	2.37	.127	.104	2.73	.160	1.99	2.74	1.51	-
32	2.59	.082	.114	6.24	.169	2.15	3.02	1.46	?
39	2.77	.112	.074	9.88	.125	2.42	2.86	1.74	0.93
40	2.27	.047	.018	3.67	.081	2.08	2.45	1.65	(0.93)
48	3.11	.060	.071	6.57	.121	2.74	3.50	1.20	-
51	2.37	.066	.105	10.07	.161	1.99	2.75	1.28	-

TABLE I. ASTEROID SPECTRAL REFLECTIVITY AND ORBITAL DATA (cont)

Asteroid Number	Semimajor Axis(A.U.)	Current Eccentricity	Proper Eccentricity	Proper Inclination	Maximum Eccentricity	Minimum Perihelion Distance (A.U.)	Maximum Aphelion Distance	R/B	IR Band Depth
52	3.10	.111	.119	6.47	.168	2.57	3.62	1.07	-
53	2.62	.207	.219	4.57	.282	1.88	3.35	1.22	-
58	2.70	.044	.082	4.73	.135	2.33	3.06	1.10	-
60	2.39	.183	.201	3.95	.256	1.78	3.01	1.54	-
63	2.39	.127	.123	6.07	.178	1.97	2.82	2.07	(0.89)
68	2.78	.185	.150	7.30	.200	2.23	3.34	1.57	-
69	2.98	.166	.183	8.61	.233	2.29	3.67	1.31	(0.79)
79	2.44	.194	.174	5.12	.227	1.89	3.00	1.62	0.92
80	2.30	.200	.159	9.24	.219	1.79	2.80	2.04	-
82	2.76	.220	.249	2.64	.300	1.94	3.59	1.59	(0.91)
84	2.36	.236	.198	9.72	.254	1.76	2.96	1.20	-
85	2.65	.192	.165	12.34	.235	2.03	3.28	1.06	0.90
88	2.77	.162	.142	6.37	.193	2.23	3.30	1.14	-
89	2.55	.180	.149	16.92	.203	2.04	3.07	1.53	0.83
93	2.75	.141	.145	8.66	.196	2.21	3.30	1.19	-
97	2.67	.257	.238	11.38	.296	1.88	3.46	1.12	-
108	3.52	.084	.128	4.88	.178	2.65	3.79	1.61	
115	2.38	.192	.174	12.19	.230	1.83	2.93	1.54	(0.90)
119	2.58	.081	.051	6.20	.105	2.31	2.85	1.74	-
130	3.12	.215	.168	22.08	.218	2.44	3.80	1.12	-
139	2.78	.174	.210	11.02	.260	2.06	3.51	1.15	-
140	2.73	.214	.202	2.14	.253	2.04	3.42	1.29	-
141	2.67	.218	.171	12.77	.230	2.05	3.28	1.16	-
145	2.67	.145	.166	11.58	.223	2.08	3.27	1.19	-
163	2.37	.191	.208	4.69	.264	1.74	2.99	1.19	-
166	2.69	.212	.175	11.07	.230	2.07	3.30	1.44	(0.93)
170	2.55	.063	.078	15.28	.132	2.22	2.89	1.70	-
176	3.17	.181	.146	23.06	.196	2.55	3.79	1.26	-
181	3.12	.214	.210	17.76	.260	2.31	3.93	1.48	(0.82)
192	2.40	.246	.213	7.07	.268	1.76	3.05	1.70	0.93
194	2.62	.239	.215	12.39	.279	1.89	3.34	1.28	-
196	3.11	.013	.045	6.19	.095	2.82	3.41	1.54	-

TABLE I. ASTEROID SPECTRAL REFLECTIVITY AND ORBITAL DATA (cont)

Asteroid Number	Semimajor Axis(A.U.)	Current Eccentricity	Proper Eccentricity	Proper Inclination	Maximum Eccentricity	Minimum Perihelion Distance (A.U.)	Maximum Aphelion Distance	R/B	IR Band Depth
200	2.74	.135	.109	7.66	.161	2.30	3.18	1.07	
210	2.72	.122	.096	4.85	.148	2.32	3.13	1.10	-
213	2.75	.144	.143	5.81	.194	2.22	3.29	1.04	-
221	3.01	.096	.072	10.06	.121	2.65	3.38	1.50	0.91
230	2.38	.061	.034	10.22	.090	2.17	2.60	1.51	-
324	2.69	.336	.299	11.92	.353	1.74	3.64	1.09	-
326	2.32	.189	.183	23.16	.241	1.76	2.88	1.06	-
335	2.47	.180	.162	4.70	.215	1.94	3.00	1.00	-
337	2.38	.137	.153	7.86	.208	1.89	2.88	1.37	-
349	2.92	.090	.054	7.82	.103	2.62	3.22	1.72	0.75
354	2.80	.117	.149	17.63	.199	2.24	3.35	1.89	-
356	2.76	.238	.229	8.53	.279	1.99	3.53	1.34	-
402	2.56	.117	.145	11.08	.199	2.05	3.06	1.36	-
409	2.57	.073	.092	12.19	.146	2.20	2.95	1.25	-
433	1.46	.223	-	-	-	-	-	1.66	(0.94)
446	2.79	.126	.102	9.99	.152	2.36	3.21	2.64	(0.77)
462	2.87	.087	.052	2.06	.102	2.58	3.16	1.62	-
481	2.74	.156	.136	8,89	.187	2.23	3.26	1.24	-
505	2.69	.244	.228	8.71	.282	1.93	3.45	1.08	0.91
511	3.19	.167	.165	14.51	.215	2.51	3.88	1.23	-
532	2.77	.175	.218	15.20	.268	2.03	3.52	1.55	0.93
554	2.38	.153	.147	3.66	.203	1.89	2.86	1.12	-
563	2.71	.237	.216	9.14	.269	1.98	3.44	1.50	?
584	2.37	.234	.197	11.53	.252	1.77	2.97	1.84	?
624	5.12	.025	-	-	-	-	-	1.45	-
654	2.30	.231	.267	18.86	.327	1.55	3.05	1.23	-
674	2.92	.195	.198	12.68	.248	2.20	3.65	1.63	-
704	3.06	.155	.109	18.59	.158	2.57	3.54	1.07	-
714	2.54	.055	.074	15.18	.126	2.22	2.86	1.63	?
739	2.74	.142	.181	15.27	.233	2.10	3.38	1.03	-
887	2.52	.544	.550	8.10	.602	1.00	4.03	1.63	(0.95)
1685	1.37	.436	-	-	-	-	-	1.73	0.84

in a slightly different manner in Table II which shows the number of bodies which have pyroxene bands as a function of R/B value. Here there is an increase in the fraction of bodies with bands from 12% with $R/B < 1.25$ to 63% (although the sample size is only 8 here hence there is a rather large uncertaintiy in this percentage) for $R/B > 1.75$. Hence any correlation with R/B must also correlate with semimajor axis.

There is no reason to anticipate any correlation of reflectivity characteristics with the other orbital parameters of interest, current eccentricity and inclination. These elements undergo perturbations due to other planets and hence are continually changing with time. However correlations might be expected with the proper eccentricity and proper inclination noted above. Figures 2 and 3 show the distribution of asteroids by R/B as a function of proper eccentricity and proper inclination respectively. There is no apparent correlation by R/B type for either inclination or eccentricity when all asteroids are considered. However for that subset which has the IR absorption there is an increased concentration of these at larger values of proper eccentricity. Indeed for the pyroxene band asteroids the mean proper eccentricity is .178 whereas for the non-pyroxene band asteroids the mean eccentricity is .150. When removing 887 Alinda with its very large proper eccentricity of .054 from the pyroxene asteroids still gives a mean proper eccentricity of .165 which is significantly larger than the non-banded values. When the proper inclination is examined for the pyroxene band vs. non-pyroxene band asteroids there is virtually no difference at all.

TABLE II. FRACTION OF ASTEROIDS WITH PYROXENE BAND AS A FUNCTION OF R/B

R/B	Number of Asteroids		Total Number	% With IR Band
	With IR Absorption Band	Without IR Absorption Band		
< 1.25	4	30	34	12
1.25 - 1.50	7	10	17	41
1.50 - 1.75	18	16	34	53
> 1.75	5	3	8	63

The average proper inclination of the former group is .166 (9.54°) and for the latter group is .164 (9.45°).

The extreme heliocentric distances were next examined for possible correlations. Figure 4 shows the distribution of asteroids by color class in aphelion-perihelion space. Asteroids having $R/B < 1.25$ are classified as having a flat reflectivity curve, for $1.25 \leq R/B < 1.50$ the reflectivity curve is called medium and for $R/B \geq 1.50$ the classification is red. From this figure it appears that the flat and medium asteroids are rather uniformly distributed without any obvious correlations, whereas those having a red reflectivity curve appear concentrated toward the smaller perihelion values. To further examine the distribution by reflectivity class, Figures 5-7 show the distribution in perihelion-aphelion space of each of the flat, medium and red distributions. The distinctions noted above are further emphasized in the detailed plots - from Figures 5 and 6 it is apparent that the asteroids with the flat and medium reflectivity curves are indeed uniformly distributed in this space and show no obvious correlation with either the extreme perihelion or aphelion distance. From Figure 7 however, the increased concentration of asteroids toward the smaller perihelion values is obvious. The numerical distribution of red vs. non-red asteroids is depicted in Figures 8 and 9 which gives histograms of the number of asteroids as a function of minimum perihelion distance. The red asteroids are depleted relative to the non-red for perihelion distances greater than about 2.2 A.U. and are somewhat enhanced,

particularly in the region from 1.7 - 1.8 A.U. The non-red asteroids show a more or less uniform distribution in minimum perihelion distance while the red ones show an increasing concentration toward the smaller perihelion distances. These figures should be treated with some caution however, as the statistics are relatively small, i.e. only a total of 42 red and 50 non-red in the entire histogram, however the trends do seem real. When the subset of asteroids with the IR absorption band is considered, there are too few such bodies for any meaningful comparison in the flat and medium classes although the few that are there appear unduly scattered. For the red group, there is a further concentration toward the small perihelion values. Of the red asteroids, those with pyroxene absorption bands have a mean minimum perihelion distance of 1.98 A.U. while those without such a band have a mean perihelion distance of 2.15 A.U. Similar plots for maximum aphelion distance, Figures 10 and 11, yield a very similar distribution for both red and non-red asteroids.

It is intriguing that the flat asteroids have an apparent cutoff (i.e. the smallest maximum aphelion distance) at $\sim$ 2.85 A. U., the medium asteroids show a cutoff at $\sim$ 2.70 A.U., whereas for the red bodies the cutoff is at $\sim$ 2.45 A.U. This observation is the only trend in the data with regard to aphelion distance noted so far.

III. DISCUSSION

The only correlations noted, which are primarily general trends rather than absolute correlations, are primarily with the concentration of red asteroids and asteroids with pyroxene bands toward the inner part of the solar system. This correlation appears with both semimajor axes and minimum perihelion distance (which are not independent parameters). A somewhat more tenuous correlation exists with proper eccentricity when the pyroxene band asteroids are considered alone. The primary observation regarding the correlations or lack thereof is to understand why they are so imperfect. Even if asteroids were homogeneously formed, which by no means is necessarily the case, there would be mixing subsequent to formation. This mixing arises from two sources:

(1) mixing by gravitational perturbations

(2) collisional mixing.

Unquestionably collisions have and are taking place in the asteroid belt, however it is doubtful that such collisions would significantly alter the orbits of the bodies. The energies required for orbital changes are generally such that the body is disrupted long before the orbit is changed by very much.

Gravitational mixing could arise from two mechanisms:

(1) perturbations due to mutual interactions, i.e. close orbital encounters, etc.

(2) perturbations by planets, primarily Jupiter.

It is difficult to see how the first mechanism leads to appreciable mixing if the mass in the belt was approximately the same as the mass of the current belt. The orbital change due to a close encounter with Ceres, the largest asteroid, is such that many such encounters all acting in the same sense would be required for large changes. Hence the mechanism looks unpromising. Gravitational mixing arising from Jupiter perturbations could produce large changes. Lecar and Franklin (1973) address the evolution of an initially uniform distribution of asteroids due to Jupiter's gravitational perturbation and found that the outer part of the initial belt, lay at distances greater than 3.3 A.U. In particular asteroids in the outer regions of the initial belt 73.3 A.U. are either driven to stable orbits further in or approach Jupiter closely and are ejected from the asteroid domain. Possibly then the medium and flat asteroids were formed in the outer part of the belt and subsequent perturbations by Jupiter were sufficient to mix these bodies more uniformly throughout the belt whereas the red- and pyroxene-band asteroids were originally formed in the inner part of the belt where perturbations are relatively weak and hence less mixing would be expected.

In conclusion, it is noted that no strong correlations were found between spectral parameters and orbital characteristics; there is a general correlation of red asteroids and asteroids with pyroxene bands to be concentrated in the inner part of the current belt and a possible correlation of pyroxene-banded asteroids with larger values of proper eccentricity.

REFERENCES

Brouwer, D. (1951) Secular Variations of the Orbital Elements of Minor Planets, Astron. J. 56, 9.

Chapman, C. R. (1971) Ph.D thesis, Massachusetts Institute of Technology.

Chapman, C., T. McCord and T. Johnson, (1973) Asteroid Spectral Reflectivities, Astron. J. 78, 126.

Kiang, T. (1966) Bias Free Statistics of Orbital Elements of Asteroids, Icarus 5, 437.

Lecar, M. and F. A. Franklin (1973) On the Original Distribution of Asteroids. I., Icarus 20, 4, 422.

McCord, T., J. Adams and T. Johnson (1970) Asteroid Vesta: Spectral Reflectivity and Compositional Implications, Science 168, 1445.

McCord, T. and C. Chapman (1974) Asteroids: Spectral Reflectance and Color Characteristics, Ap.J. (in press).

FIGURE CAPTIONS

Figure 1. Color parameter R/B as a function of semi-major axis. Filled symbols denote asteroids with significant IR ($\sim .95\,\mu m$) absorption bands.

Figure 2. Color parameter R/B as a function of proper eccentricity of the asteroids.

Figure 3. Color parameter R/B as a function of proper eccentricity.

Figure 4. Asteroid color distribution as a function of maximum aphelion distance and minimum perihelion distance.

Figure 5. Asteroids with flat spectral reflectivities as a function of aphelion-perihelion distance.

Figure 6. Asteroids with medium spectral reflectivities as a function of aphelion-perihelion distance.

Figure 7. Asteroids with red spectral reflectivities as a function of aphelion-perihelion distance.

Figure 8. Number histogram of red asteroids as a function of minimum perihelion distance.

Figure 9. Number histogram of non-red asteroids as a function of minimum perihelion distance.

Figure 10. Number histogram of red asteroids as a function of maximum aphelion distance.

Figure 11. Number histogram of non-red asteroids as a function of maximum aphelion distance.

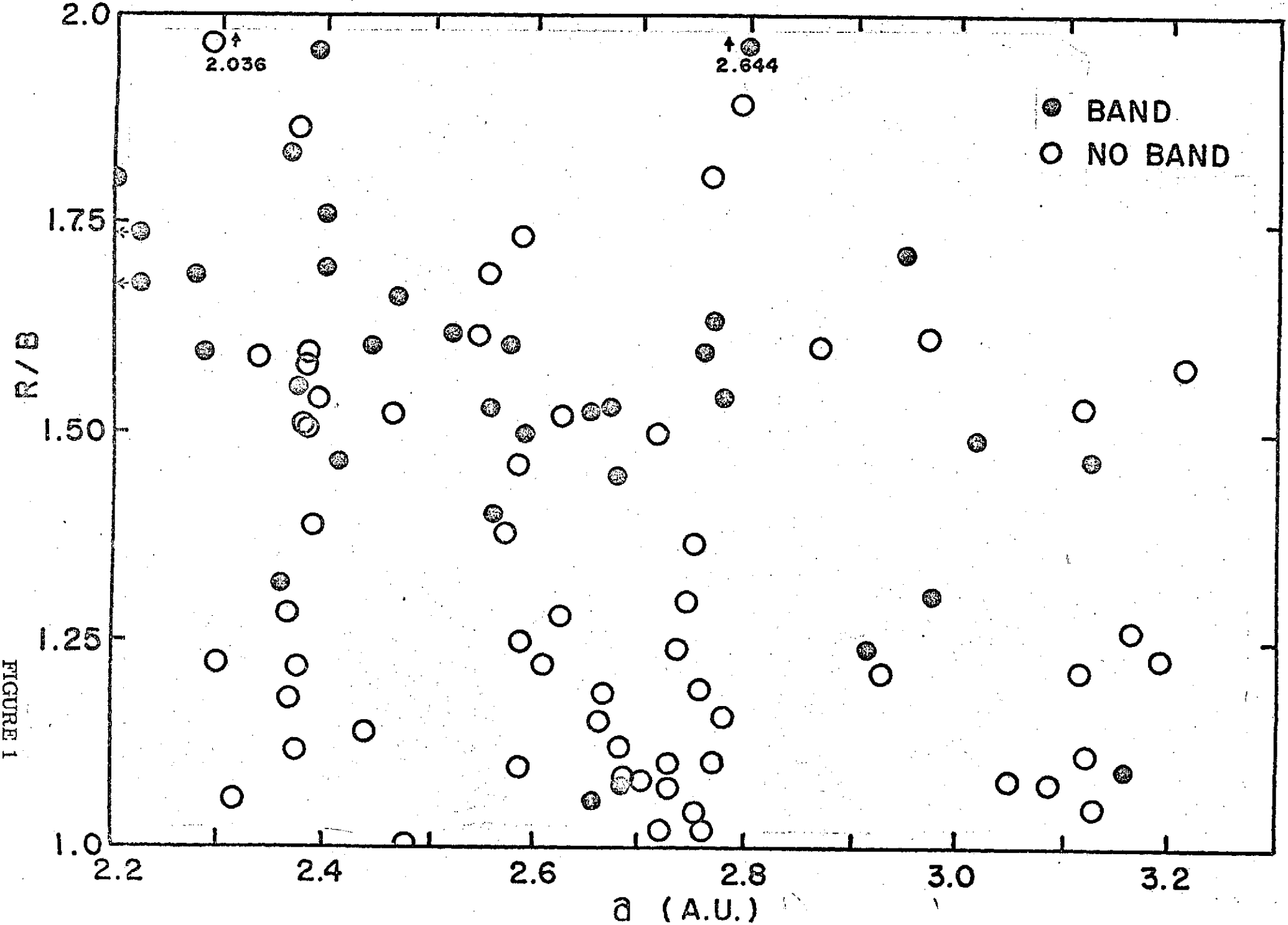

FIGURE 1

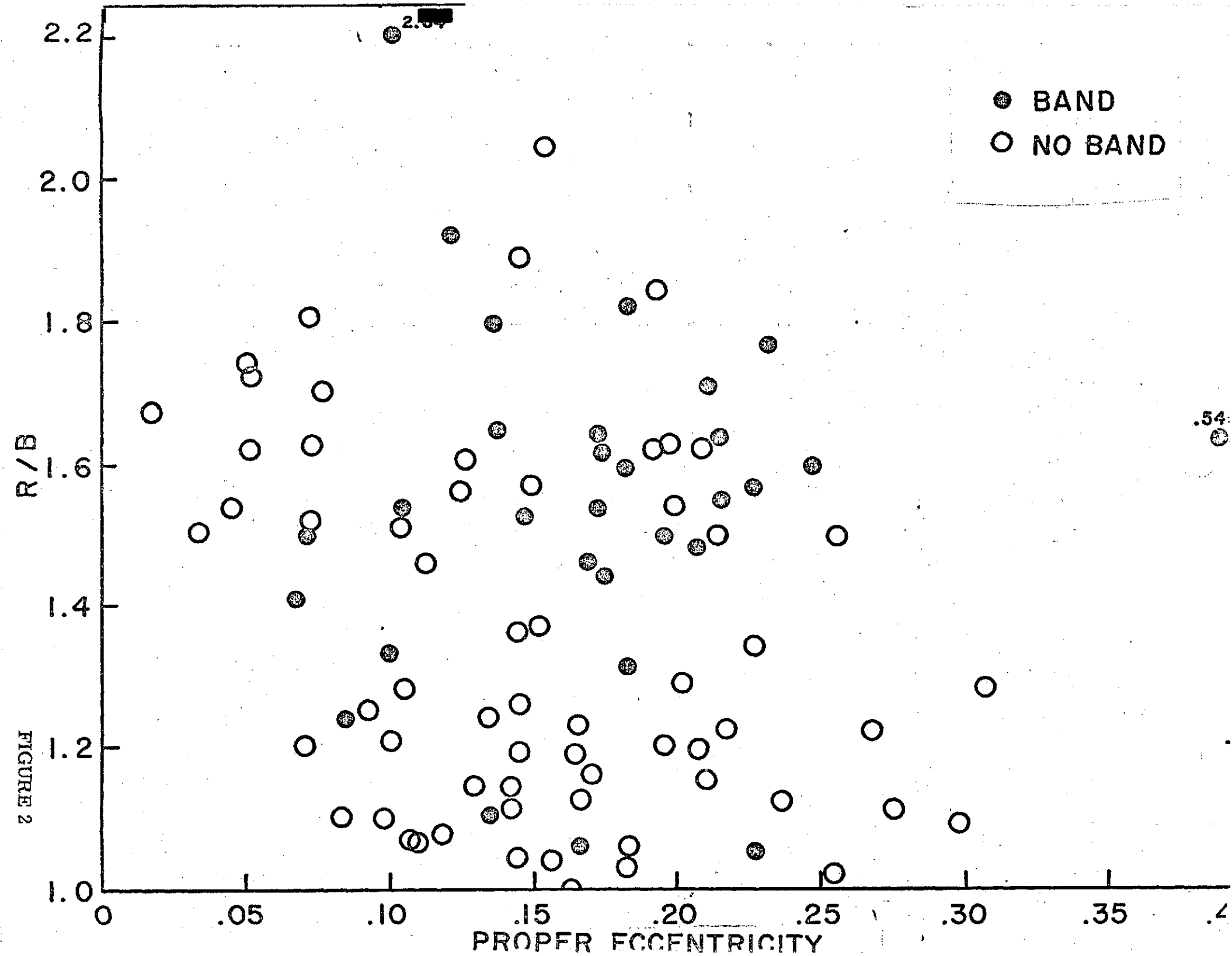
BAND
NO BAND
R / B
2.2
2.0
1.8
1.6
1.4
1.2
1.0
.54
0
.05
.10
.15
.20
.25
.30
.35
PROPER ECCENTRICITY

FIGURE 2

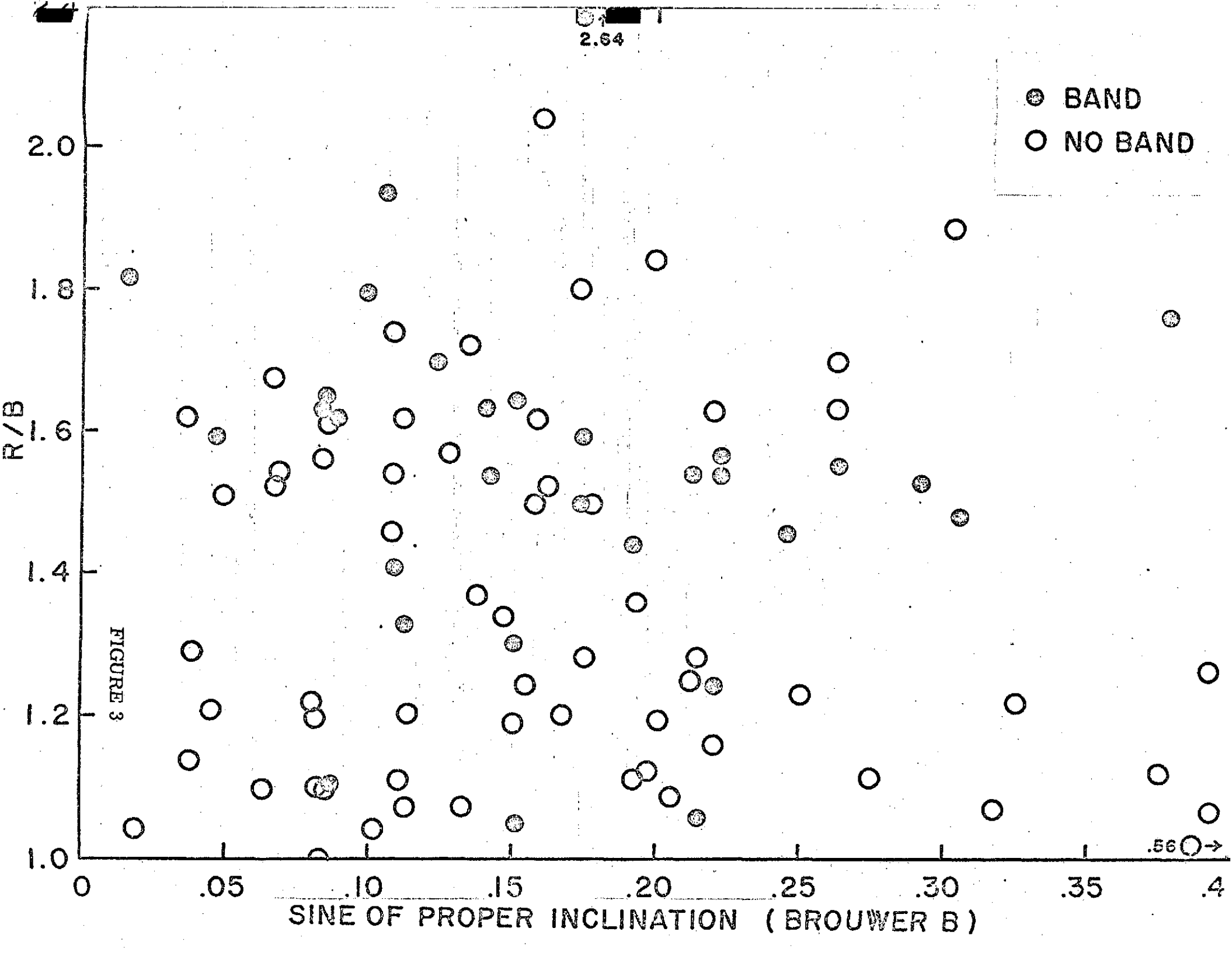
2.64
BAND
NO BAND
2.0
1.8
1.6
1.4
1.2
1.0
R/B
.56
0
.05
.10
.15
.20
.25
.30
.35
.4
SINE OF PROPER INCLINATION (BROUWER B)

FIGURE 3

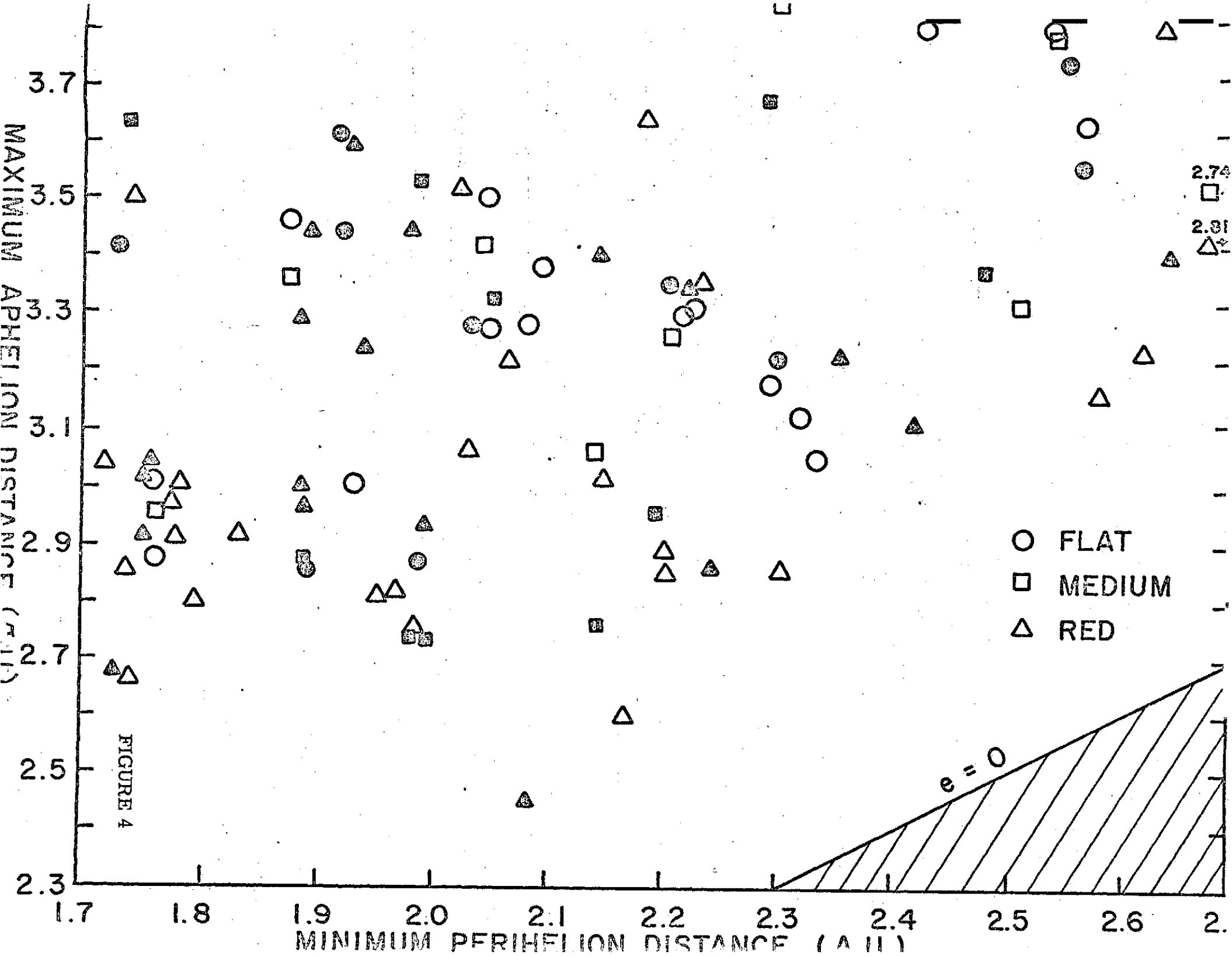
MAXIMUM APHELION DISTANCE (A.U.)
3.7
3.5
3.3
3.1
2.9
2.7
2.5
2.3
1.7
1.8
1.9
2.0
2.1
2.2
2.3
2.4
2.5
2.6
2.
MINIMUM PERIHELION DISTANCE (A.U.)
2.74
2.31
FLAT
MEDIUM
RED
e = 0

FIGURE 4

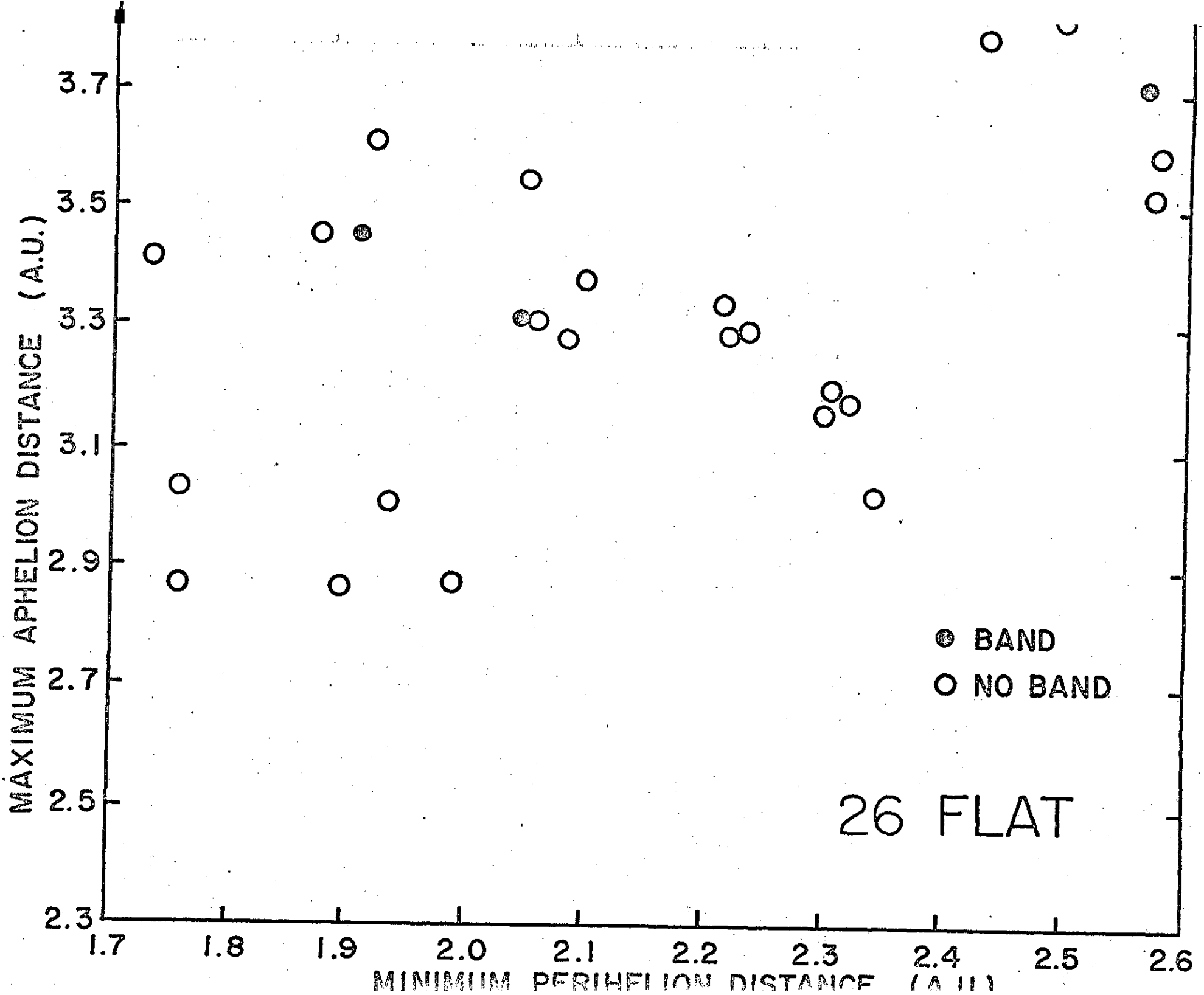
MAXIMUM APHELION DISTANCE (A.U.)
3.7
3.5
3.3
3.1
2.9
2.7
2.5
2.3
1.7
1.8
1.9
2.0
2.1
2.2
2.3
2.4
2.5
2.6
MINIMUM PERIHELION DISTANCE (A.U.)
BAND
NO BAND
26 FLAT

FIGURE 5

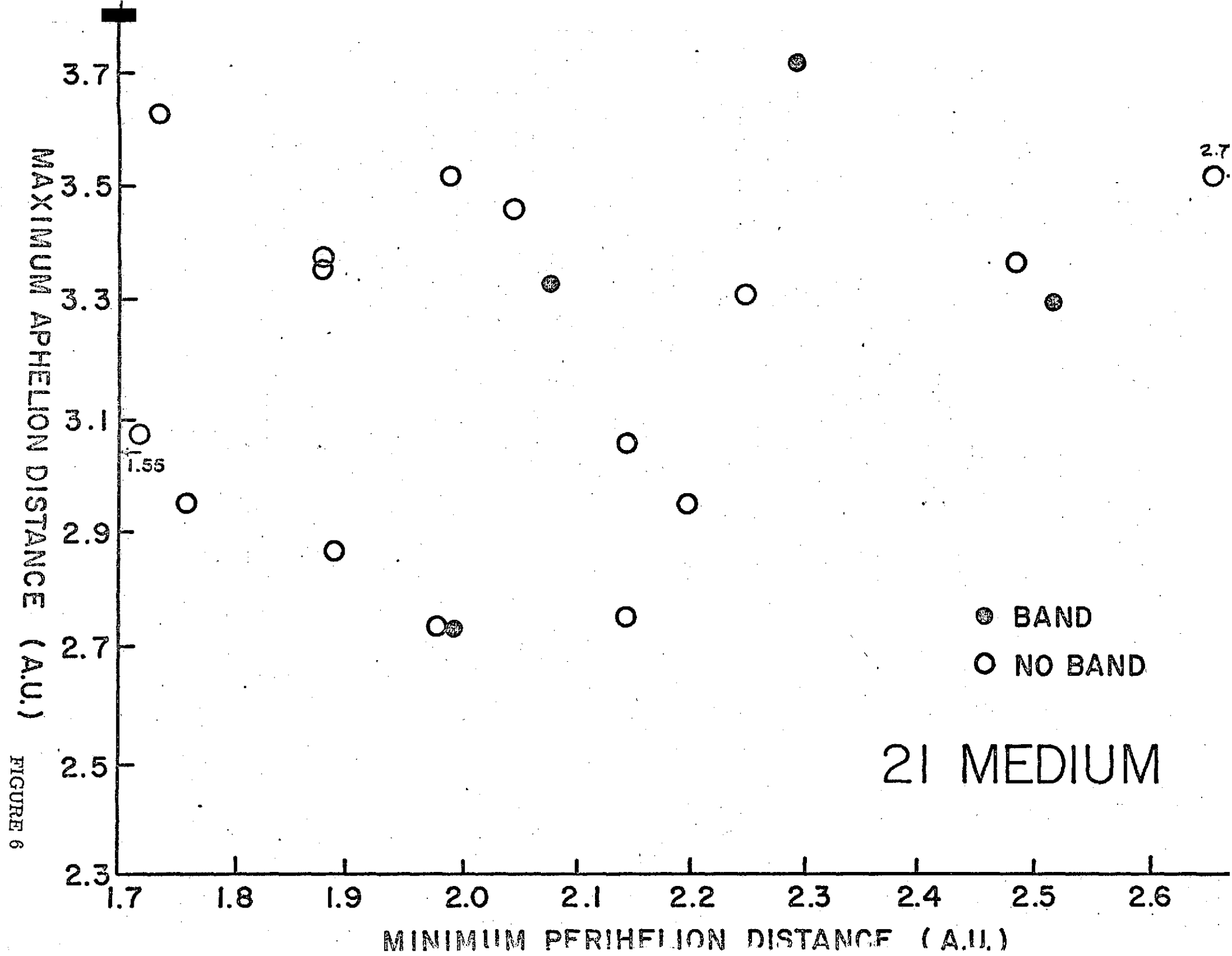
MAXIMUM APHELION DISTANCE (A.U.)
3.7
3.5
3.3
3.1
2.9
2.7
2.5
2.3
1.55
2.7
1.7
1.8
1.9
2.0
2.1
2.2
2.3
2.4
2.5
2.6
MINIMUM PERIHELION DISTANCE (A.U.)
BAND
NO BAND
21 MEDIUM

FIGURE 6

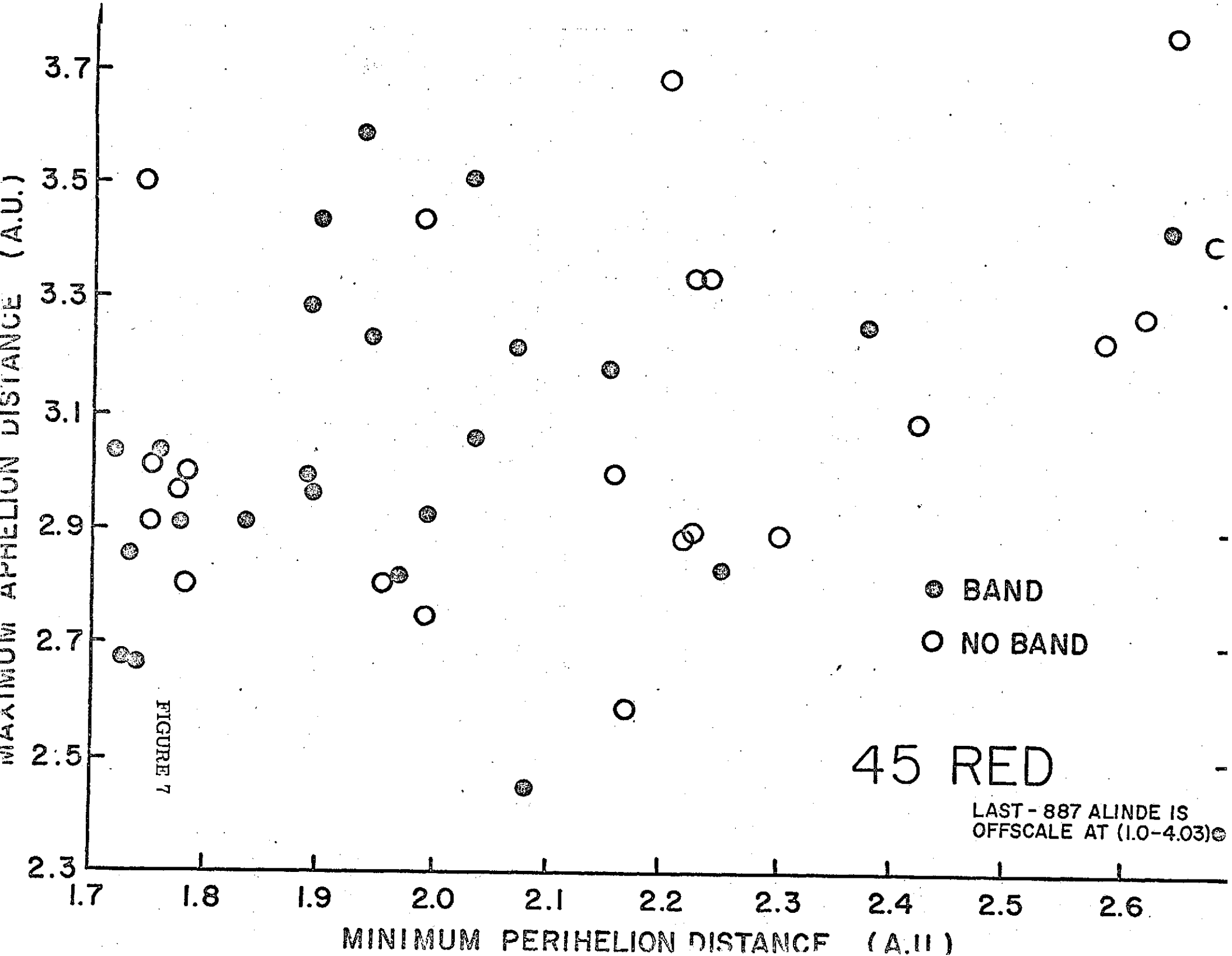
MAXIMUM APHELION DISTANCE (A.U.)
3.7
3.5
3.3
3.1
2.9
2.7
2.5
2.3
1.7
1.8
1.9
2.0
2.1
2.2
2.3
2.4
2.5
2.6
MINIMUM PERIHELION DISTANCE (A.U.)
BAND
NO BAND
45 RED
LAST - 887 ALINDE IS OFFSCALE AT (1.0-4.03)

FIGURE 7

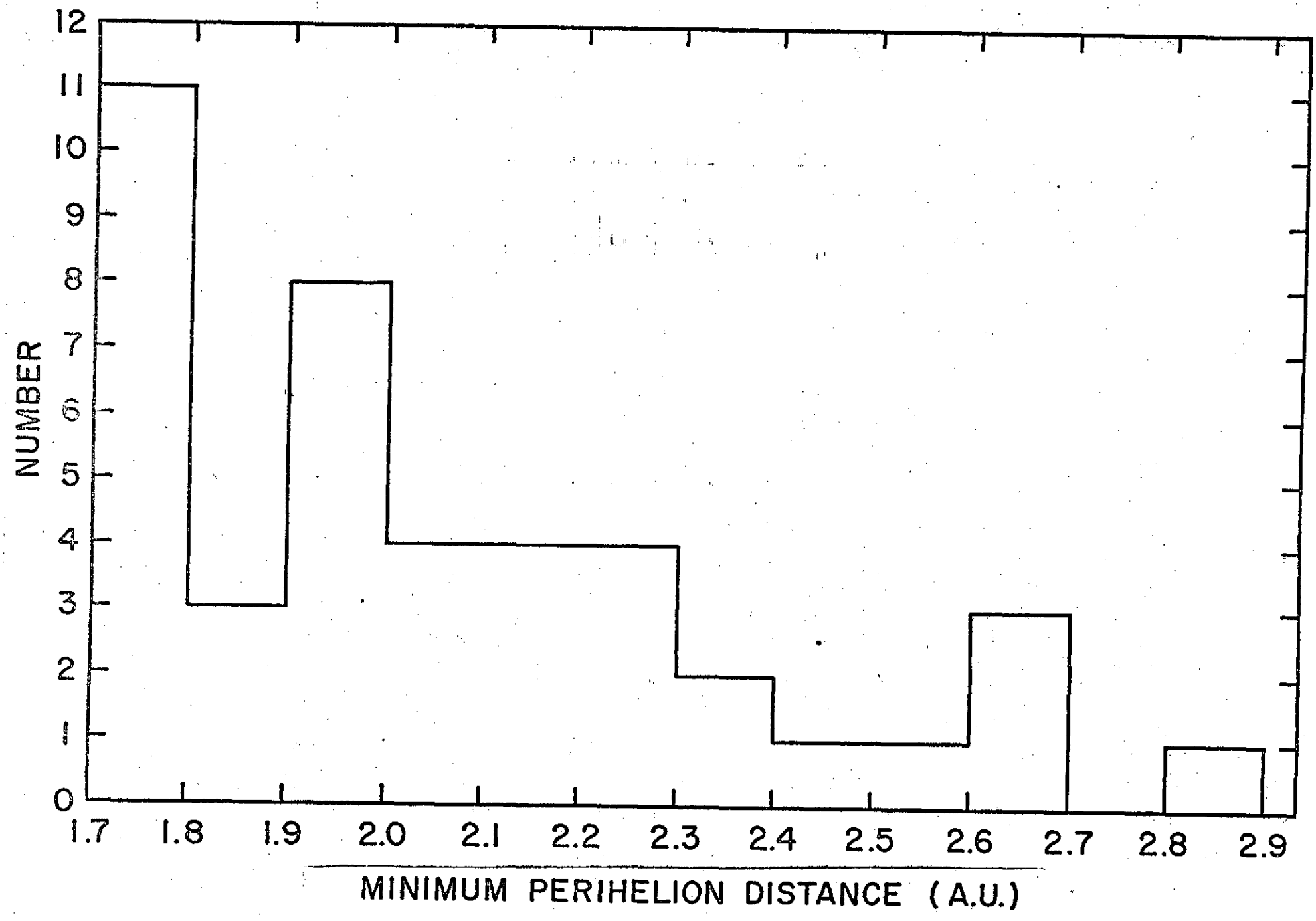
NUMBER
0
1
2
3
4
5
6
7
8
9
10
11
12
1.7
1.8
1.9
2.0
2.1
2.2
2.3
2.4
2.5
2.6
2.7
2.8
2.9
MINIMUM PERIHELION DISTANCE (A.U.)

FIGURE 8

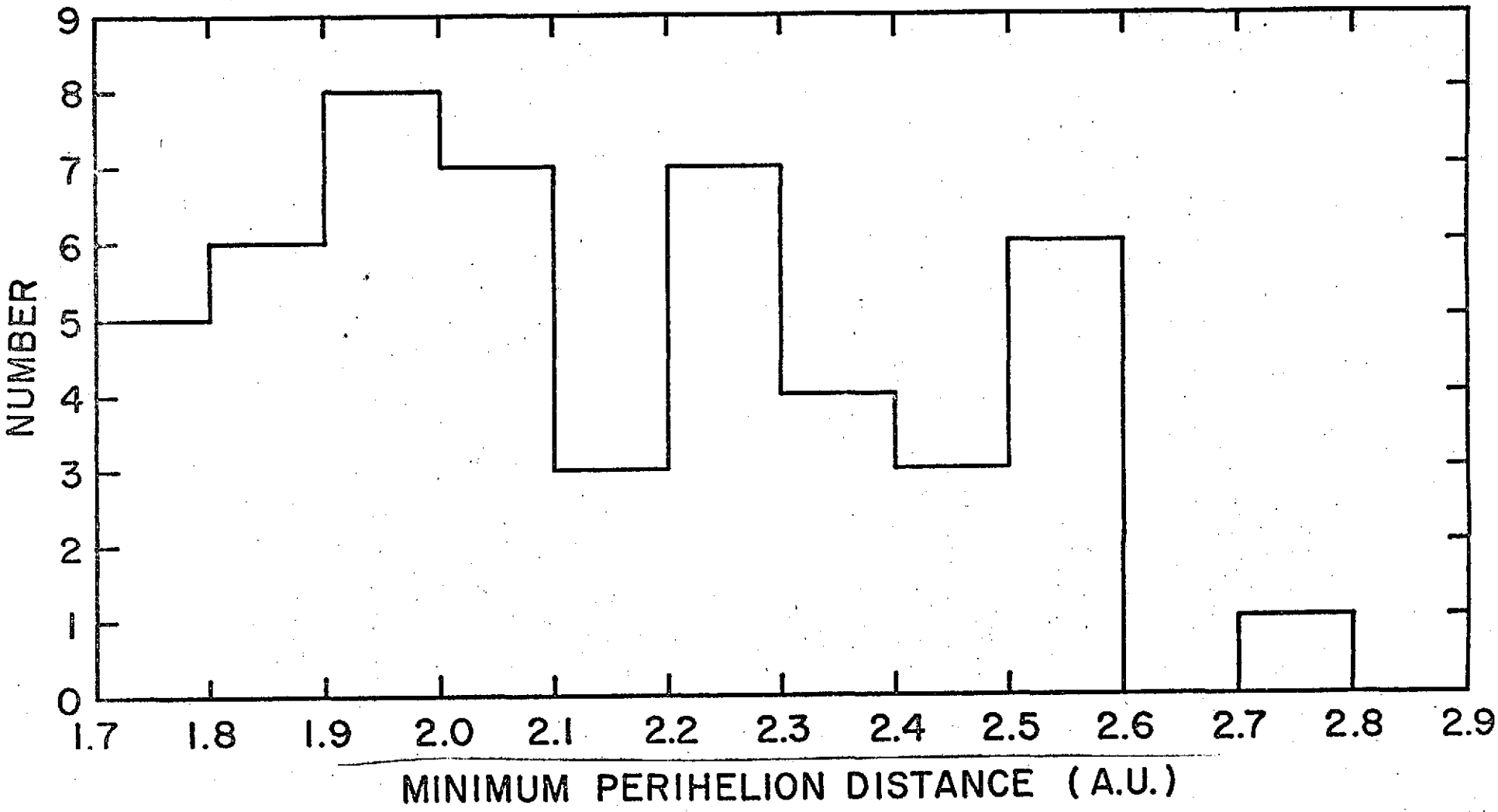
NUMBER
0
1
2
3
4
5
6
7
8
9
1.7
1.8
1.9
2.0
2.1
2.2
2.3
2.4
2.5
2.6
2.7
2.8
2.9
MINIMUM PERIHELION DISTANCE (A.U.)

FIGURE 9

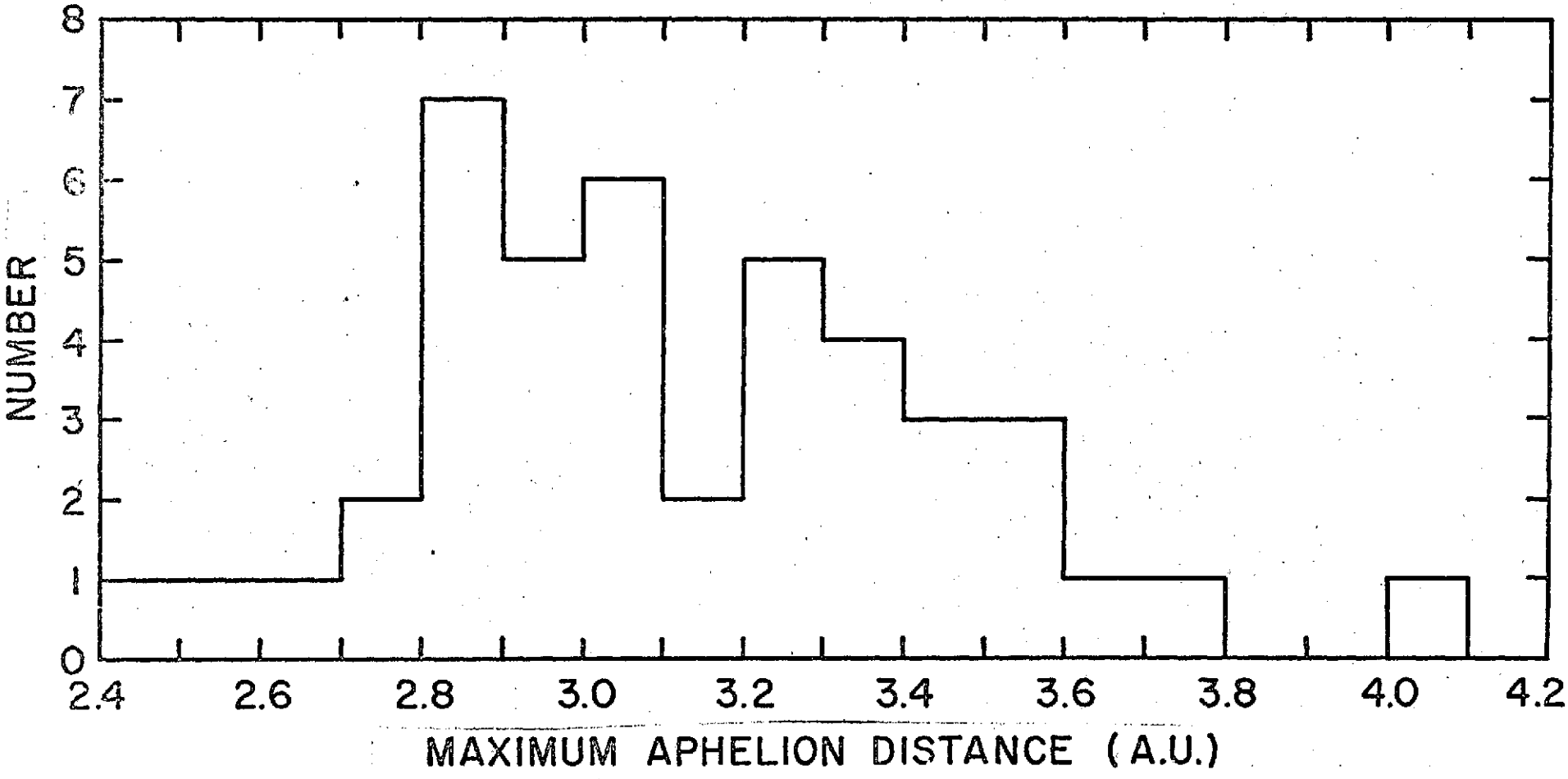
NUMBER
0
1
2
3
4
5
6
7
8
2.4
2.6
2.8
3.0
3.2
3.4
3.6
3.8
4.0
4.2
MAXIMUM APHELION DISTANCE (A.U.)

FIGURE 10

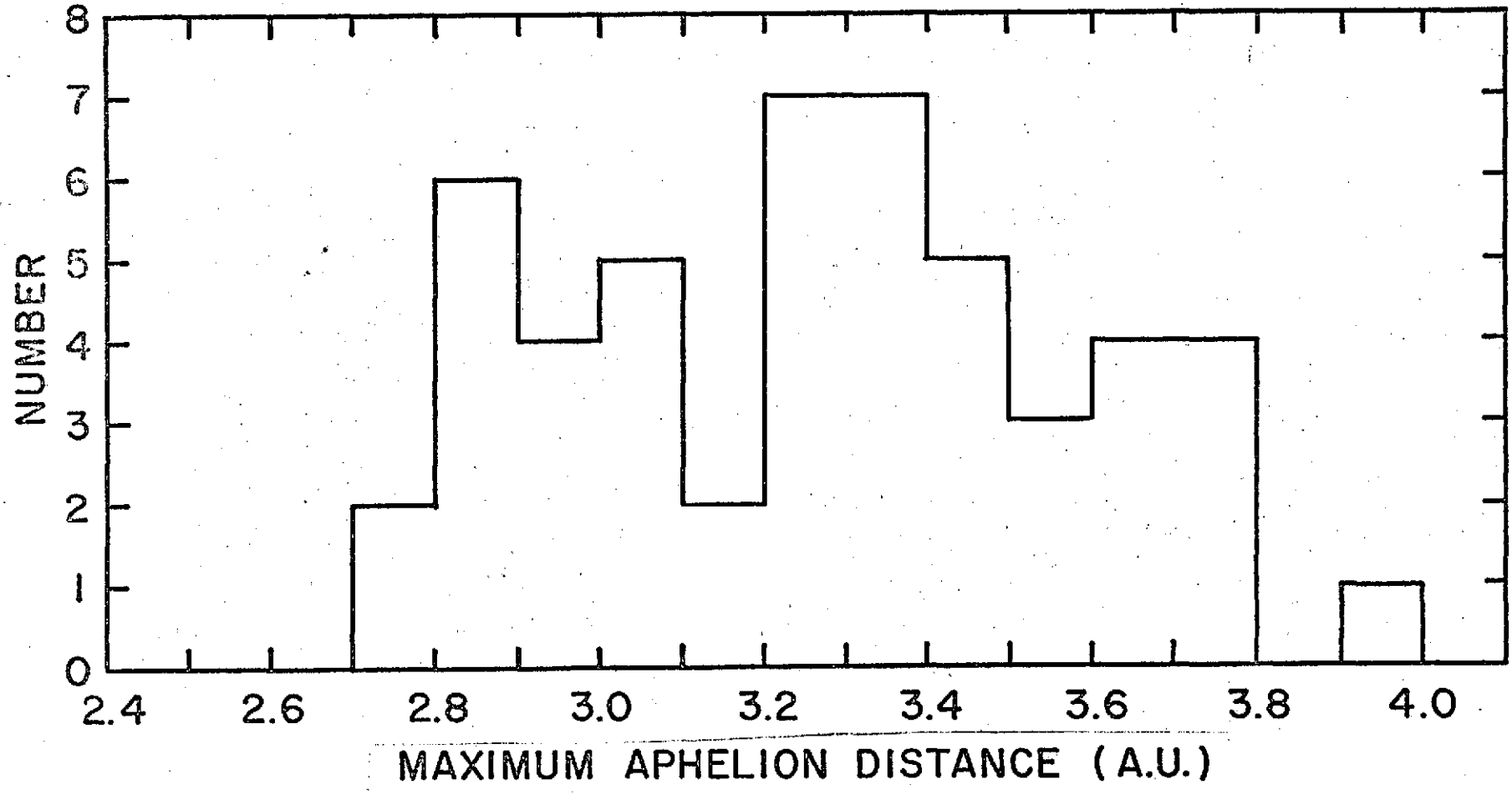
NUMBER
0
1
2
3
4
5
6
7
8
2.4
2.6
2.8
3.0
3.2
3.4
3.6
3.8
4.0
MAXIMUM APHELION DISTANCE (A.U.)

FIGURE 11

APPENDIX II

Preprints of papers to be submitted to Icarus, entitled:

1. "Optical Scattering Properties of Saturn's Ring.II."

2. "Saturn's Ring and Pioneer 11."

3. "Indirect Illumination of Saturn's Ring via the Ball of the Planet. I. Detection."

M. J. Price

OPTICAL SCATTERING PROPERTIES OF SATURN'S RING. II.

Michael J. Price
Planetary Science Institute
Tucson, Arizona 85704

Received _____

Revised _____

No. of Copies: 4
No. of MS Pages: 22
No. of Figures: 9
No. of Tables: 0

Proposed Running Head: SATURN'S RING

Name and address of author/person to whom proofs are to be sent:

Dr. Michael J. Price
Planetary Science Institute
252 W. Ina Road, Suite D
Tucson, Arizona 85704

ABSTRACT

Further analysis of visual (V) wavelength photometric function data for Saturn's ring is presented. Evidence indicating both that primary scattering dominates, and that mutual shadowing is an irrelevant concept, is reviewed. Simple anisotropic scattering radiative transfer models are used to define the probable ranges in the single scattering albedo, and in the general shape of the scattering phase function of the individual particles. Limitations on the mean perpendicular optical thickness of the ring are also obtained. Results indicate that the ring particles are highly efficient back-scatterers of visual radiation. Macroscopic particles account for the basic shape of the scattering phase function. Based on an infinite optical thickness for the ring, a minimum single scattering albedo ~ 0.75 is found. Use of conservative scattering leads to a minimum optical thickness ~ 0.7. The analysis is consistent with the ring particles being centimeter-size pieces of ice.

1. INTRODUCTION

In Paper I, Price (1973) rediscussed the optical scattering properties of the Saturn ring system. Reliable data defining its photometric function at visual wavelengths were interpreted in terms of a simple scattering model. The ring model adopted was a plane-parallel slab of isotropically scattering particles; the single scattering albedo and the perpendicular optical thickness were both arbitrary. Results indicated that primary scattering is inadequate to describe the photometric properties of the ring; multiple scattering was found to predominate for all angles of tilt with respect to the Sun and Earth. In addition, the scattering phase function of the individual particles is significantly anisotropic; they must scatter preferentially towards the Sun. Minimum values for the single scattering albedo, and for the mean perpendicular optical thickness (rings A and B together) appeared to be 0.9 and unity respectively. It was concluded that thorough interpretation of ring photometry in terms of the physical structure of the system would be highly problematic requiring the solution of a complex radiative transfer problem.

Further analysis of the photometric function data is presented in this paper. The conclusions reached in Paper I are rediscussed on the basis of more realistic scattering models for the ring. First, the relevance of the mutual shadowing concept is examined. Observational evidence, indicating that mutual shadowing is negligible, is presented. Additional evidence, indicating that primary scattering must predominate, is reviewed.

Simple anisotropic scattering radiative transfer models for the ring are then introduced. By comparing theoretical predictions of the photometric function with observation, limitations are set on the probable ranges in the single scattering albedo, in the mean perpendicular optical thickness, and in the shape of the scattering phase function for the individual particles. The paper continues with an investigation of the relative importance of primary and multiple scattering in defining the photometric properties of the ring. By imposing the condition that primary scattering must predominate, additional constraints are placed on the basic radiative transfer parameters of the ring. Finally, the physical nature of the ring particles is discussed with reference to the results.

2. IS THE CONCEPT OF MUTUAL SHADOWING RELEVANT?

Nearly 100 years ago, the Saturn ring system was discovered to exhibit a pronounced phase effect, the rings brightening dramatically near opposition. Traditionally, the phase effect has been interpreted in terms of mutual shadowing among macroscopic ring particles. Some interpretations have been attempted using the Mie theory of scattering, the small particles being either located individually within the ring or attached to the surfaces of much larger bodies. Other explanations have also been made in terms of shadowing within rough surface layers of macroscopic particles. But, over the years, the concept of mutual shadowing has entirely dominated photometric studies of the ring. Indeed, it has become axiomatic that the individual particles must be sufficiently close together for significant mutual shadowing to occur.

Evidence exists, however, to suggest that mutual shadowing is in fact negligible. While analyzing two-color (B, V) phase curves for both the A and B components of Saturn's ring, Franklin and Cook (1965) drew attention to a peculiar observational fact. In spite of the wide disparity in the surface brightness (x2) for rings A and B, their phase effects in either blue or visual light are identical. Assuming that surface brightness is directly related to optical thickness (τ) and that the particle radius (r) is constant throughout the ring, Franklin and Cook (1965) derived an interpretation based on the mutual shadowing phenomenon. Their mathematical expressions for the phase effect contained both the volume density (D), and the optical thickness (τ). Although τ and D were strongly coupled, they were not linearly related. Nevertheless, in order to explain the invariant phase effect, optical thickness and volume density had to be precisely, and inversely, coupled everywhere in the ring system. Corresponding changes in the ring thickness (z) were required since the basic ring parameters are related through the equation

$$z = \frac{4}{3} \; r \; \tau/D \quad . \tag{1}$$

Such a unique situation is so unlikely to occur naturally that the concept of mutual shadowing must be considered highly artificial.

If the concept of mutual shadowing is abandoned, a simpler explanation for the invariant phase effect can be introduced; the phase effect is nothing more than the scattering phase function of the individual ring particles. That the effect is an intrinsic property of the individual particles is also suggested by its color-dependence discovered by Franklin and Cook (1965). Two constraints

are placed on the ring model by our new working hypothesis. First, the physical nature of the particles must be identical throughout the ring. Supporting evidence comes from UV-IR spectrophotometric studies by Lebofsky, Johnson, and McCord (1970); spectral reflectivity curves for rings A and B closely match. Second, primary scattering must predominate in order to retain the basic signature of the scattering phase function. Either the ring particles back-scatter solar radiation so efficiently that multiple scattering is always negligible, or the single scattering albedo is low, or the ring system is everywhere optically thin. Indeed, the monolayer ring model (Jeffreys, 1947) might well be valid.

Discarding the idea of mutual shadowing is not inconsistent with current knowledge of the ring parameters. For mutual shadowing to produce a negligible phase effect, the volume density must be less than $\sim 10^{-3}$ (Bobrov, 1970). For comparison, the actual volume density can be estimated from equation (1). Pollack, Summers, and Baldwin (1973) have provided a comprehensive discussion of current estimates for the particle dimensions. Several observational techniques suggest a mean particle radius ~ 1 cm. Focas and Dollfus (1969) have obtained a physical thickness for the ring ~ 3 kms. For an optical thickness ~ 1, the corresponding volume density is 4.5×10^{-6}; interparticle separations must necessarily be large (i.e. ~ 120 radii). Bear in mind that particle radii ~ 1 meter (Goldstein and Morris, 1973) can also be tolerated before interparticle distances become small, and mutual shadowing becomes significant.

3. RADIATIVE TRANSFER RING MODELS

Adopting the working hypothesis that mutual shadowing is negligible greatly simplifies the radiative transfer problem cf: Irvine (1966). Derived interparticle distances are sufficiently large that each particle may be considered to be in the far field of its neighbors. The classical theory for multiple scattering may therefore be applied. Our ring model is a homogeneous, plane-parallel, layer of anisotropic scattering particles illuminated by a parallel beam of solar radiation. It will be completely described by three basic radiative transfer parameters: single scattering albedo, anisotropy parameter, and optical thickness.

To begin exploring the anisotropic scattering properties of the individual particles, an elementary general phase function, $p(\textcircled{H})$ will be utilized. Its mathematical form is given by

$$p(\textcircled{H}) = \tilde{\omega}(1 + x\cos\textcircled{H}), \quad 0 \leq \tilde{\omega} \leq 1, \quad -1 \leq x \leq 1, \qquad (2)$$

where $\textcircled{H}$ is the scattering angle, $\tilde{\omega}$ is the single scattering albedo, and x is the anisotropy parameter. By varying the anisotropy parameter through the range $-1 \leq x \leq 1$, a wide variety of scattering phase functions can be investigated. Extremes range from predominant back-scattering ($x = -1$), through isotropic ($x = 0$), to pronounced forward scattering ($x = 1$). In the back-scattering ($x = -1$) case, the phase function is equivalent to the far field of a macroscopic sphere for which the intensity of radiation scattered in a given direction is proportional to the apparent area illuminated. Examples of the scattering phase function for two x-values, $\tilde{\omega}$ being constant, are shown

in Fig. 1. For comparison, the Lambert case is also shown. If the macroscopic sphere had a Lambert scattering surface, the phase function can be readily shown to be

$$p(\Theta) = \frac{8\tilde{\omega}}{3\pi}\left\{\sin\Theta \cdot \cos^2\Theta - \Theta \cdot \cos\Theta + \sin^3\Theta\right\} . \qquad (3)$$

The major features of the Lambert case are described by the general phase function ($x = -1$). Bear in mind, however, that the real phase function might be a good deal more asymmetric than the extreme cases permitted by our elementary function.

Analytical solutions of the classic radiative transfer problem, involving the general scattering phase function, have been obtained by Chandrasekhar (1960); both finite and semi-infinite cases have been studied. His expressions for diffuse reflection may be readily evaluated provided that the relevant X-, Y- and H- functions are known. But general tabulations do not exist since their exact computation is a non-trivial numerical problem. Fortunately, however, high accuracy is not required in our exploratory investigation. Approximate computational techniques recommended by Chandrasekhar (1960) were therefore used. The H-functions were derived from the roots of the relevant characteristic equation in the fourth approximation. The X-, Y- functions were determined using the iterative technique for small optical thickness with subsequent second-trial correction. For single scattering albedos in the range $0.4 \leq \tilde{\omega} \leq 1$, the H-functions can be evaluated to an accuracy ~ 1 percent or better. So can the X-, Y- functions, provided the optical thickness lies in the range $0 \leq \tau \leq 1$. The primary scattering contribution to the intensity of radiation diffusely reflected from the ring can be readily calculated by

generalizing the treatment by Chandrasekhar (1960) for the isotropic scattering case.

4. THE PHOTOMETRIC FUNCTION: OBSERVATION AND THEORY

Price (1973) has reviewed the observational data defining the photometric function of the ring at visual wavelengths. Brief studies have been made of the variation in the surface brightness with both phase angle and solar declination angle. But no reliable information exists concerning variation in the phase effect with ring tilt. Current knowledge of the visual photometric function of the system (rings A and B together) is summarized in Fig. 2. Information on the phase effect is derived from Franklin and Cook (1965) taking into account the important errata discussed by Cook, Franklin and Palluconi (1971). Tilt effect data are taken from Price (1973).

Our general phase function (Fig. 1) cannot explain the opposition surge in the phase curve; it is too strongly peaked. Most probably, the opposition "pip" results from microshadowing within the surfaces of the individual particles (Oetking, 1966; Hapke, 1966). Very likely the surfaces are quite irregular. Otherwise, the opposition effect would probably be smaller than observed, especially if the surfaces are highly reflective(Bobrov, 1970). Accordingly, the effect is treated as a perturbation to the phase function, atypical of the overall scattering properties of the ring particles. Our analysis will concentrate on the coarser features of the photometric function to define the anisotropy parameter. Photometry at phase angles greater than 1.5 degrees will provide the base. Individual limitations on the single

scattering albedo, on the optical thickness, and on the shape of the scattering phase function may be obtained by comparing theoretical predictions of the photometric function with observation. Their limited combinations can also be found.

For the single scattering albedo, its minimum value can be obtained by considering the case for maximum back-scattering ($x = -1$) and maximum optical thickness ($\tau = \infty$). Predicted photometric functions for single scattering albedos in the range $0.4 \leq \varpi \leq 1$ are shown in Fig. 3. Required geometrical constraints are noted in the figure. Direct comparison with Fig. 2 indicates that the single scattering albedo cannot be less than ~ 0.75. Indeed, the opposition "pip" would require that it be not less than ~ 0.9. Tilt effect data for $\mu_o \lesssim 0.05$ has been ignored since our approximation that the angles of incidence and reflection are equal becomes invalid when the ring is nearly "edge-on."

For the mean optical thickness, its minimum value can be obtained by considering the case for maximum back-scattering ($x = -1$) and maximum single scattering albedo ($\varpi = 1$). Predicted photometric functions for optical thicknesses in the range $0.05 \leq \tau \leq \infty$ are shown in Fig. 4. Actual photometry of the phase effect indicates that the optical thickness cannot be less than 0.5; the opposition "pip" suggests a minimum value in the range $1 < \tau < \infty$. Tilt effect information requires the optical thickness to be greater than ~ 0.7.

The minimum back-scattering efficiency of the individual ring particles can be estimated in terms of the maximum value for the anisotropy parameter. Consider the case of maximum single scattering albedo ($\varpi = 1$) and maximum

optical thickness ($\tau = \infty$). Predicted photometric functions for anisotropy parameters in the range $-1 \leq x \leq 1$ are shown in Fig. 5. Actual photometry of the phase effect indicates $x < 1$ only; but the opposition "pip" suggests $\tilde{\omega} \lesssim 0.6$. A more stringest constraint on the back-scattering efficiency may be obtained from the tilt effect data. To satisfactorily account for the ring intensity for $\mu_0 < 0.1$, the anisotropy parameter must be negative ($x < 0$). Note that with τ set equal to infinity, the photometric function remains nearly invariant if $\tilde{\omega}$ and x are inversely coupled.

5. PRIMARY AND MULTIPLE SCATTERING: RELATIVE CONTRIBUTIONS

In order to investigate the dominance of primary scattering in determining the photometric function of the ring, its contribution to the total intensity of radiation suffering diffuse reflection has been studied for a wide range in models. Denote the intensity of reflected radiation suffering primary scattering alone, $I^{(1)}$, and the total intensity of radiation suffering both primary and multiple scattering, I. Primary scattering will be considered to dominate whenever $I^{(1)}/_I > 0.5$. The $I^{(1)}/_I$ variation with μ_0, for zero azimuth angle and equal angles of incidence and reflection, has been calculated for key combinations of single scattering albedo, anisotropy parameter, and optical thickness.

The dependence of primary scattering on single scattering albedo is illustrated in Fig. 6. To obtain a minimum estimate of the significance of primary scattering, an infinite optical thickness has been assumed. Two

scattering phase functions, corresponding to maximum back-scattering (x = -1) and isotropic scattering (x = 0), have been considered. For small μ_0 values, primary scattering always dominates, indicating that radiation cannot penetrate far into the ring before reflection. For larger μ_0 values, corresponding to the case where the ring appears wide open with respect to the Sun and Earth (ref: Fig. 2), primary scattering does not necessarily dominate unless the back-scattering efficiency is high. For x equal -1, $I^{(1)}/_I > .5$ for all $\tilde{\omega} \lesssim 1$; but for x equal zero, $I^{(1)}/_I > .5$ only for $\tilde{\omega} \lesssim .8$.

Fig. 7 illustrates the dependence of primary scattering on optical thickness. To obtain a minimum estimate of the significance of primary scattering, conservative scattering has been assumed. For μ_0 values corresponding to the case where the ring appears wide open (ref: Fig. 2), primary scattering again does not necessarily dominate unless the back-scattering efficiency is high. For x equal -1, $I^{(1)}/_I > .5$ for all $\tau \gtrsim \infty$; but for x equal zero, $I^{(1)}/_I > .5$ only for $\tau \gtrsim .8$.

Finally, the dependence of primary scattering on the anisotropy parameter is illustrated in Fig. 8. To obtain a minimum estimate of the significance of primary scattering, conservative scattering and an infinite optical thickness have been assumed. Again, primary scattering dominates for small μ_0 values. However, for μ_0 values corresponding to the case where the rings appear wide open (ref: Fig. 2), primary scattering will not dominate unless x equals -1; an even higher back-scattering efficiency would be desirable.

6. CONCLUSIONS

Permitted ranges in the single scattering albedo and the anistropy parameter are illustrated schematically in Fig. 9. Results obtained by considering the total intensity of radiation suffering diffuse reflection from the ring are shown in Fig. 9a. Fig. 9b summarizes the results obtained by imposing the condition that primary scattering must dominate in determining the photometric function of the ring. Restrictions on the optical thickness for the cases of maximum back-scattering efficiency and isotropic scattering are shown in both figures. Fig. 9c summarizes the results by imposing constraints on both primary and total intensities. Based on application of the general scattering phase functions, the single scattering albedo must lie in the range $0.75 \leq \tilde{\omega} \leq 1$, the anisotropy parameter must lie in the range $-1 \leq x \leq -.4$, and the mean perpendicular optical thickness of the ring must lie in the range $0.7 \leq \tau \leq \infty$. Least difficulty in reconciling theory with observation occurs when the selected anisotropy parameter is equal to -1. If the back-scattering efficiency of the individual particles is larger than the maximum permitted by the general phase function (Ref: Fig. 1), correspondingly smaller single scattering albedos and/or optical thicknesses would be permitted.

Our investigation of the optical scattering properties of Saturn's ring has treated the system as a whole. Our conclusions are heavily weighted towards ring B because of its photometric dominance. By way of comparison, Hameen - Anttila and Pyykko (1972) have also examined the photometric behavior of

Saturn's ring. Their study of the surface brightness of the system as a function of the Saturnocentric latitudes of the Sun and Earth treats rings A and B individually. While at low tilt angles the surface brightnesses of rings A and B appear to be essentially identical, the same does not hold true as the system opens up. Ring B steadily increases in surface brightness (cf: Fig. 2); ring A remains nearly constant, perhaps even showing a slight tendency for the surface brightness to decrease. At maximum opening, the surface brightnesses of rings A and B differ by nearly a factor 2.

Our basic ring model is entirely consistent with the Hameen-Anttila and Pyykko (1972) measurements. Consider the case of conservative scattering ($\tilde{\omega} = 1$), and maximum back-scattering efficiency ($x = -1$). Fig. 4 shows the corresponding dependence of the Tilt Effect on optical thickness (τ). Ring B measurements are consistent with $\tau \gtrsim 1$; ring A measurements with $\tau \sim 0.5$. Fig. 3 indicates that decreasing the single scattering albedo ($\tilde{\omega}$) has the effect of reducing the variation of the surface brightness with tilt angle. Photometric differences between rings A and B can be explained quite simply in terms of optical thickness alone.

In conclusion, the ring particles appear to be highly efficient back-scatters of visual radiation. Frost- or ice-covered particles can explain the large single scattering albedo (Veverka, 1973); macroscopic particles account for the overall shape of the scattering phase function; surfaces of unknown irregularity

may be necessary to explain the opposition effect. Results of the analysis are consistent with the ring particles being centimeter-size pieces of ice (Pollack, Summers, and Baldwin, 1973).

ACKNOWLEDGEMENTS

Stimulating discussions with my colleague Clark R. Chapman are acknowledged. This research was supported by the National Aeronautics and Space Administration under contract NASW-2521.

REFERENCES

Bobrov, M.S. (1970) "Surfaces and Interiors of Planets and Satellites," edited by A. Dollfus (Academic, London, 1970) p. 376.

Chandrasekhar, S. (1960) "Radiative Transfer" (Dover: New York).

Cook, A.F., Franklin, F.A., and Palluconi, F.D. (1971) "Saturn's Rings - A Survey", NASA-JPL Technical Memorandum 33-488.

Focas, J.H. and Dollfus, A. (1969) "Optical Characteristics and Thickness of Saturn's Rings Observed on the Ring Plane in 1966", Astron. and Astrophys., 2, 251.

Franklin, F.A. and Cook, A.F. (1965) "Optical Properties of Saturn's Ring. II. Two-Color Phase Curves of the Two Bright Rings". Astronomical J. 70, 704.

Goldstein, R.M. and Morris, G.A. (1973) "Radar Observations of the Rings of Saturn", Icarus, 20, 260.

Hameen-Anttila, K. A. and Pyykko, S. (1972) "Photometric Behavior of Saturn's Rings as a Function of the Saturnocentric Latitudes of the Earth and the Sun", Astronomy and Astrophysics, 19, 235, 1972.

Hapke, B. (1966) "Comments on Paper by Philip Oetking, ' Photometric Studies of Diffusely Reflecting Surfaces with Applications to the Brightness of the Moon", J. Geophysical Research, 71, 2515.

Irvine, W. M. (1966) "The Shadowing Effect in Diffuse Reflection", J. Geophysical Research, 71, 2931.

Jeffreys, H. (1947) "The Effects of Collisions on Saturn's Rings", Monthly Notices Roy. Ast. Soc., 107, 263.

Lebofsky, L. A., Johnson, T.V. and McCord, T.B. (1970) "Saturn's Rings: Spectral Reflectivity and Compositional Implications" Icarus, 13, 226.

Oetking, P. (1966) "Photometric Studies of Diffusely Reflecting Surfaces with Applications to the Brightness of the Moon", J. Geophysical Research, 71, 2505.

Pollack, J.B., Summers, A. and Baldwin, B. (1973) "Estimates of the Size of the Particles in the Rings of Saturn and their Cosmogonic Implications", Icarus, 20, 263.

Price, M.J. (1973) "Optical Scattering Properties of Saturn's Ring", Astronomical J., 78, 113.

Veverka, J. (1973) "The Photometric Properties of Natural Snow and of Snow-covered Planets", Icarus, 20, 304.

FIGURE CAPTIONS

Fig. 1. Polar diagrams of specimen scattering phase functions for individual ring particles. Single scattering albedos are equal, and the far-field approximation is adopted. Two cases based on the general phase function discussed in the text (Eq. (2)), maximum back-scattering ($x = -1$) and isotropic scattering ($x = 0$), are illustrated. The case of a macroscopic sphere having a Lambert scattering surface is shown for comparison.

Fig. 2. Photometric function data for Saturn's ring at visual (V) wavelengths. Information concerning the phase effect is taken from Franklin and Cook (1965), with corrections from Cook, Franklin and Palluconi (1971). I is the mean specific intensity of the ring surface (rings A and B together); πF is the solar flux at Saturn. Azimuth angle is measured in the ring plane; zero azimuth corresponds to the projected line joining the center of Saturn with the center of the Sun. During the course of the observations, the planetocentric declinations of the Sun and Earth remained nearly constant near -26 (± 0.5) degrees. Tilt effect data are taken from Price (1973). Data refer to phase angles greater than 1.5 degrees. No attempt has been made to correct the measurements to a constant phase angle. The parameter μ_0 is the cosine of the angle of incidence with respect to the outward normal. Except when the rings are viewed essentially "edge-on", the angles of incidence and reflection are nearly equal. No attempt has been made to correct either set of data to equal angles of incidence and reflection.

Fig. 3. Theoretical Prediction of the Photometric Function for Saturn's Ring: Variation with single scattering albedo ($\tilde{\omega}$) for maximum back-scattering efficiency (x = -1) and infinite optical thickness ($\tau = \infty$). Ordinates and abscissae are defined in the caption to Fig. 2. Equal angles of incidence and reflection are assumed. For the phase effect, the planetocentric solar declination angle has been taken as constant at the 1959 opposition value, $-26^{\circ}.230$ (Ref: Fig. 2). For the tilt effect, zero azimuth angle has been adopted.

Fig. 4. Theoretical Prediction of the Photometric Function for Saturn's Ring: Variation with optical thickness (τ) for maximum back-scattering efficiency (x = -1) and conservative scattering ($\tilde{\omega} = 1$). Ordinates, abscissae and geometrical constraints remain the same as in Fig. 3.

Fig. 5. Theoretical Prediction of the Photometric Function for Saturn's Ring: Variation with anisotropy parameter (x) for infinite optical thickness ($\tau = \infty$) and conservative scattering ($\tilde{\omega} = 1$). Ordinates, abscissae and geometrical constraints remain the same as in Fig. 3.

Fig. 6. Theoretical Investigation of Primary and Multiple Scattering in Saturn's Ring: Relative contributions as a function of single scattering albedo ($\tilde{\omega}$). Two scattering phase functions are considered, corresponding to maximum back-scattering ($x = -1$) and to isotropic scattering ($x = 0$). In both cases, infinite optical thickness ($\tau = \infty$), zero azimuth angle, and equal angles of incidence and reflection are assumed. The ordinates are defined in terms of $I^{(1)}$ and I. The quantity $I^{(1)}$ is the specific intensity of radiation suffering only single scattering before reflection; I is the specific intensity of radiation suffering one or more scatterings before escape from the ring as diffusely reflected light. The abscissae are the cosines of the angles of incidence with respect to the outward normal.

Fig. 7. Theoretical Investigation of Primary and Multiple Scattering in Saturn's Ring: Relative contributions as a function of optical thickness (τ). Two scattering phase functions are considered, corresponding to maximum back-scattering ($x = -1$) and to isotropic scattering ($x = 0$). In both cases, conservative scattering ($\tilde{\omega} = 1$), zero azimuth angle, and equal angles of incidence and reflection are assumed. The ordinates and abscissae are defined in the caption to Fig. 6.

Fig. 8. Theoretical Investigation of Primary and Multiple Scattering in Saturn's Ring; Relative contributions as a function of anisotropy parameter (x). Conservative scattering ($\tilde{\omega} = 1$), infinite optical thickness ($\tau = \infty$), zero azimuth angle, and equal angles of incidence and relfection are assumed. The ordinates and abscissae are defined in the caption to Fig. 6.

Fig. 9. Summary of the basic radiative transfer parameters for Saturn's Ring. Single scattering albedo ($\tilde{\omega}$) is plotted against anisotropy parameter (x). Shaded areas indicate regions excluded by the analysis. Fig. 9a indicates permitted ranges in the parameters on the basis of the total intensity of radiation suffering diffuse reflection from the ring. Extreme ranges in optical thickness (τ) are also indicated. Fig. 9b indicates permitted ranges in the parameters on the basis of the photometric function being determined predominantly by primary scattering alone. Fig. 9c indicates permitted ranges in the parameters on the basis of both types of constraint.

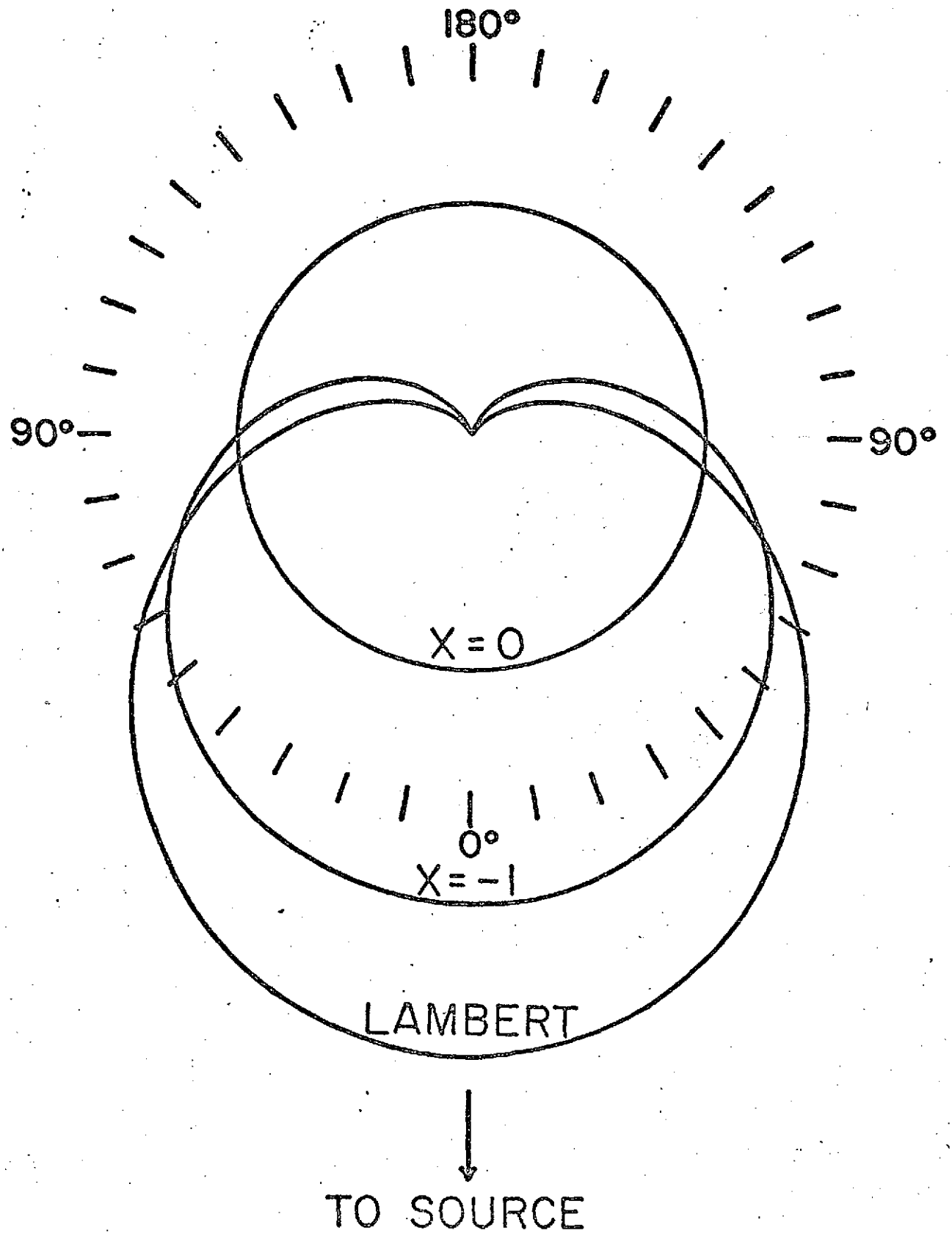

Fig. 1

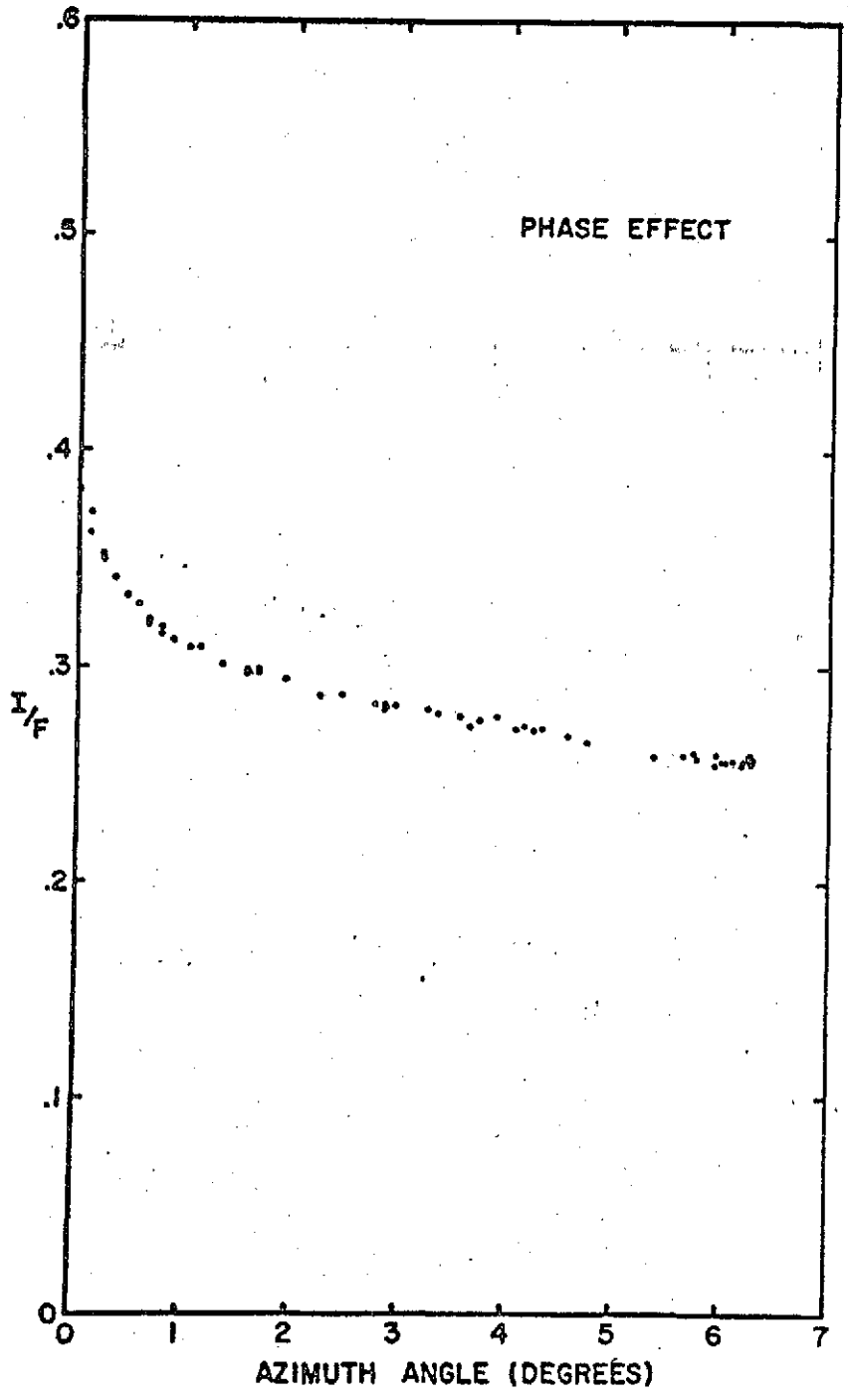
PHASE EFFECT
I/F
.6
.5
.4
.3
.2
.1
0
0
1
2
3
4
5
6
7
AZIMUTH ANGLE (DEGREES)

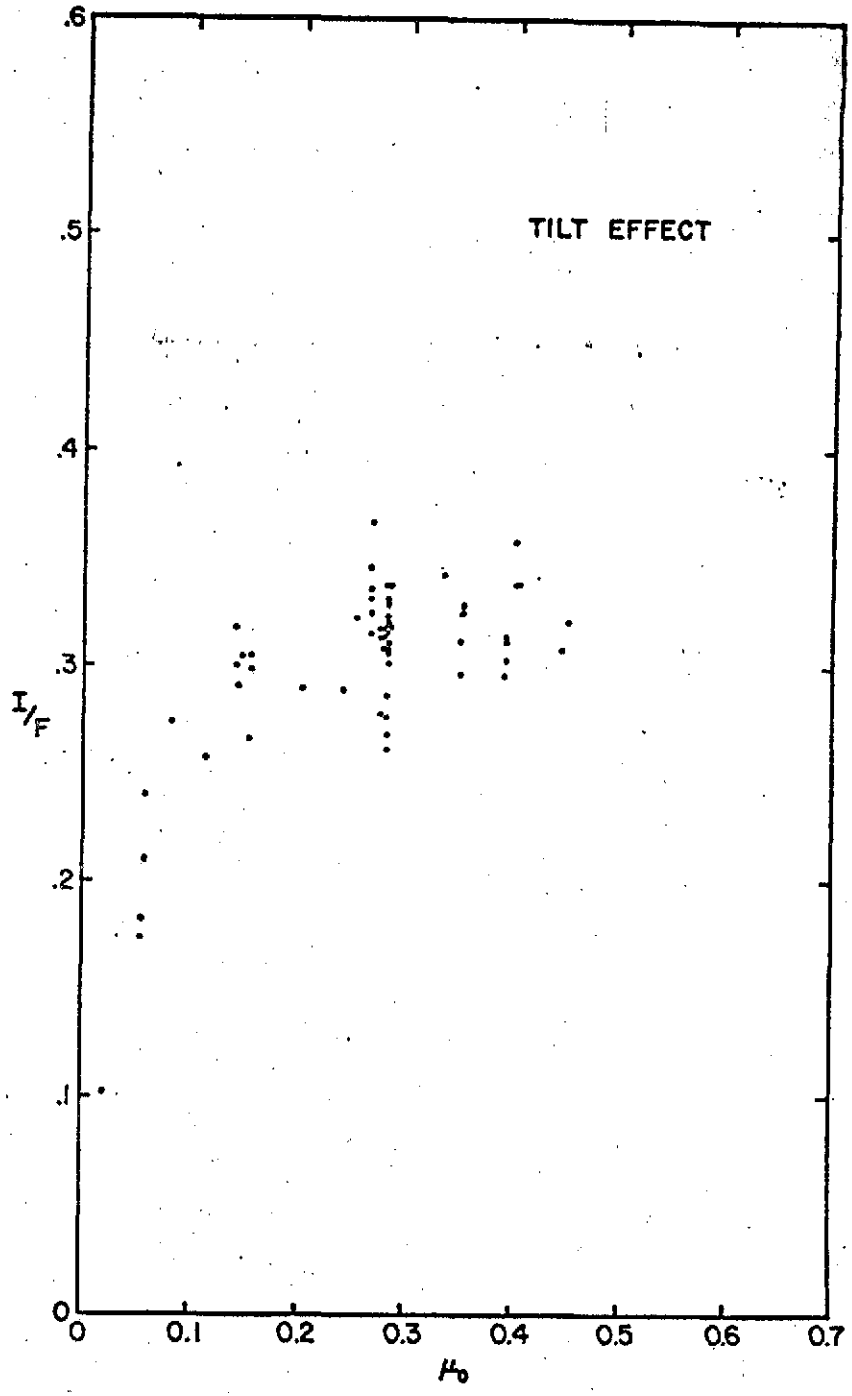
TILT EFFECT
I/F
.6
.5
.4
.3
.2
.1
0
0
0.1
0.2
0.3
0.4
0.5
0.6
0.7
μ0

Fig. 2

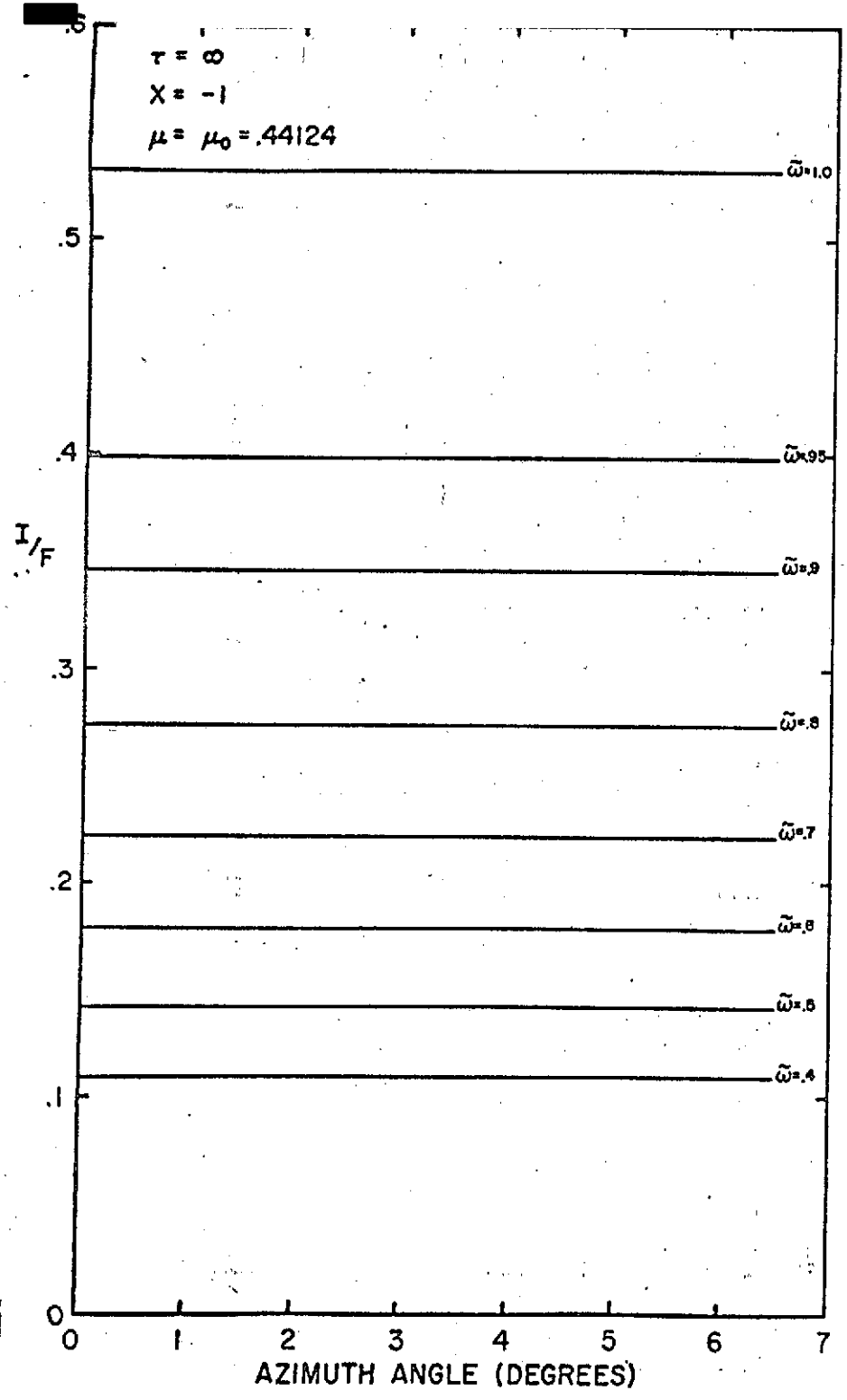
τ = ∞
X = -1
μ = μ₀ = .44124
ω̃=1.0
ω̃=.95
ω̃=.9
ω̃=.8
ω̃=.7
ω̃=.6
ω̃=.5
ω̃=.4
I/F
AZIMUTH ANGLE (DEGREES)

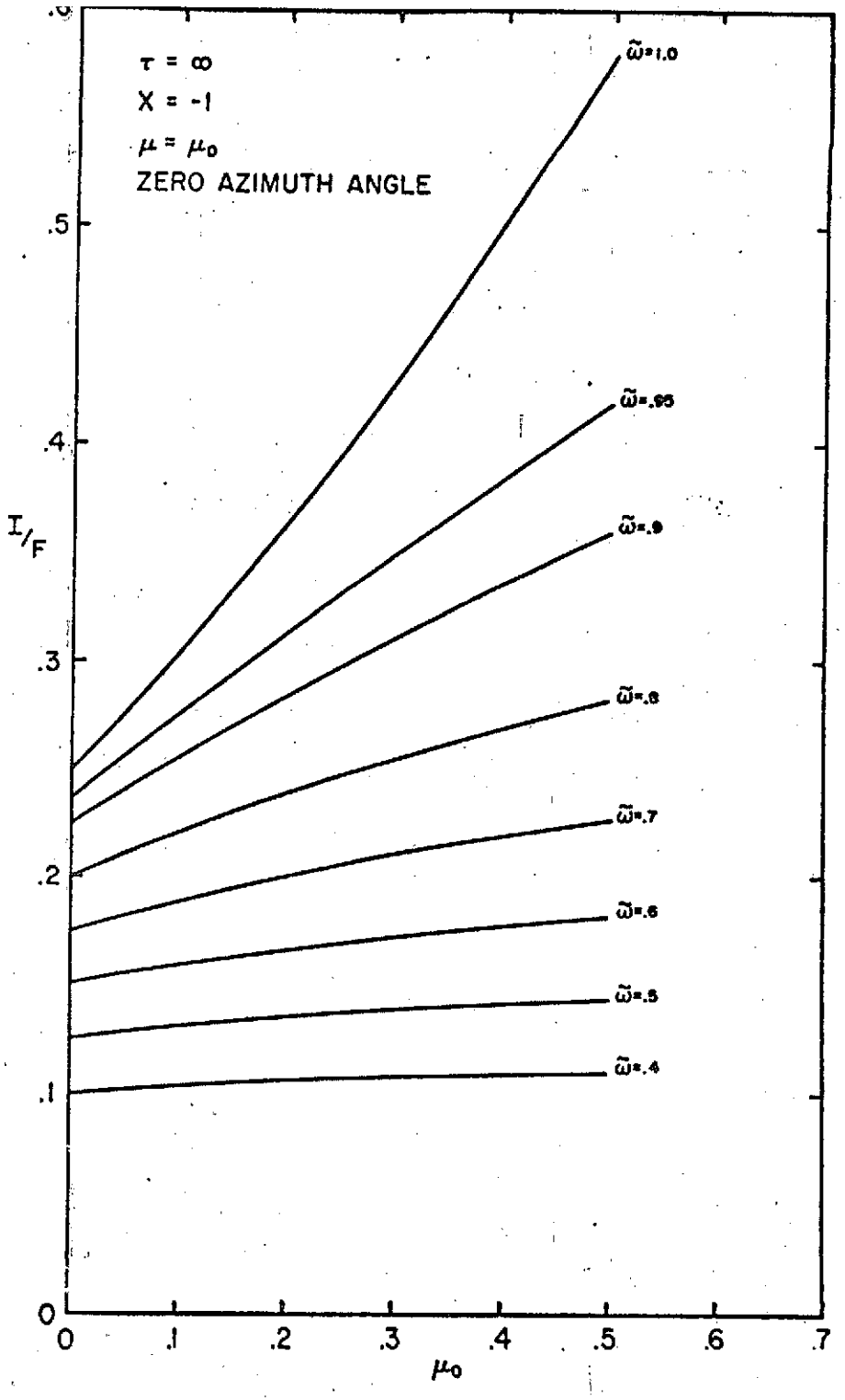
τ = ∞
X = -1
μ = μ₀
ZERO AZIMUTH ANGLE
ω̃=1.0
ω̃=.95
ω̃=.9
ω̃=.8
ω̃=.7
ω̃=.6
ω̃=.5
ω̃=.4
I/F
μ₀

Fig. 3

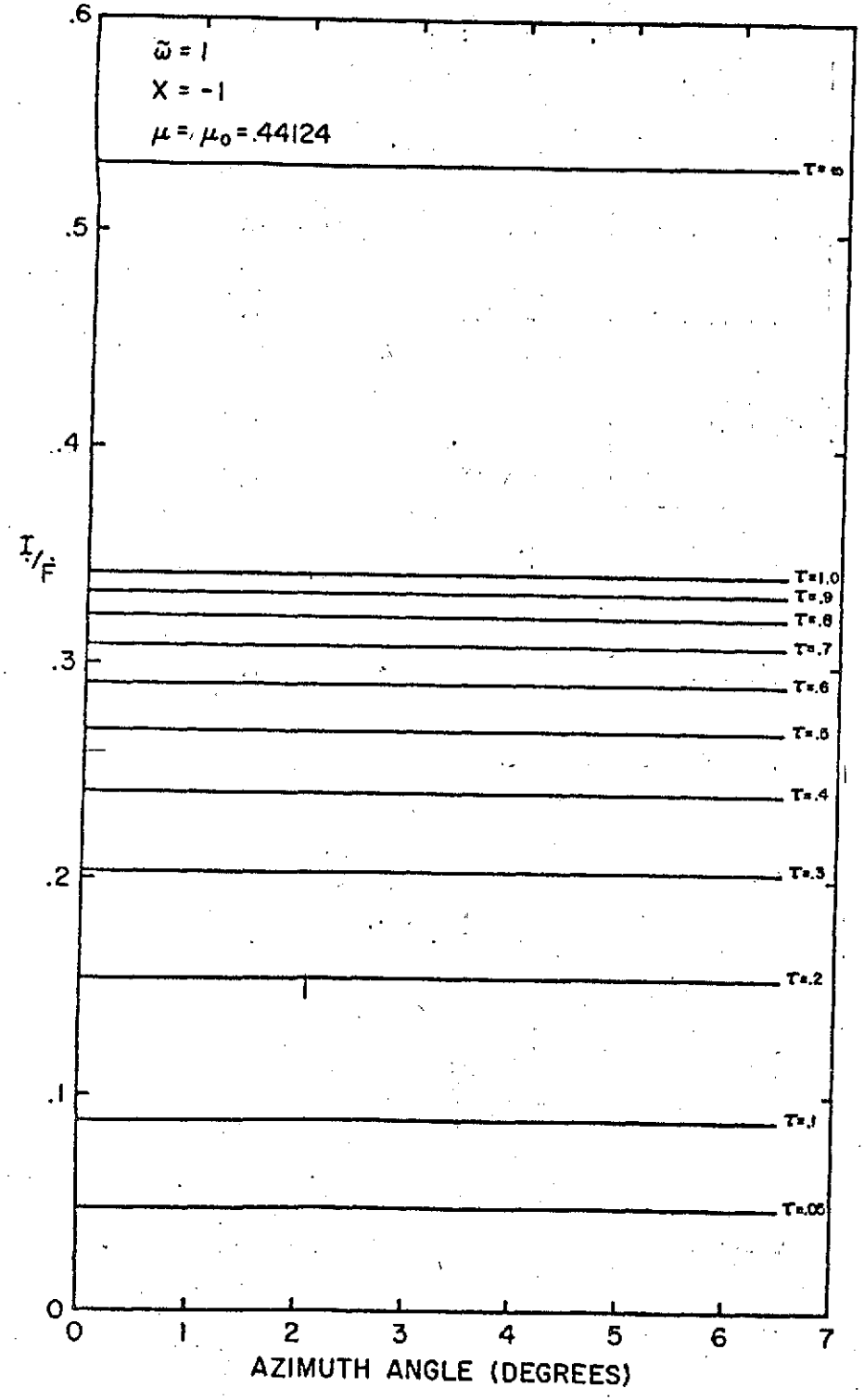
$\tilde{\omega} = 1$
X = -1
$\mu = \mu_0 = .44124$
I/F
τ=∞
τ=1.0
τ=.9
τ=.8
τ=.7
τ=.6
τ=.5
τ=.4
τ=.3
τ=.2
τ=.1
τ=.05
0
.1
.2
.3
.4
.5
.6
0
1
2
3
4
5
6
7
AZIMUTH ANGLE (DEGREES)

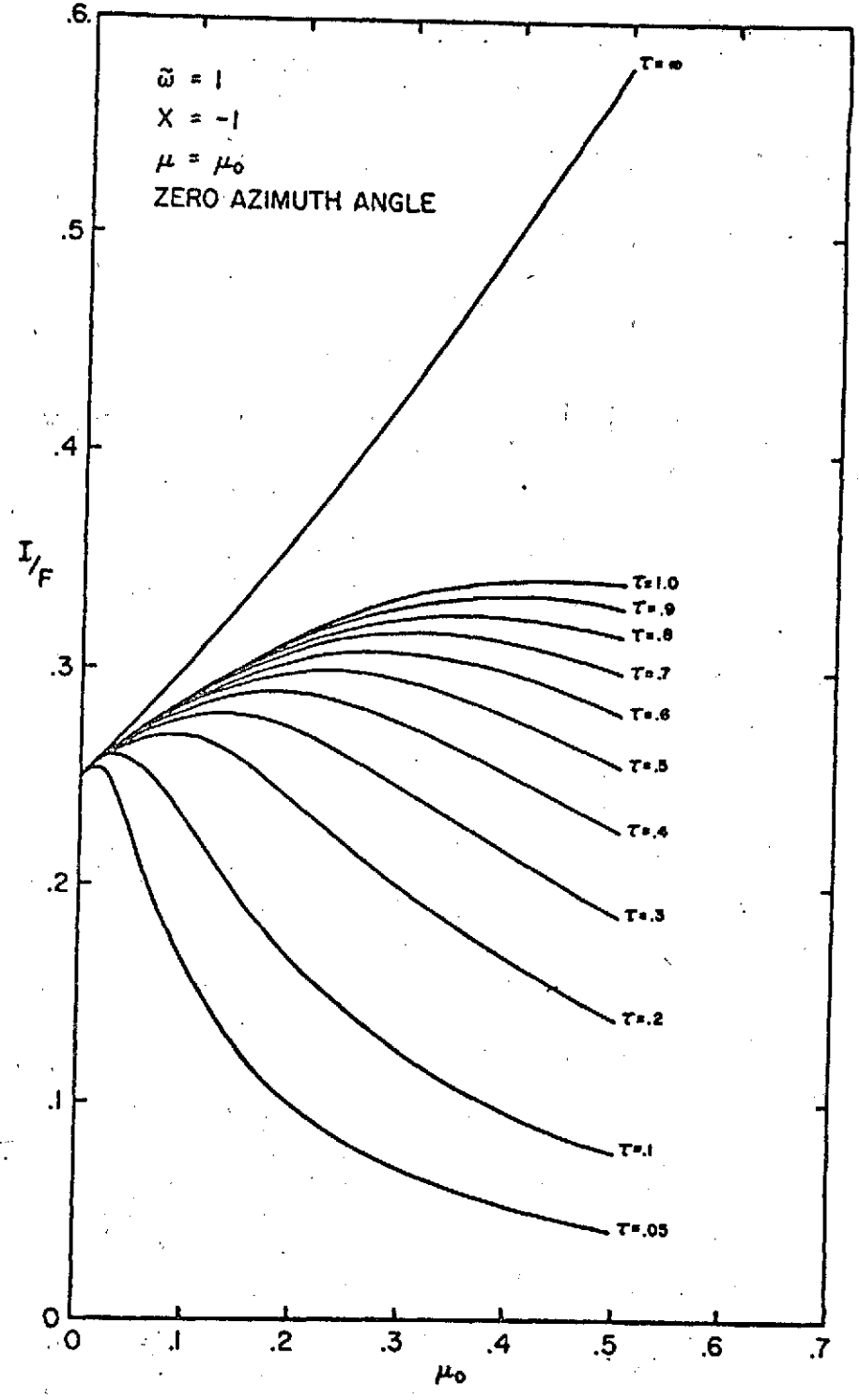
$\tilde{\omega} = 1$
X = -1
$\mu = \mu_0$
ZERO AZIMUTH ANGLE
I/F
τ=∞
τ=1.0
τ=.9
τ=.8
τ=.7
τ=.6
τ=.5
τ=.4
τ=.3
τ=.2
τ=.1
τ=.05
0
.1
.2
.3
.4
.5
.6
.7
μ_0

F. 9.4

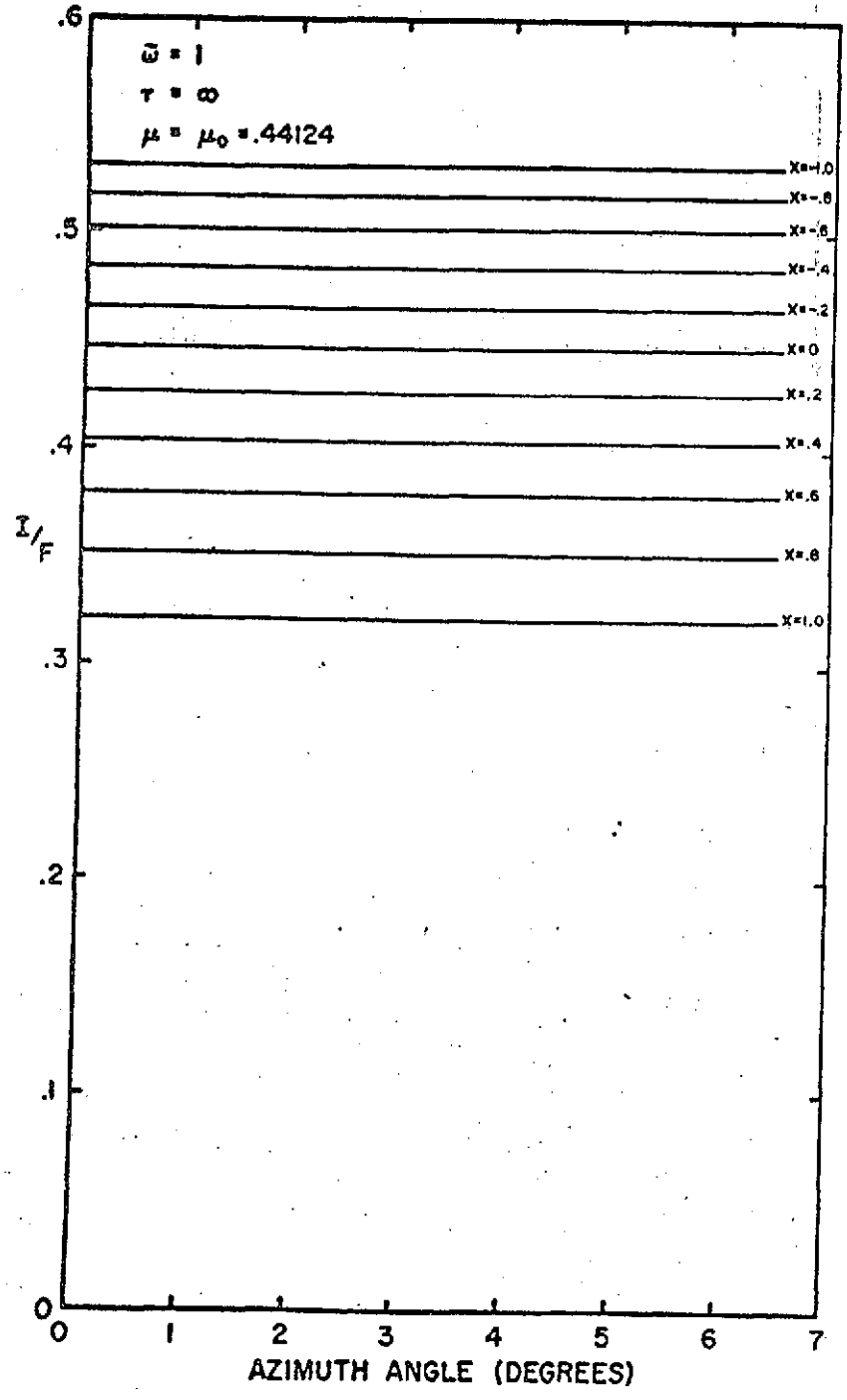
ω̃ = 1
τ = ∞
μ = μ₀ = .44124
X=-1.0
X=-.8
X=-.6
X=-.4
X=-.2
X=0
X=.2
X=.4
X=.6
X=.8
X=1.0
I/F
AZIMUTH ANGLE (DEGREES)

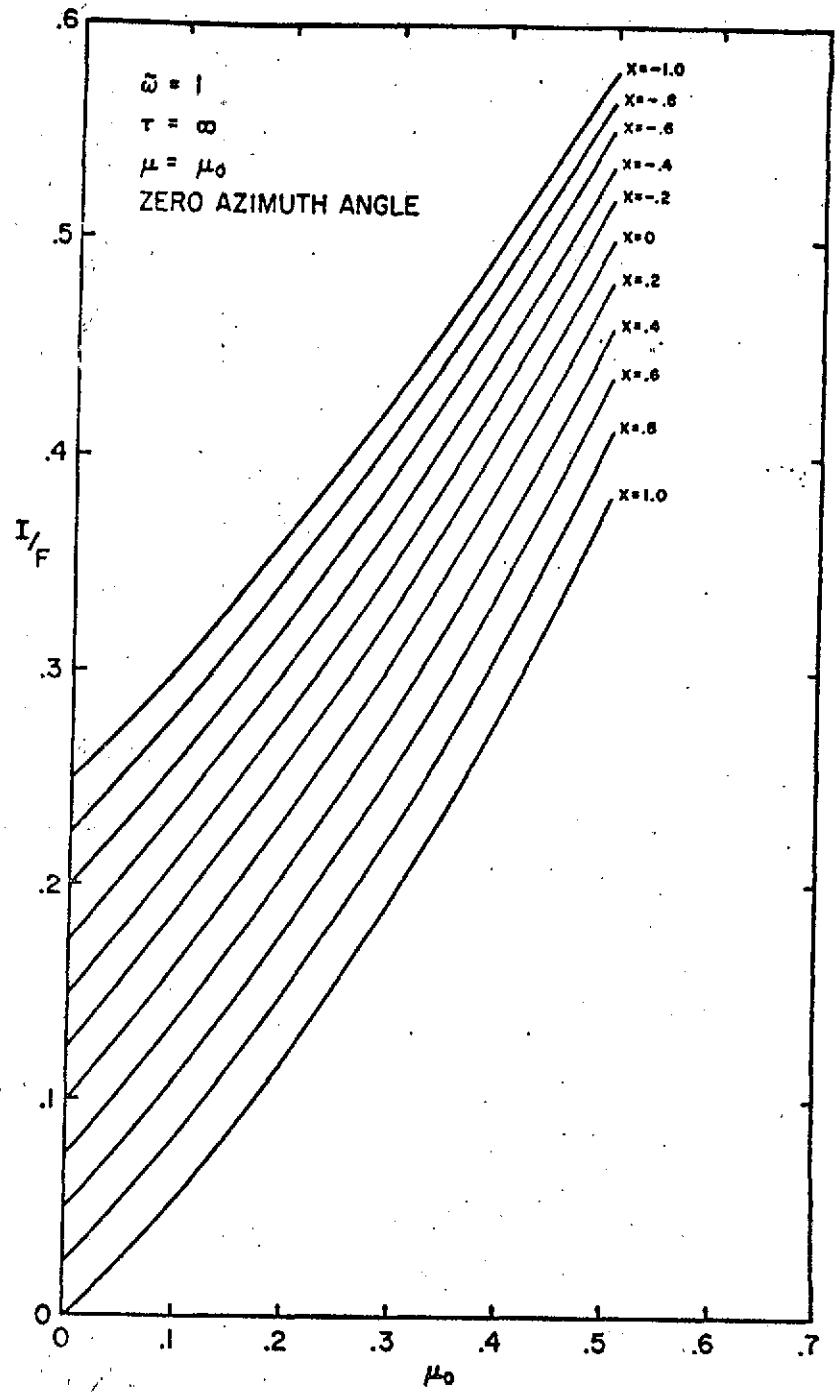
ω̃ = 1
τ = ∞
μ = μ₀
ZERO AZIMUTH ANGLE
X=-1.0
X=-.8
X=-.6
X=-.4
X=-.2
X=0
X=.2
X=.4
X=.6
X=.8
X=1.0
I/F
μ₀

Fig. 5

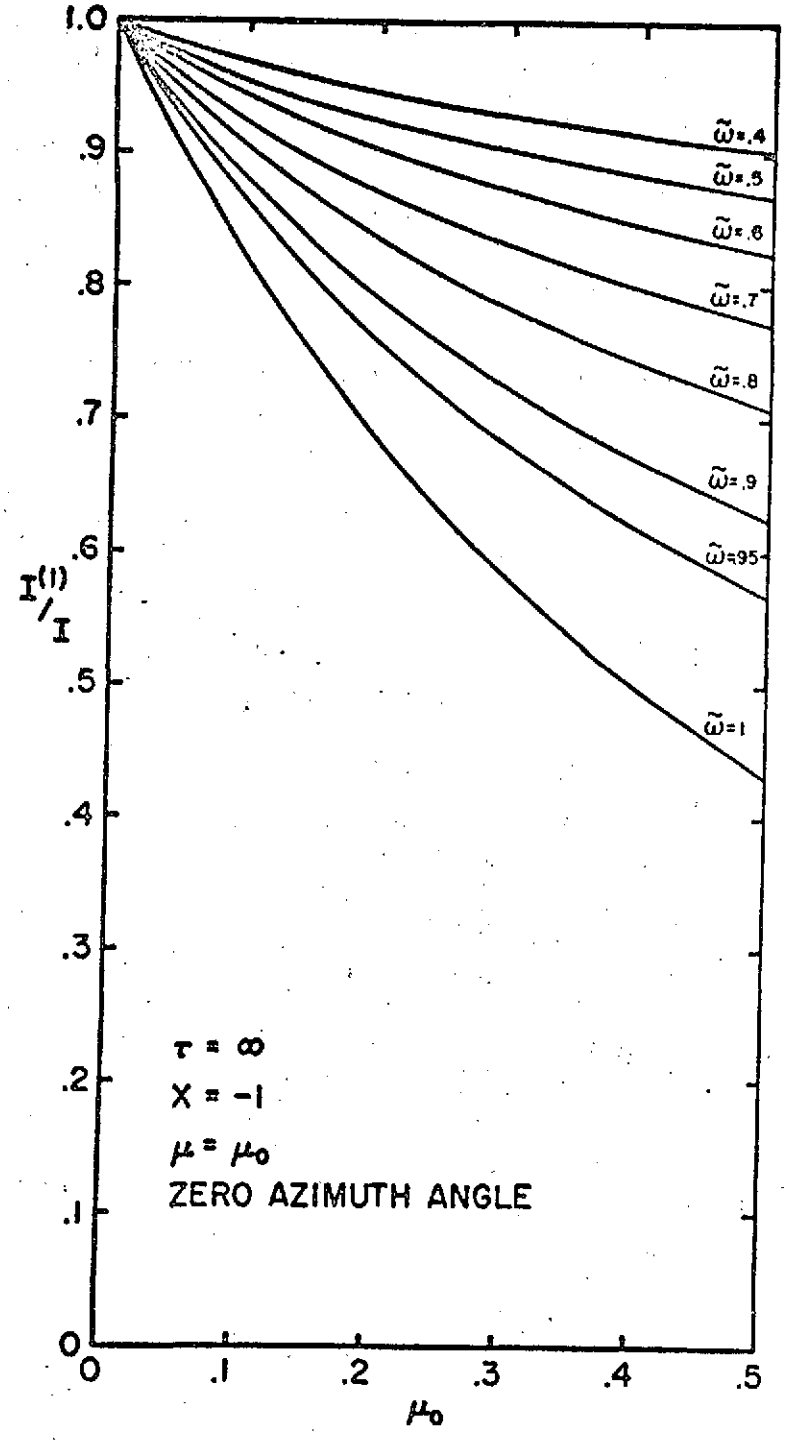
1.0
.9
.8
.7
.6
.5
.4
.3
.2
.1
0
$I^{(1)}/I$
$\tilde{\omega}$=.4
$\tilde{\omega}$=.5
$\tilde{\omega}$=.6
$\tilde{\omega}$=.7
$\tilde{\omega}$=.8
$\tilde{\omega}$=.9
$\tilde{\omega}$=.95
$\tilde{\omega}$=1
$\tau = \infty$
X = -1
$\mu = \mu_0$
ZERO AZIMUTH ANGLE
0
.1
.2
.3
.4
.5
μ_0

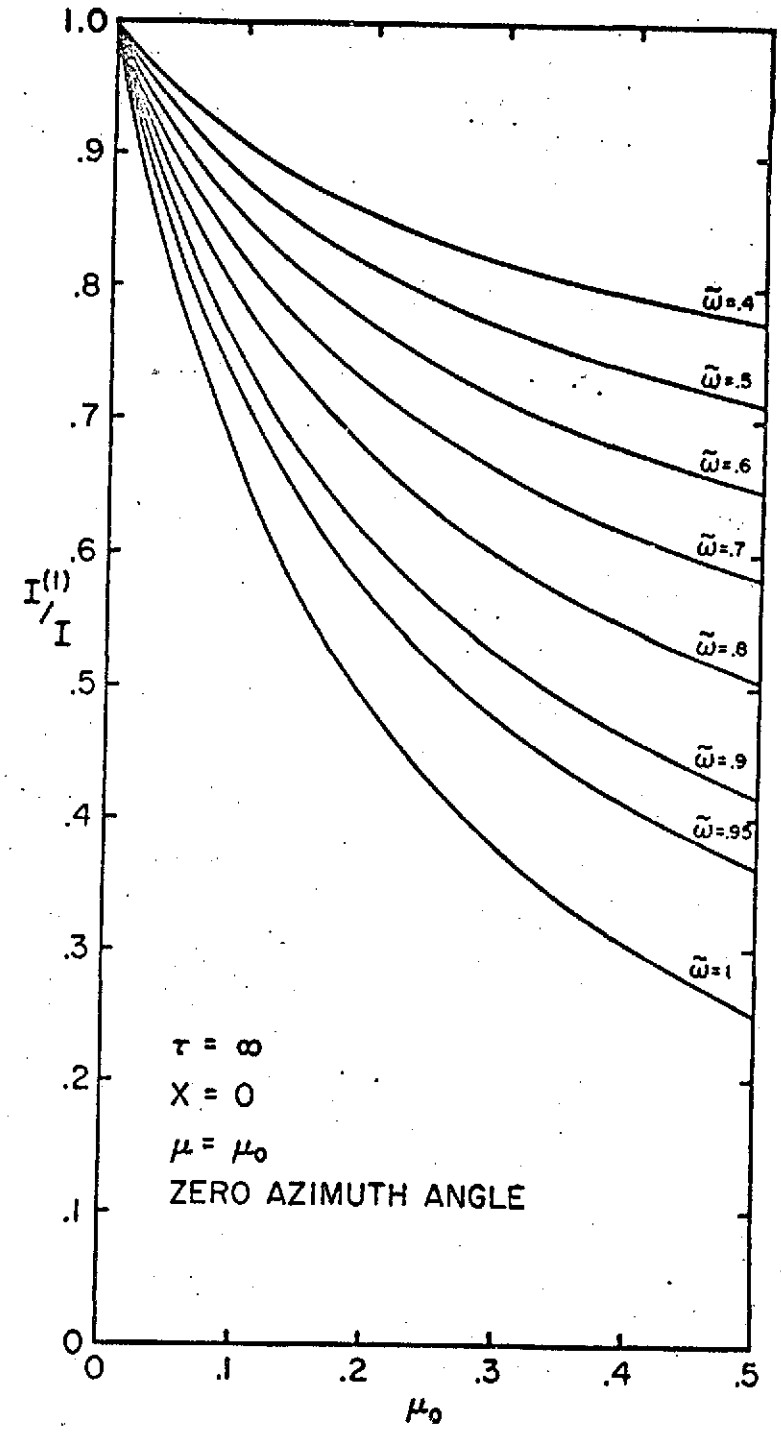
1.0
.9
.8
.7
.6
.5
.4
.3
.2
.1
0
$I^{(1)}/I$
$\tilde{\omega}$=.4
$\tilde{\omega}$=.5
$\tilde{\omega}$=.6
$\tilde{\omega}$=.7
$\tilde{\omega}$=.8
$\tilde{\omega}$=.9
$\tilde{\omega}$=.95
$\tilde{\omega}$=1
$\tau = \infty$
X = 0
$\mu = \mu_0$
ZERO AZIMUTH ANGLE
0
.1
.2
.3
.4
.5
μ_0

Fig 6

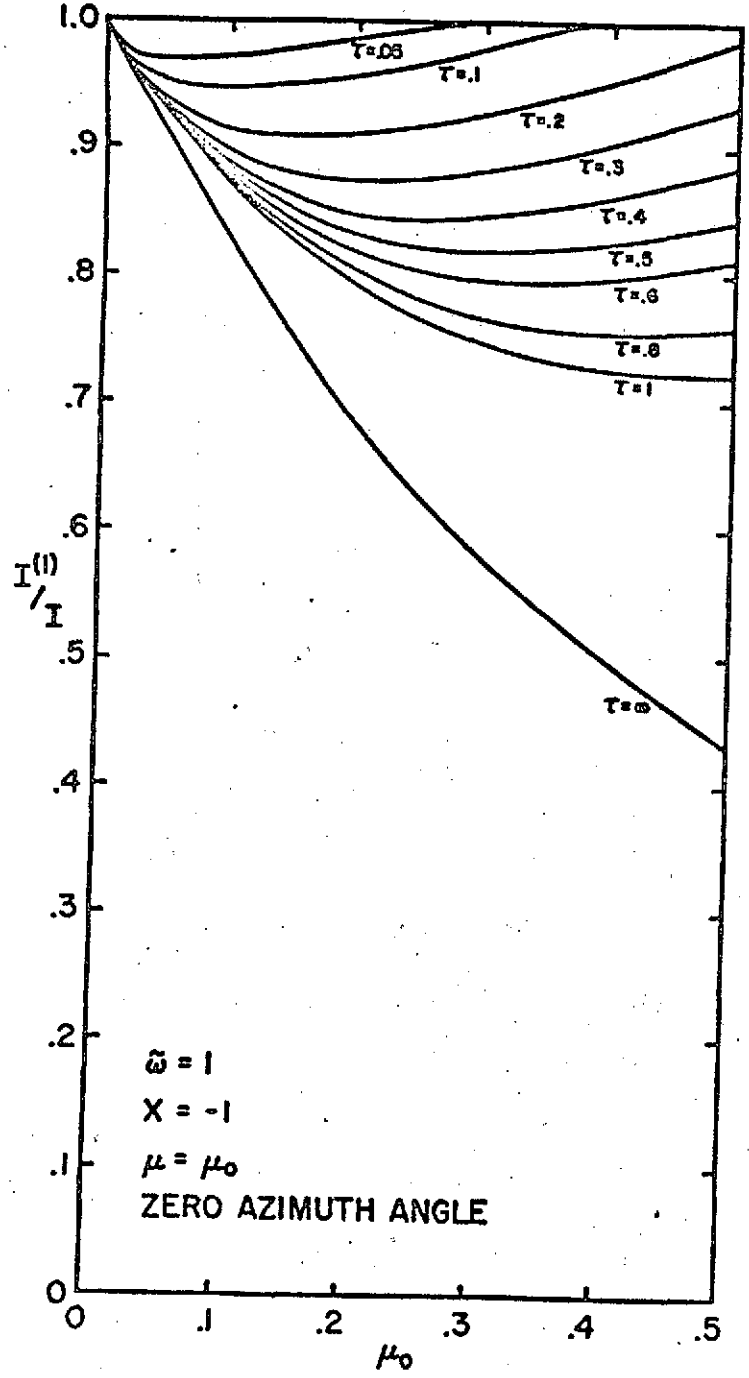
1.0
.9
.8
.7
.6
.5
.4
.3
.2
.1
0
$I^{(1)}/I$
τ=.05
τ=.1
τ=.2
τ=.3
τ=.4
τ=.5
τ=.6
τ=.8
τ=1
τ=∞
$\tilde{\omega} = 1$
X = -1
$\mu = \mu_0$
ZERO AZIMUTH ANGLE
0
.1
.2
.3
.4
.5
μ_0

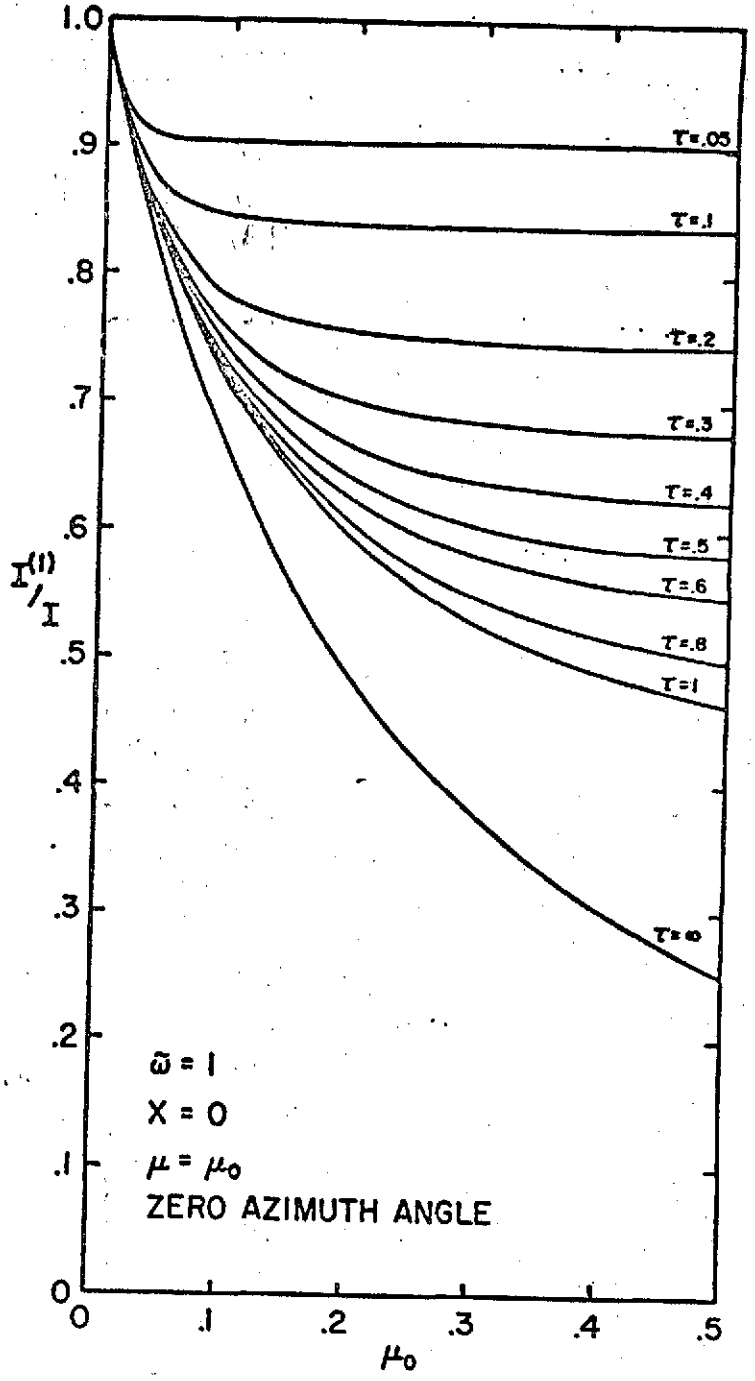
1.0
.9
.8
.7
.6
.5
.4
.3
.2
.1
0
$I^{(1)}/I$
τ=.05
τ=.1
τ=.2
τ=.3
τ=.4
τ=.5
τ=.6
τ=.8
τ=1
τ=∞
$\tilde{\omega} = 1$
X = 0
$\mu = \mu_0$
ZERO AZIMUTH ANGLE
0
.1
.2
.3
.4
.5
μ_0

Fig 7

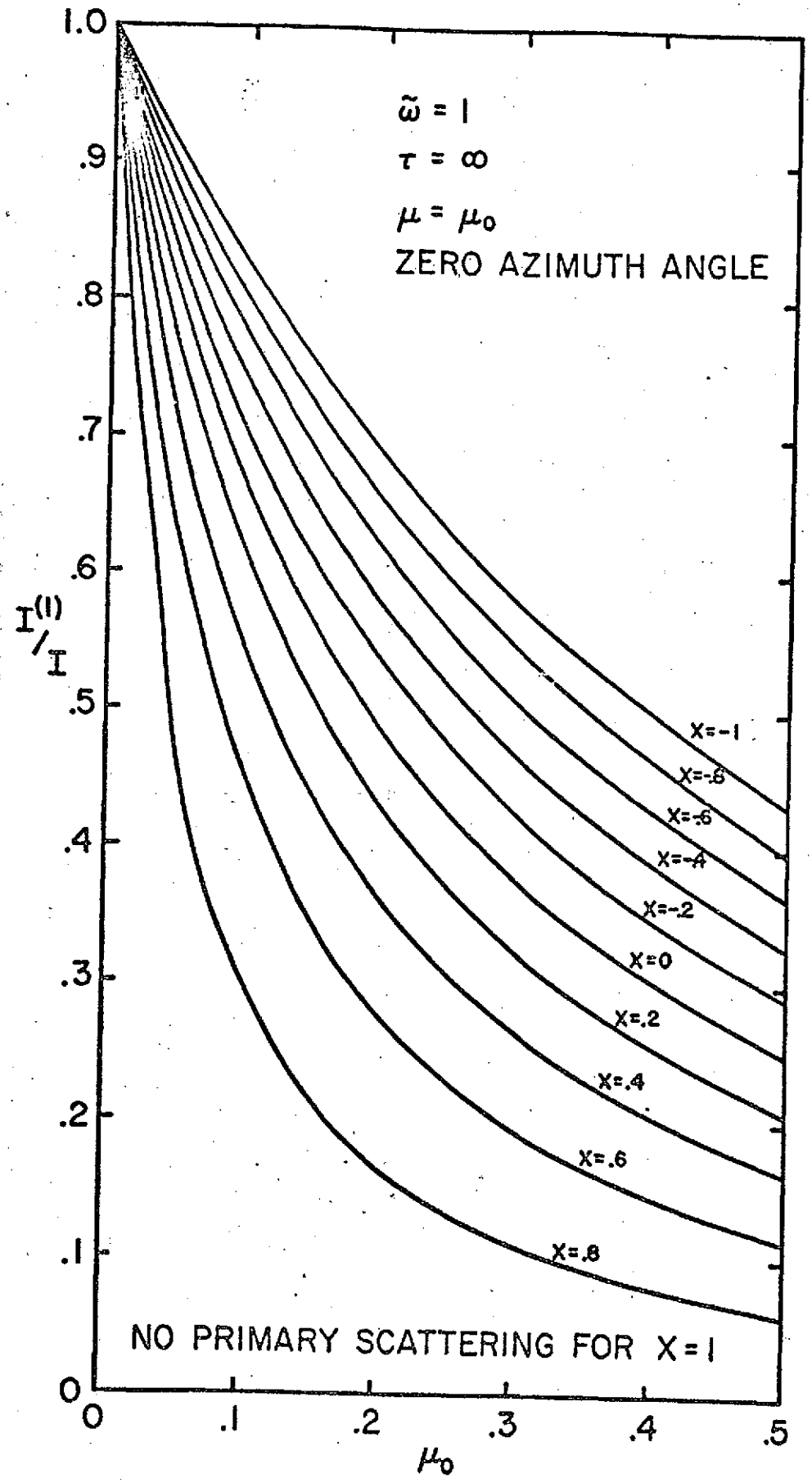
$\tilde{\omega} = 1$
$\tau = \infty$
$\mu = \mu_0$
ZERO AZIMUTH ANGLE
$I^{(1)}/I$
μ_0
X=-1
X=-.8
X=-.6
X=-.4
X=-.2
X=0
X=.2
X=.4
X=.6
X=.8
NO PRIMARY SCATTERING FOR X=1
0
.1
.2
.3
.4
.5
.6
.7
.8
.9
1.0

Fig. 8

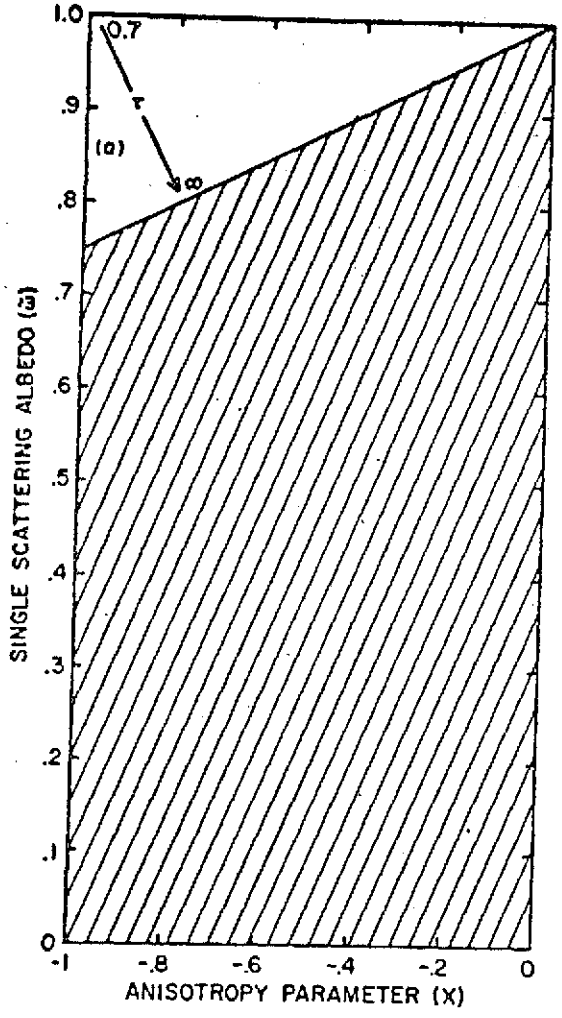
1.0
.9
.8
.7
.6
.5
.4
.3
.2
.1
0
0.7
τ
(a)
∞
SINGLE SCATTERING ALBEDO (ω̃)
-1
-.8
-.6
-.4
-.2
0
ANISOTROPY PARAMETER (X)

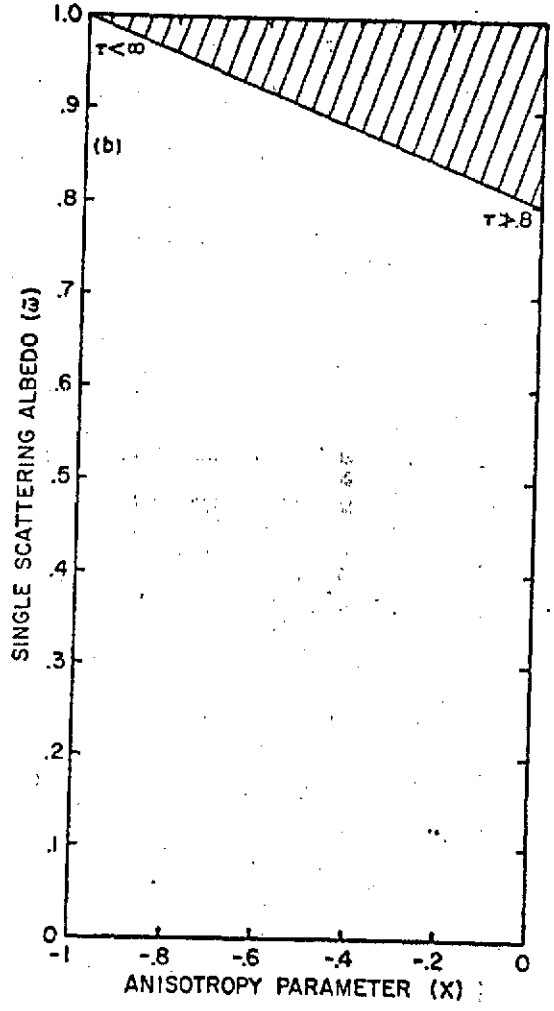
1.0
.9
.8
.7
.6
.5
.4
.3
.2
.1
0
τ<∞
(b)
τ→∞
SINGLE SCATTERING ALBEDO (ω̃)
-1
-.8
-.6
-.4
-.2
0
ANISOTROPY PARAMETER (X)

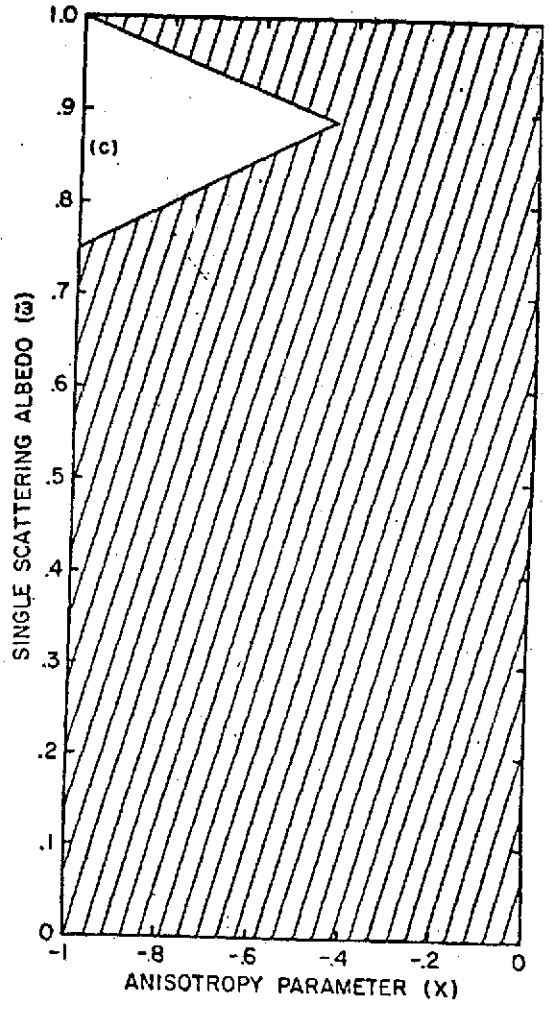
1.0
.9
.8
.7
.6
.5
.4
.3
.2
.1
0
(c)
SINGLE SCATTERING ALBEDO (ω̃)
-1
-.8
-.6
-.4
-.2
0
ANISOTROPY PARAMETER (X)

Fig. 9

SATURN'S RING
AND
PIONEER 11

Michael J. Price
Planetary Science Institute
Tucson, Arizona 85704

Received_____

No. of Copies: 4

No. of MS Pages: 13

No. of Figures: 5

No. of Tables: 0

ABSTRACT

Quantitative predictions of the diffuse reflection and transmission properties of Saturn's ring, relevant to the September 1979 Pioneer 11 flyby are presented. Predictions are based on an elementary anisotropic scattering model; interparticle separations are sufficiently large that mutual shadowing is negligible, the far field approximation being valid. Wide ranges in the fundamental radiative transfer parameters are considered. Cases of pronounced back-scattering and of isotropic scattering are treated individually. Measurement of the radiation suffering diffuse scattering by the ring should provide useful information concerning the single scattering albedo, the general shape of the scattering phase function, and optical thickness.

1. INTRODUCTION

Recently, Price (1973, 1974) rediscussed the optical scattering properties of Saturn's ring using Earth-based photometric function data at visual wavelengths. Evidence indicating both that primary scattering dominates and that mutual shadowing is an irrelevant concept, was reviewed. Simple anisotropic scattering radiative transfer models were used to define the probable ranges both in the single scattering albedo, and in the general shape of the scattering phase function. Limitations on the mean perpendicular optical thickness of the ring were also obtained. Results indicated that the ring particles are highly efficient back-scatterers of visual radiation. Macroscopic particles account for the basic shape of the scattering phase function. Based on an infinite optical thickness for the ring, a minimum single scattering albedo ~ 0.75 was found. Use of conservative scattering lead to a minimum optical thickness ~ 0.7. The analysis was consistent with the ring particles being centimeter-size pieces of ice.

Currently, the NASA Pioneer 11 spacecraft is enroute to Saturn via Jupiter. On board the spacecraft is an Imaging Photopolarimeter Experiment (Gehrels, 1974), providing a unique opportunity for investigating the validity of optical scattering models for the ring. Whatever the actual spacecraft fly-by trajectory at Saturn, the observed diffuse reflection and transmission properties of the ring are predicted in this paper on the basis of the optimum models derived by Price (1973, 1974). Emphasis is placed on predicting the visual appearance of the ring system as a function of viewpoint.

2. DIFFUSE SCATTERING BY THE RING

Our basic ring model (Price, 1974) is a homogeneous, plane-parallel, layer of anisotropically scattering particles illuminated by a parallel beam of solar radiation. Interparticle distances are sufficiently large that each particle may be considered to be in the far field of its neighbors. The optical scattering properties of the ring are completely described by three basic radiative transfer parameters: single scattering albedo ($\tilde{\omega}$), anisotropy parameter (x), and optical thickness (τ). The general shape of the scattering phase function is described by the elementary form

$$p(\Theta) = \tilde{\omega}(1 + x \cos \Theta) \qquad (1)$$

where Θ is the scattering angle. The classical theory for multiple scattering may therefore be applied. Analytical solutions and approximate computational techniques developed by Chandrasekhar (1960) have been used c.f. Price (1974).

Our optimum ring model (Price, 1974) requires the maximum back-scattering efficiency (x = -1). The scattering phase function is then equivalent to the far field of a macroscopic sphere for which the intensity of radiation scattered in a given direction is proportional to the apparent area illuminated. The single scattering albedo was found to lie in the range $0.75 \leq \tilde{\omega} \leq 1$; the corresponding mean perpendicular optical thickness, in the range $\infty \geq \tau \geq 0.7$.

Our predictions of the diffuse reflection and transmission properties of the ring should span the probable ranges in the single scattering albedo, in the optical thickness, and in the anisotropy parameter. Specifically, two extreme values for the single scattering albedo have been selected, i.e. $\tilde{\omega} = 0.5$ and $\tilde{\omega} = 1.0$. In order to examine the relative photometric properties of the major ring components, two distinct values for the optical thickness are adopted. For investigations of rings A and C, $\tau = 0.1$ is used; for ring B, $\tau = 1$. Dependence of the predictions on choice of the anisotropy parameter may be illustrated by considering the two cases of maximum back-scattering efficiency ($x = -1$) and of isotropic scattering ($x = 0$).

Since Pioneer 11 will encounter Saturn only one year before the ring system presents an "edge-on" aspect to the sun (in late 1980), the chosen solar illumination angle must necessarily be low. In the usual notation, the cosine of the angle of incidence (or reflection) with respect to the outward normal is labelled μ_0 (or μ). All predictions correspond to $\mu_0 = 0.05$. Because our radiative transfer theory tacitly assumes the ring to be laterally both homogeneous and infinite in extent, it can be expected to breakdown for small μ, μ_0 values. All predictions therefore correspond to $\mu \geq 0.05$ only.

Results of the computations are contained in Figs. 1 through 5. Fig. 1 treats the case of isotropic scattering ($x = 0$); Figs. 2 through 5, the case of maximum back-scattering efficiency ($x = -1$). The specific intensity, I,

measured in units of F (where πF is the solar flux at Saturn) is plotted against μ. For isotropic scattering, the $I/_F$ v μ curves depend only on ϖ and τ; they are identical for all azimuth angles. In the case of maximum back-scattering efficiency, the $I/_F$ v μ curves depend also on the azimuth angle. Note that azimuth angle is measured in the ring plane between the projected lines which individually join the point on the ring surface under consideration to the Sun and to the spacecraft; zero azimuth corresponds to the projected solar direction.

3. THE VIEW FROM THE SPACECRAFT

Bearing in mind that the flight time of Pioneer 11 from the Earth to Saturn (6 1/2 years) greatly exceeds the design lifetime of the spacecraft (900 days), our predictions must consider the possibility of partial or even complete failure of the imaging photometric experiment. Should calibration difficulties prohibit absolute photometry, relative photometry between the individual ring components may still be possible. Both absolute and relative photometric predictions of the appearance of Saturn's ring have therefore been made. Should the spacecraft be no longer functioning at Saturn encounter, the predictions will yet be relevant to the imaging experiment on board the pair of 1977 Mariner Jupiter-Saturn missions. Both Mariner spacecraft are expected to encounter Saturn during the first half of 1981. By then, the ring will have passed through its "edge-on" aspect, presenting its other face to the Sun. Even so, the geometry of solar illumination will be very similar to the situation when Pioneer 11 flew by.

Dependence of the diffuse reflection and transmission properties of the ring on both the single scattering albedo and optical thickness can be most easily examined by considering the simple case of isotropic scattering ($x = 0$). Complications introduced by anisotropic scattering will be considered later. Our quantitative predictions are contained in Fig. 1.

In the case of diffuse reflection, the specific intensity is low because of the shallow solar illumination angle. Specific intensity decreases rapidly and monotonically as the angle of reflection becomes more nearly normal to the ring plane; the rate of decrease slows very significantly for $\mu \geq 0.5$. From all viewpoints, the absolute specific intensity appears to be very sensitive to ϖ for constant τ. Increasing ϖ from 0.5 to unity changes the specific intensity by a factor 2-3. The absolute specific intensity is not particularly sensitive to τ for constant ϖ. Increasing τ from 0.1 to unity results in changing the specific intensity by never more than at most a factor 2, frequently by very much less. Diffuse reflection measurements can therefore provide information concerning the single scattering albedo. Not, so, however, concerning the optical thickness.

For the case of diffuse transmission, the specific intensity is again very low because of the shallow solar illumination angle. Dependence of the specific intensity on the angle of transmission is determined by optical thickness. For small optical thicknesses ($\tau = 0.1$), the specific intensity decreases rapidly and monotonically as the angle of transmission becomes more nearly normal to the ring plane; the rate of decrease slows very

significantly for $\mu \geq 0.5$. For large optical thicknesses ($\tau = 1$), the specific intensity remains nearly constant. From all viewpoints, the absolute specific intensity appears to be very sensitive to the single scattering albedo for constant τ. Increasing $\tilde{\omega}$ from 0.5 to unity changes the specific intensity by a factor 2-3. From all viewpoints, the specific intensity decreases with increasing optical thickness for constant single scattering albedo. For small μ, the absolute specific intensity is very sensitive to τ for constant $\tilde{\omega}$. For μ equal 0.1, increasing τ from 0.1 to unity results in changing the specific intensity by a factor 5 - 15, depending on the $\tilde{\omega}$ value. For μ near unity, the absolute specific intensity is not sensitive to τ. Diffuse transmission measurements can therefore provide information on optical thickness if the single scattering albedo is known, and the spacecraft elevation angle small.

Expected dependences of the diffuse reflection and transmission properties of the ring on azimuth angle are illustrated in Figs. 2, 3, 4 and 5. Each figure corresponds to our preferred radiative transfer model in which the anisotropy parameter, x, is set equal to -1. Two individual single scattering albedos are again used, $\tilde{\omega} = 0.5$ and 1. For $\tilde{\omega} = 0.5$, Figs. 2 and 3 illustrate the diffuse reflection and transmission characteristics, respectively. For $\tilde{\omega} = 1$, Figs. 4 and 5 illustrate the diffuse reflection and transmission characteristics, respectively. Each diagram considers four azimuth angles $\psi = 0^{\circ}$, 45°, 90°, and 180°. For $\psi \leq 90^{\circ}$, the diffuse reflection and transmission properties of the ring remain

qualitatively very similar to the isotropic scattering case. Not surprisingly, highest values for the specific intensity occur for $\psi = 0^{o}$ (i.e. the back-scattering direction). In the forward-scattering direction ($\psi = 180^{o}$), the reflection and transmission characteristics are very alike; the specific intensity is insensitive to μ and τ. Evidently, discrimination between scattering phase functions will likely require observations with $\psi > 90^{o}$.

Several major qualitative predictions may also be made. When the ring is viewed from the spacecraft by reflected sunlight, its visual appearance will be similar to that observed from the Earth. In surface brightness, ring A will always be fainter than ring B. Contrast between rings A and B will gradually increase with the spacecraft elevation angle. By comparison, when the ring is viewed from the spacecraft in transmitted sunlight, its visual appearance will differ widely from that observed from the Earth. For small spacecraft elevation angles, ring A will exhibit a surface brightness much greater than that of ring B. However, as the spacecraft elevation angle increases, contrast between the major ring components will entirely disappear. When viewed from a direction perpendicular to the ring plane, the system should appear uniformly bright.

ACKNOWLEDGEMENTS

This research was supported by the National Aeronautics and Space Administration under contract NASW-2521.

REFERENCES

Price, M. J. (1973) " Optical Scattering Properties of Saturn's Ring". Astronomical J. 78, 113.

Price, M. J. (1974) "Optical Scattering Properties of Saturn's Ring. II." Icarus (in press).

Gehrels, T. et al (1974) "The Imaging Photopolarimeter Experiment on Pioneer 10". Science 183, 318.

Chandrasekhar, S. (1960) "Radiative Transfer" (Dover: New York).

FIGURE CAPTIONS

Fig. 1: Theoretical Predictions of the Diffuse Reflection and Transmission Properties of Saturn's Ring. Isotropic scattering ($x = 0$) is assumed. Two values of the single scattering albedo ($\tilde{\omega}$) are considered, 0.5 and unity. Calculations are presented for two values of the optical thickness (τ), 0.1 and unity. The cosine of the angle of incidence of solar radiation with respect to the outward normal to the ring plane (μ_0) is taken as 0.05. Each diagram refers to all azimuth angles. Azimuth angle is measured in the ring plane, the zero point corresponding to the projected Saturn-Sun line. Ordinates are the specific intensity, I, measured in units F, where πF is the solar flux at Saturn. Abscissae are the cosines of the angles of emergence with respect to the outward normal to the ring plane, μ.

Fig. 2: Theoretical Predictions of the Diffuse Reflection Properties of Saturn's Ring. Maximum back-scattering ($x = -1$) is assumed. The single scattering albedo ($\tilde{\omega}$) is taken as 0.5. Calculations are presented for two values of the optical thickness (τ), 0.1 and unity. The cosine of the angle of incidence of solar radiation with respect to the outward normal to the ring plane (μ_0) is taken as 0.05. Four values for the azimuth angle (ψ) are considered: 0°, 45°, 90°, and 180°. Azimuth angle is measured in the ring

plane, the zero point corresponding to the projected Saturn-Sun line. Ordinates are the specific intensity, I, measured in units F, where πF is the solar flux at Saturn. Abscissae are the cosines of the angles of emergence with respect to the outward normal to the ring plane, μ.

Fig. 3: Theoretical Predictions of the Diffuse Transmission Properties of Saturn's Ring. Maximum back-scattering ($x = -1$) is assumed. The single scattering albedo ($\tilde{\omega}$) is taken as 0.5. Calculations are presented for two values of the optical thickness (τ), 0.1 and unity. The cosine of the angle of incidence of solar radiation with respect to the outward normal to the ring plane (μ_0) is taken as 0.05. Four values for the azimuth angle (ψ) are considered: 0^o, 45^o, 90^o, and 180^o. Azimuth angle is measured in the ring plane, the zero point corresponding to the projected Saturn-Sun line. Ordinates are the specific intensity, I, measured in units F, where πF is the solar flux at Saturn. Abscissae are the cosines of the angles of emergence with respect to the outward normal to the ring plane, μ.

Fig. 4: Theoretical Predictions of the Diffuse Reflection Properties of Saturn's Ring. Maximum conservative ($\tilde{\omega} = 1$) back-scattering ($x = -1$) is assumed. Calculations are presented for two values of

the optical thickness (τ), 0.1 and unity. The cosine of the angle of incidence of solar radiation with respect to the outward normal to the ring plane (μ_0) is taken as 0.05. Four values for the azimuth angle (ψ) are considered: 0^o, 45^o, 90^o, and 180^o. Azimuth angle is measured in the ring plane, the zero point corresponding to the projected Saturn-Sun line. Ordinates are the specific intensity, I, measured in units F, where πF is the solar flux at Saturn. Abscissae are the cosines of the angles of emergence with respect to the outward normal to the ring plane, μ.

Fig. 5: Theoretical Predictions of the Diffuse Transmission Properties of Saturn's Ring. Maximum conservative ($\tilde{\omega} = 1$) back-scattering ($x = -1$) is assumed. Calculations are presented for two values of the optical thickness (τ), 0.1 and unity. The cosine of the angle of incidence of solar radiation with respect to the outward normal to the ring plane (μ_0) is taken as 0.05. Four values for the azimuth angle (ψ) are considered: 0^o, 45^o, $90^o$and 180^o. Azimuth angle is measured in the ring plane, the zero point corresponding to the projected Saturn-Sun line. Ordinates are the specific intensity, I, measured in units F, where πF is the solar flux at Saturn. Abscissae are the cosines of the angles of emergence with respect to the outward normal to the ring plane, μ.

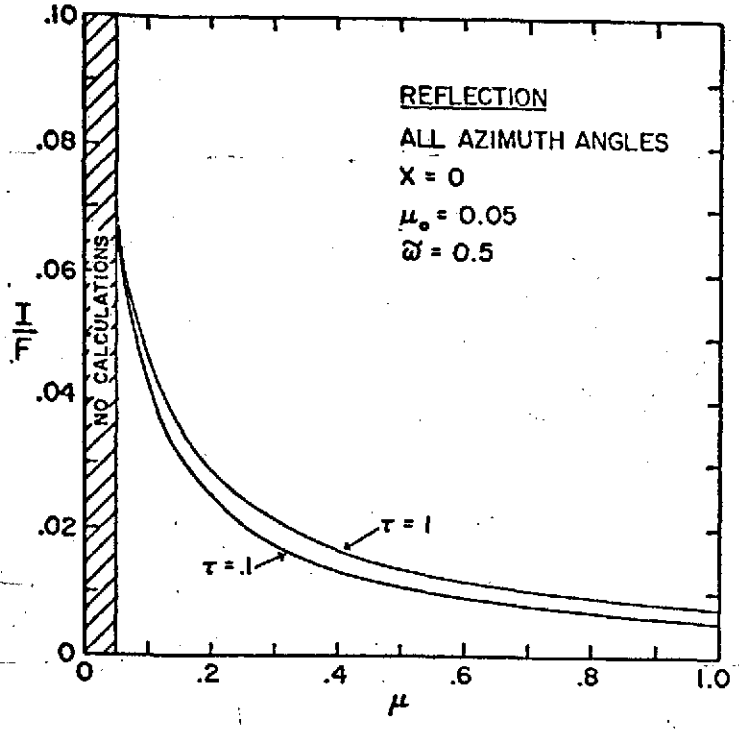
REFLECTION
ALL AZIMUTH ANGLES
X = 0
μ_o = 0.05
ϖ = 0.5
NO CALCULATIONS
τ = 1
τ = .1
$\frac{I}{F}$
μ

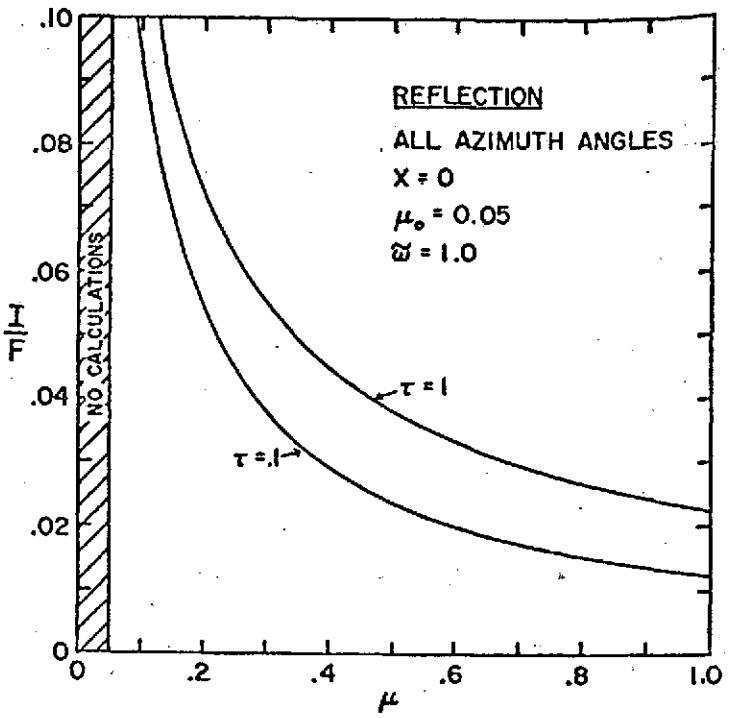
REFLECTION
ALL AZIMUTH ANGLES
X = 0
μ_o = 0.05
ϖ = 1.0
NO CALCULATIONS
τ = 1
τ = .1
$\frac{I}{F}$
μ

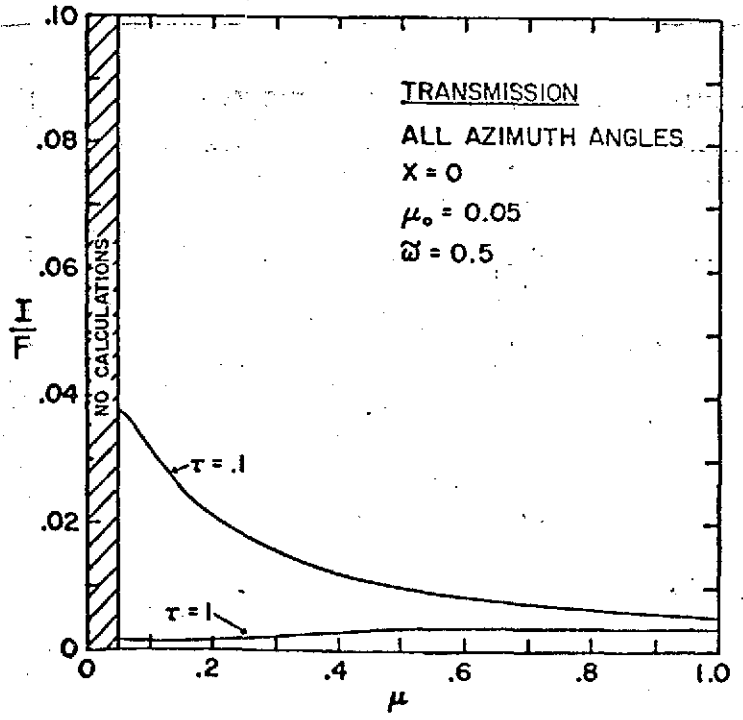
TRANSMISSION
ALL AZIMUTH ANGLES
X = 0
μ_o = 0.05
ϖ = 0.5
NO CALCULATIONS
τ = .1
τ = 1
$\frac{I}{F}$
μ

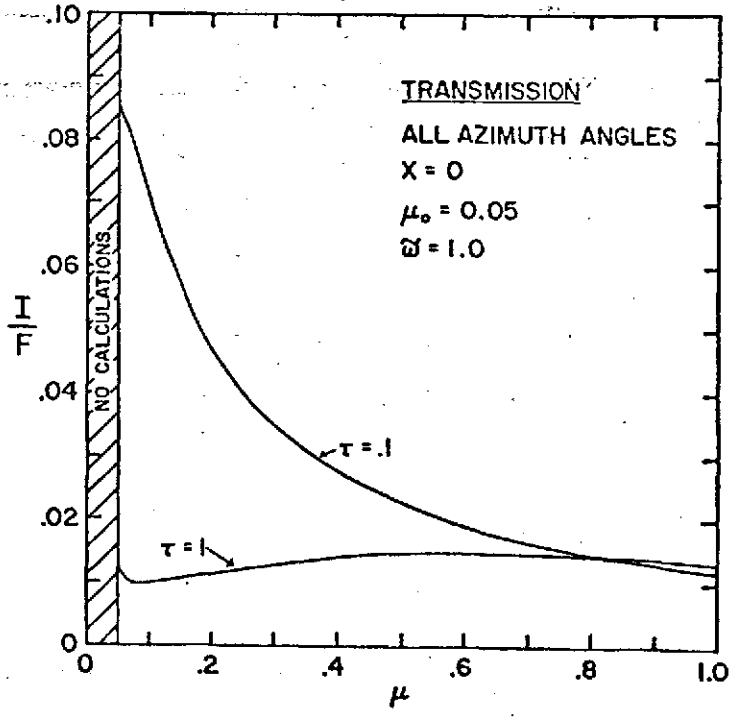
TRANSMISSION
ALL AZIMUTH ANGLES
X = 0
μ_o = 0.05
ϖ = 1.0
NO CALCULATIONS
τ = .1
τ = 1
$\frac{I}{F}$
μ

Fig. 1

REFLECTION: $X = -1$, $\mu_o = 0.05$, $\tilde{\omega} = 0.5$

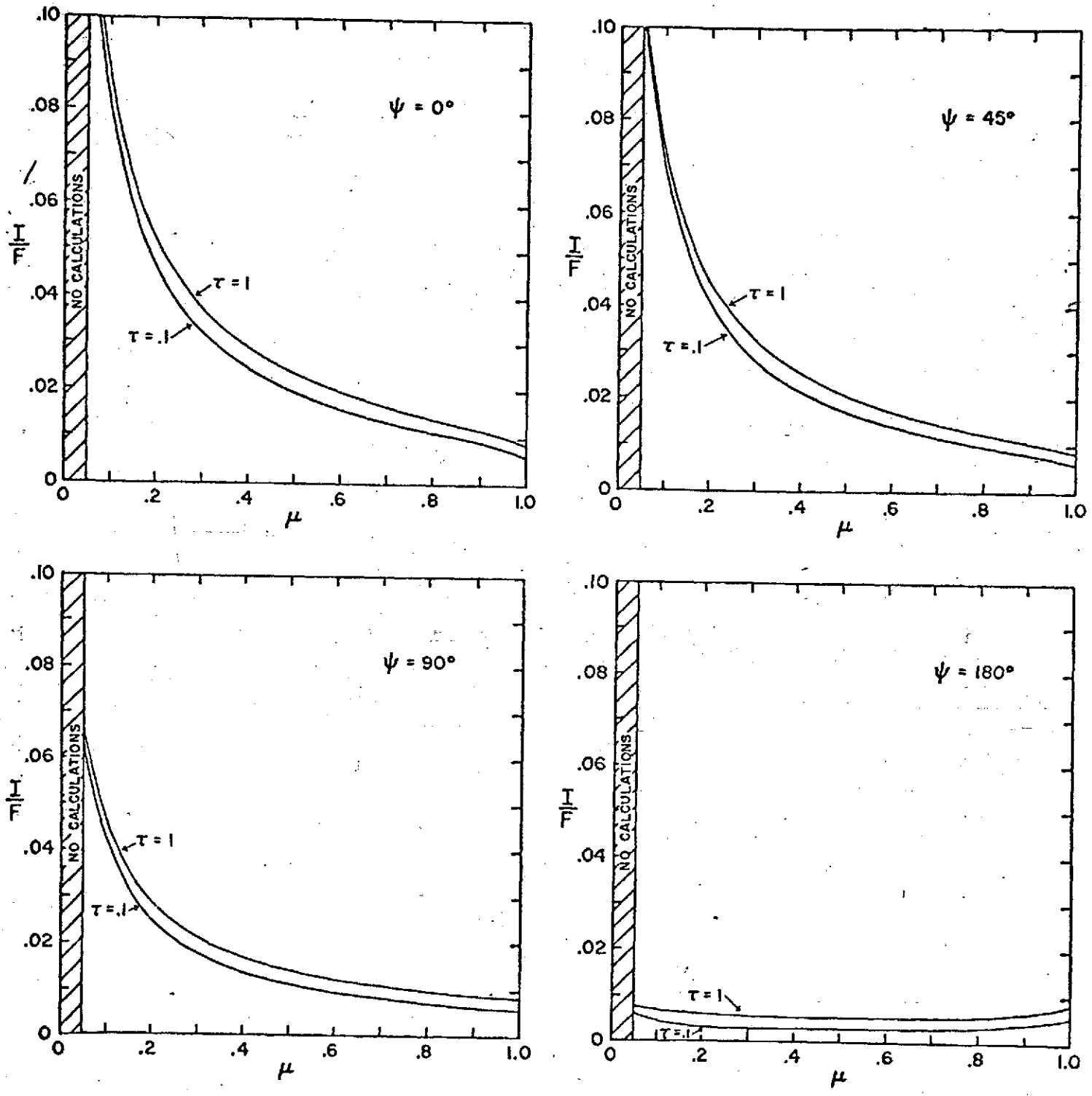

Fig. 2

TRANSMISSION: $X = -1$, $\mu_o = 0.05$, $\tilde{\omega} = 0.5$

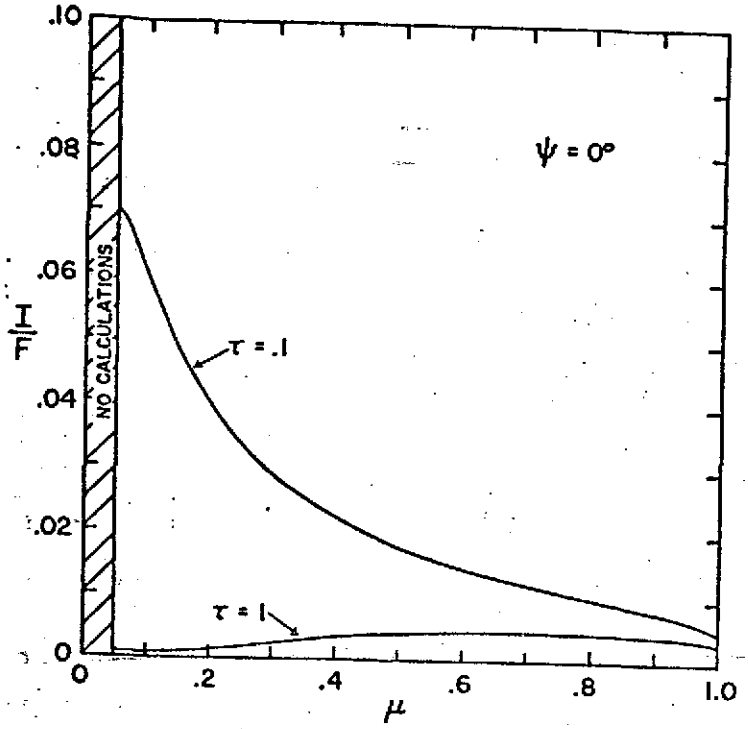

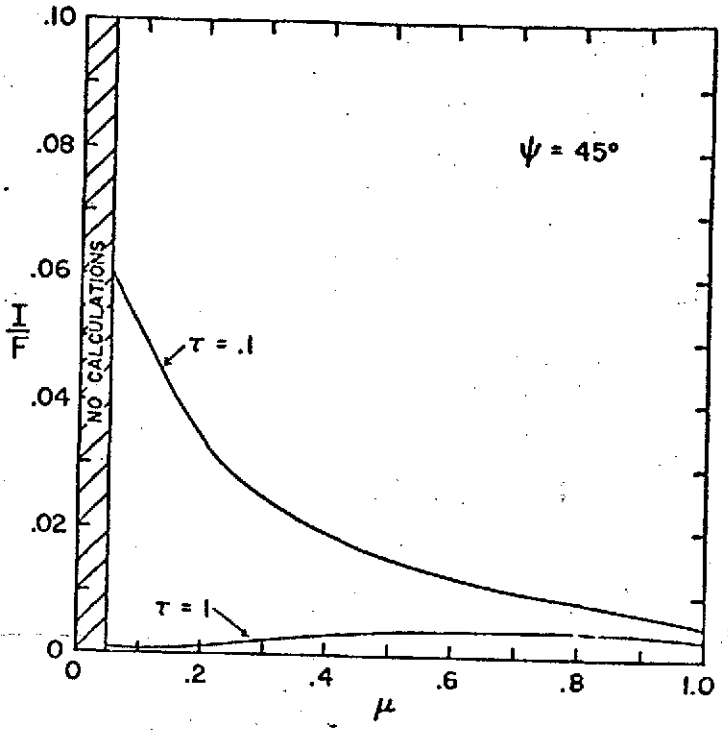

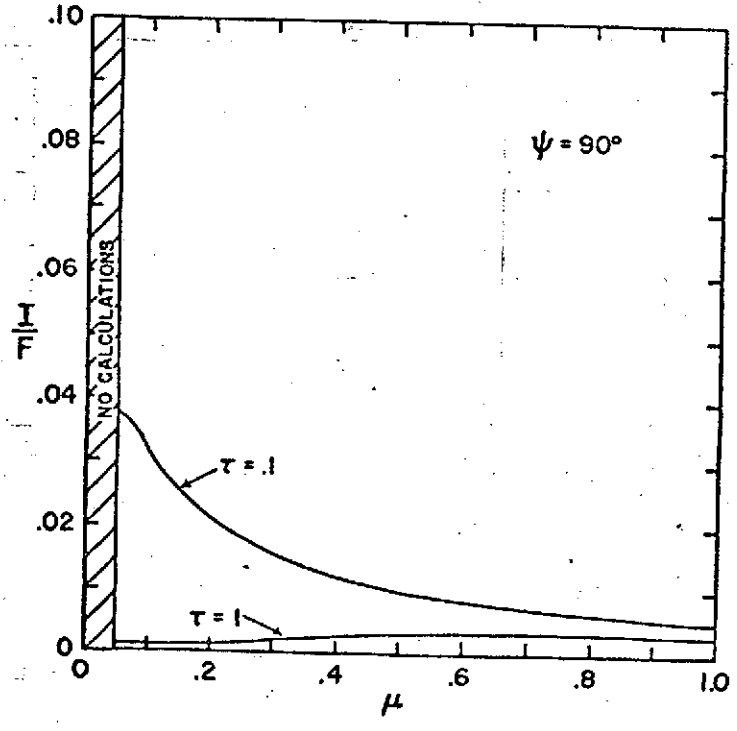

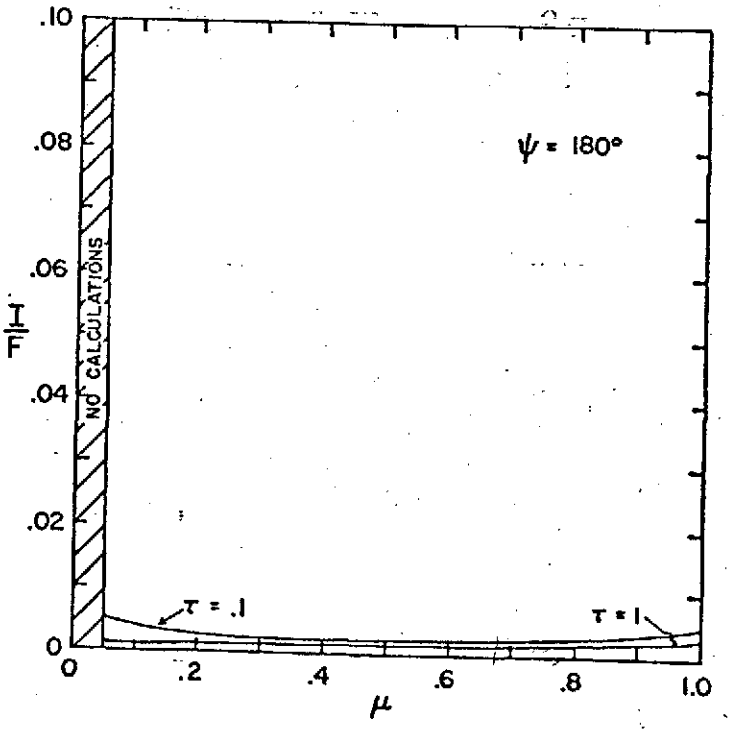

Fig. 3

REFLECTION: $X = -1$, $\mu_o = 0.05$, $\tilde{\omega} = 1$

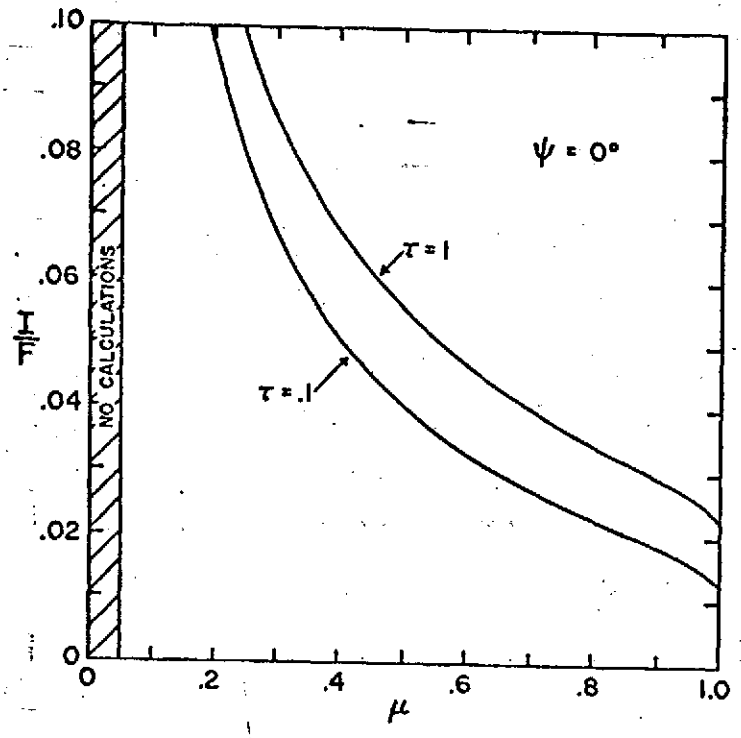

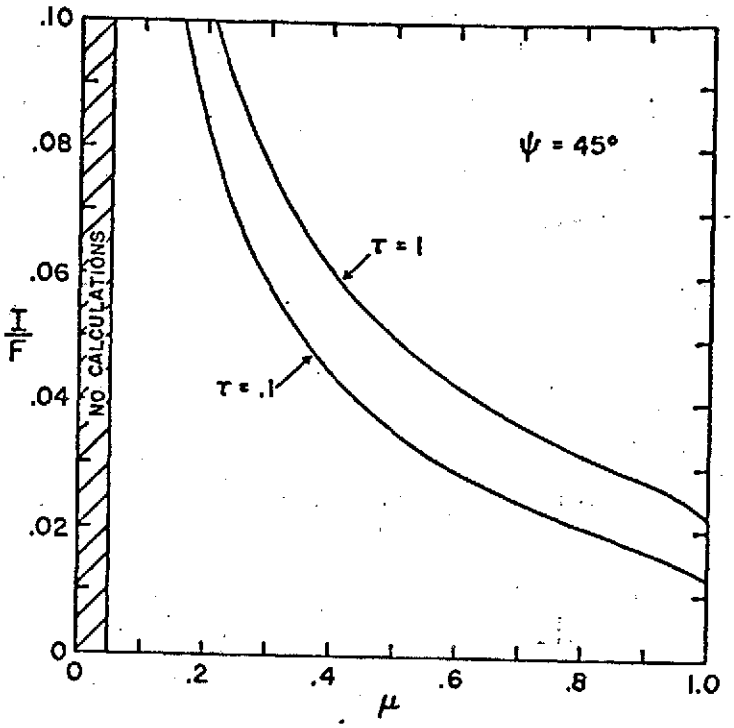

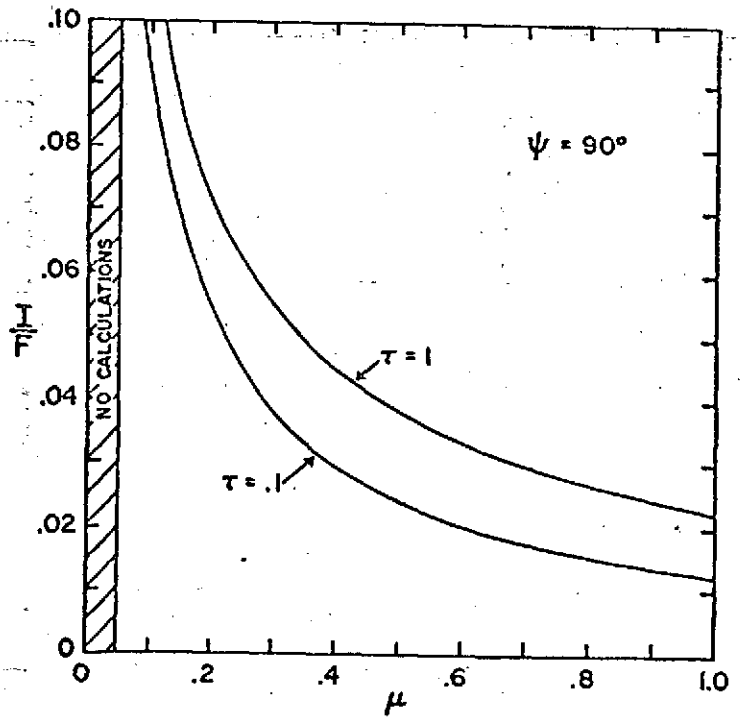

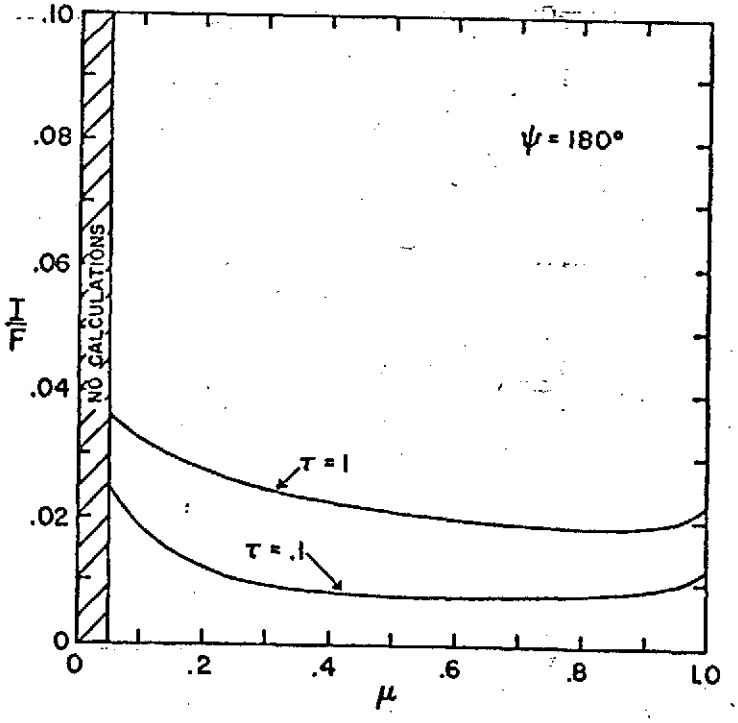

Fig. 4

TRANSMISSION: $X = -1$, $\mu_0 = 0.05$, $\tilde{\omega} = 1$

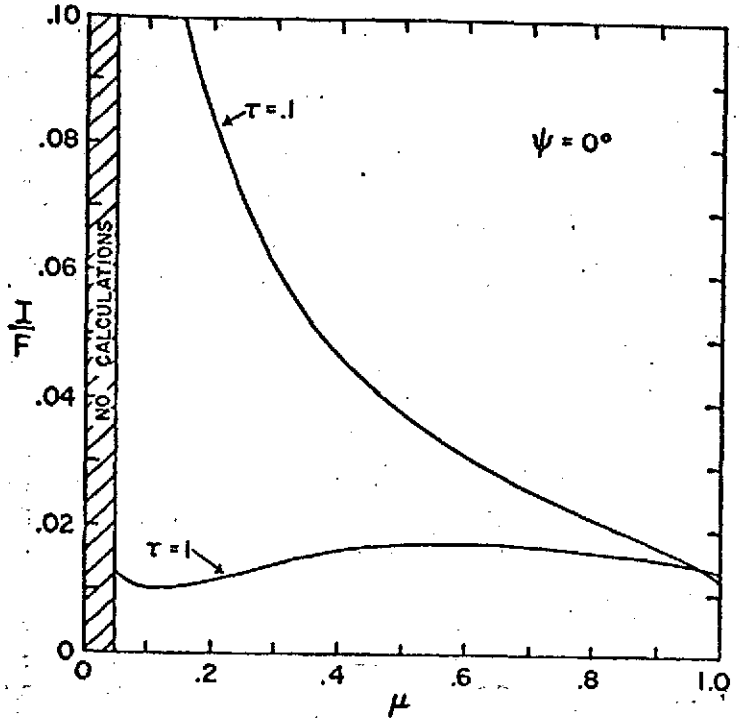

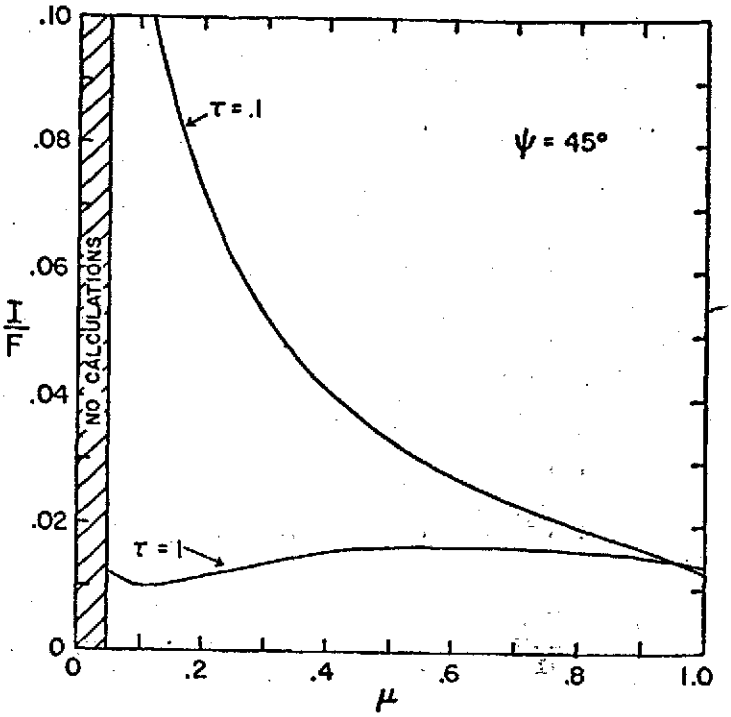

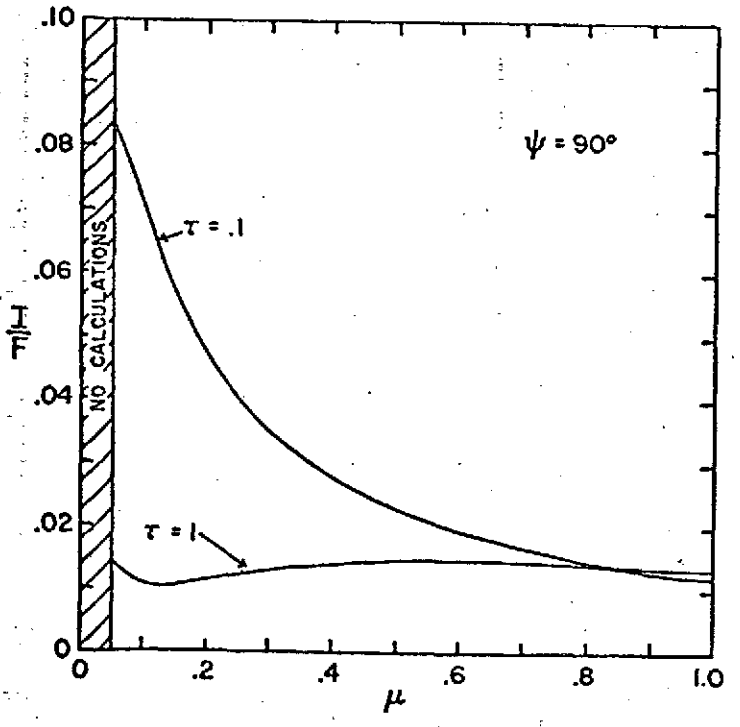

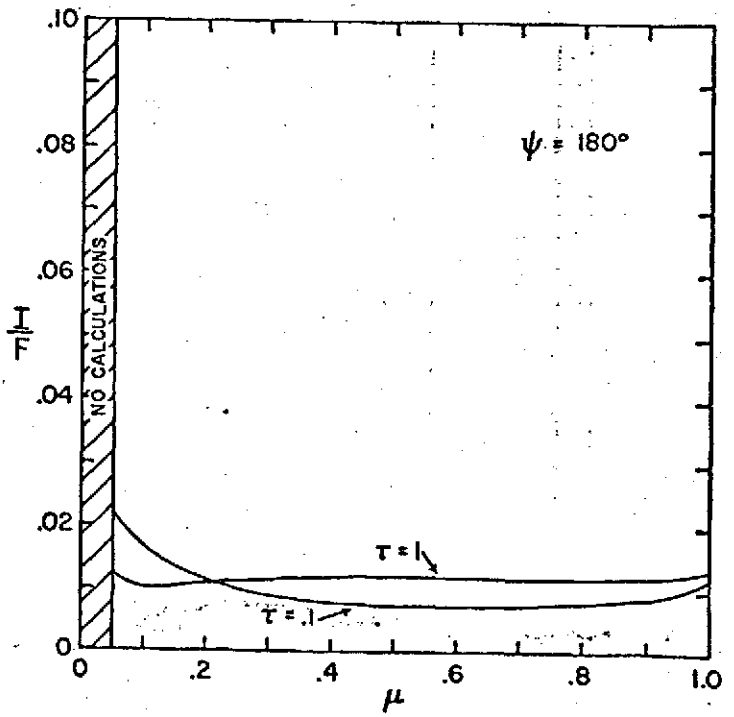

Fig. 5

ILLUMINATION OF SATURN'S RING BY THE BALL. I. DETECTION

Michael J. Price[+]
Planetary Science Institute
Tucson, Arizona 85704

Received_____

+ Visiting Astronomer, Kitt Peak National Observatory, which is operated by the Association of Universities for Research in Astronomy, Inc., under contract with the National Science Foundation.

No. of Copies: 4

No. of MS Pages: 19

No. of Figures: 5

No. of Tables: 0

ABSTRACT

Indirect solar illumination of Saturn's ring via scattering from the ball of the planet provides a new ground-based observational technique for studying the phase function of the individual particles. Essentially complete phase angle coverage can be achieved by studying the variation with azimuth of the indirect contribution to the surface brightness of the ring. Initial application of the technique is reported. The indirect contribution to the radiation scattered from the ring has been detected by electronographic areal photometry. The results have been interpreted using simple scattering models. Observational and theoretical problems involved in further development of the technique are briefly discussed.

I. INTRODUCTION

Remote sensing studies of Saturn's ring utilize information obtained at visual wavelengths regarding the single scattering albedo and phase function of the individual particles. From Earth, the phase of Saturn is never larger than 6 degrees. Unambiguous interpretation of photometry of direct sunlight suffering diffuse reflection from the ring is therefore difficult. Although Price (1973, 1974) has shown that the observational data may be explained by scattering from macroscopic ice particles, thorough investigation of the scattering properties of the ring particles properly requires photometry covering the entire range in phase angle (180^{o}). Since spacecraft missions could provide the necessary data, Price (1975) has made photometric predictions, based on the macroscopic ice particles' model, for the 1979 Pioneer 11 flyby. But missions to Saturn will be rare in the foreseeable future. Consequently, ring studies have real need for an Earth-based observational technique capable of providing thorough coverage in phase angle.

Complete phase angle information ($\pm 180^{o}$) can be obtained by treating the ball of Saturn as an auxiliary light source providing continuous indirect solar illumination of the ring surface. Areal photometry of the indirect contribution to the surface brightness can be used to thoroughly explore the shape of the scattering phase function. In essence, the technique is based on the direct dependence on longitude of the local scattering angle.

Initial application of the technique is reported in this paper. Electronographic areal photometry of the ring is presented. The data are discussed in terms of the basic optical scattering parameters of the ring using simple theoretical models. Observational and theoretical problems involved in further development of the technique are discussed.

II. OBSERVATION

To reliably detect and study the indirect contribution to the surface brightness of the ring, accurate areal photometry ($\sim$ 1 percent or better) is required. Conventional photography is not suitable because of difficulties in obtaining reliable calibration of the non-linear response of the emulsion. Although several alternative photometric techniques can provide linear response (e.g. electronography, photoelectric area-scanning, and the use of silicon diode vidicon devices), electronography offers several distinct advantages - spatial resolution, photometric accuracy, and efficiency in recording the observational data. Kron, Ables and Hewitt (1969) have discussed electronography, the Kron Camera, and its application in astronomy. Since their camera has a linear response at least to a density 4, it was selected for the task.

Observations were made early in December 1972. Conditions were then optimum. Saturn reached opposition on December 9, and the ring system was near its maximum opening. During the course of the observations, the planetocentric declinations of the Sun and Earth were $26^{o}.56$ and $26^{o}.39$,

respectively. Photometry was carried out using a Kron Electron Camera (KP1) on the nights of 1972 December 3/4 and 1972 December 4/5; one Kron plate was obtained each night. Unfiltered images of Saturn were obtained with the KPNO 50-inch Cassegrain reflector. On the basis of telescope image scale, the performance characteristics of the Kron Camera, the properties of the Ilford L-4 emulsion used, and the statistics of photographic grain, the Saturn plates were exposed to densities in the range 1 - 3 in order to obtain nominal photometric accuracy in the range 1 - 0.1 percent. Actual photometric accuracy is dependent on the uniformity of the photocathode response. Each plate contained six frames, with each frame consisting of five Saturn images of equal exposure. Exposure times for the plate taken on 1972 December 3/4 were 1/10th sec., 1/10th sec., 1/2 sec., 1 sec., 3 secs., and 10 secs.; on 1972 December 4/5, exposure times were 1 sec., 2 secs., 3 secs., 5 secs., 10 secs., and 20 secs. On both nights, seeing conditions were worse than average for Kitt Peak; half-intensity diameters of stellar images were ~ 2 arc sec. Laboratory calibration of the response and distortion of the tube was carried out on 1972 December 6 using uniform illumination of the photocathode by a point source, and an illuminated geometrical pattern. Within the central 1/3 diameter region of the photocathode, the response was uniform to $\pm$ 5 percent. Towards the edges of the photocathode, however, the sensitivity varied systematically by up to 20 percent. Only Saturn images contained within the central region were therefore selected for study. Across each selected Saturn

image, the tube sensitivity varied by not more than 1 percent. Geometrical distortion was found to be negligible. In all cases the Kron Tube was operated at 22.5 Kv. Plates were developed in Kodak D-19 for 5 minutes at 20^{o} C.

Of the sixty Saturn images recorded, two were selected for detailed study. Selection was based on seeing quality, photocathode uniformity, and density. Both images were obtained on 1972 December 4/5; their exposure times were 3 secs. and 5 secs. Thorough areal photometry of each image was carried out with the Kitt Peak PDS Microdensitometer using raster scanning. Plate scale was 32 arc sec. per mm. With a 16 μm square scanning aperture, the corresponding spatial resolution was 0.5 arc sec. By computer processing the microdensitometer data, radial profiles of density covering the entire range in position angle were obtained. Fig. 1 illustrates the geometry of the Saturn images. Taking the minor axis of the ring system as the zero reference line for position angle, radial profiles were obtained at 5 degree intervals throughout the range $\pm 180^{o}$. Complete profiles obtained from the pair of images for position angles in the range $\pm 90^{o}$ are reproduced individually in Figs. 2 and 3. Profiles corresponding to equal positive and negative position angles are superimposed at 10 degree intervals. For each complete profile across the Saturn image, photographic density is plotted against linear radial distance, measured in arbitrary units. With reference to Fig. 1, the left-hand sides

of all profiles refer to position angles, ψ, less than or equal to 90 degrees; the right-hand side, to position angles $(180 - \psi)$.

In searching for the indirect contribution to the surface brightness of the ring, our initial concern is with the general photometric quality of the images. Of major interest are photocathode uniformity and atmospheric seeing quality. Investigation of the photometric quality is constrained by lack of an absolute calibration. Only relative photometry within each Saturn image is available. In order to proceed, the geometrical symmetry of the Saturn system must be utilized. On the basis of current knowledge, longitudinal invariance of the radial physical structure of the ring is assumed. Both atmospheric seeing quality and photocathode uniformity are most easily examined by considering radial scans along the major axis of the ring (position angle 90°). With reference to Figs. 2 and 3, invisibility of the Cassini division and the non-zero sky background between the ball of Saturn and the ring both testify to our earlier estimate of seeing quality. Near equality between the ansae testify to the uniformity of the photocathode over each Saturn image. Close matching ($\sim \pm$ 1%) between all radial profiles of equal positive and negative position angle is also a strong indication of uniformity both in the photocathode sensitivity and in the seeing quality. Photoelectric symmetry with respect to the Saturn-Sun line is apparent. Before discussing the evidence for indirect solar illumination of the ring, however, two major influences on the apparent surface brightness must first be disentangled viz., disk occultation and seeing effects.

For large position angles, the ring system suffers occultation by the planet. Occultation of ring C, the faintest component of the system, begins to occur at position angles $\pm 110^{o}$; it is complete for position angles greater than $\pm 130^{o}$. Ring B occultation begins at position angles $\pm 125^{o}$; occultation is complete by $\pm 155^{o}$. Ring A occultation begins at position angles $\pm 155^{o}$; it remains partial even for position angles $\pm 180^{o}$. Occultation of rings A and B is readily apparent in the corresponding radial photometric profiles (Figs. 2 and 3). Since ring B is the most prominent component of the system, its occultation has a particularly noticeable effect. By comparison, the effect of ring C occultation is negligible. Our search for evidence of indirect solar illumination of the ring will, therefore, avoid position angles greater than $\pm 120^{o}$.

Through spatial redistribution of radiant energy, seeing conditions have a significant influence on the radial photometric profiles of the ring. Seeing effects reduce the apparent surface brightness of celestial objects. Every spatial element of an extended source is subjected to the seeing spread function, so that partial redistribution of its radiant energy to neighboring elements occurs in the image plane. Increasing angular spread in the energy distribution results in a decrease in apparent surface brightness. Magnitude of the effect is dependent on the relative angular diameters of the source and point spread function; it becomes significant when their relative angular diameters are comparable. Such is the case for our Saturn ring observations. Effective angular widths of each ansae (rings A and B only), measured along the major axis of the ring, are ~ 6 arc sec. In the perpendicular direction,

the effective angular width of the ring is 3 arc sec. By comparison, the intensity half-width of the point spread function is 1-2 arc sec. Significant variation in the apparent surface brightness of the ring with position angle can then be expected. Surface brightness should reach a maximum for position angles $\pm 90^{\circ}$; it should be a minimum for position angles 0°, $\pm 180^{\circ}$. In accordance with expectation, Figs. 2 and 3 do indeed show a maximum for a position angle of 90°.

To disentangle the effects of atmospheric seeing spread and instrumental scattering, the geometric and photometric symmetry of the Saturn images can be utilized. Effects not due to indirect solar illumination of the ring may be eliminated to first order by comparing radial profiles which correspond to equal angles with respect to the major axis of the ring (Fig. 1). For example, comparisons between the following position angles may be made: 60° and 120°, 70° and 110°, 80° and 100°. At the same time, the major effects of the indirect solar illumination of the ring are preserved. Bearing in mind that radial profiles corresponding to equal positive and negative position angles are interchangeable, the relevant comparison may be made between opposite sides of the radial profiles $\pm 60^{\circ}$, $\pm 70^{\circ}$, $\pm 80^{\circ}$. All three comparisons (Figs. 2 and 3) indicate that the maximum surface brightness of the ring is $\sim 3 \pm 1\%$ higher on the sunward side. Data at the intermediate position angles $\pm 65^{\circ}$, $\pm 75^{\circ}$ and $\pm 85^{\circ}$, show the same effect. The anomalous brightening of the ring on the sunward side may be interpreted as due to indirect solar illumination of the ring via the ball of the planet.

III. INTERPRETATION

Our estimate of the relative indirect contribution to the surface brightness of the ring must first be converted to an absolute scale. To do so, the effective observational wavelength must be determined. Unfortunately, during the time when the Saturn observations were carried out, the Kron Camera (KP1) was still in the development stage. In order to expedite the project, it was necessary to image Saturn onto the photocathode with no wavelength filtering. Consequently, the effective wavelength could not be accurately selected. Even so, it can be estimated approximately by considering the spectral response of the photocathode (S-11) in relation to the spectral reflectivity of the ring determined by Lebofsky, Johnson and McCord (1970). Peak photocathode sensitivity occurs near $\lambda \sim 4000$Å; it deteriorates to near-zero for $\lambda \sim 6000$Å. By comparison, the spectral reflectivity of the ring is very low for $\lambda \sim 4000$Å, reaching a maximum for $\lambda \sim 6000$ Å. On balance, the net effective wavelength will be $\lambda \sim 5000$Å.

Published photometry of the direct contribution to the surface brightness of the ring have been used to calibrate the indirect contribution. Relevant data, taken under essentially identical geometrical conditions, have been published by Franklin and Cook (1965). Their measurements have been interpreted by Price (1973, 1974) in terms of an equivalent I/F value, where the mean specific intensity over the ring surface (rings A and B only) is denoted I, and πF is the solar flux at Saturn. Taking into account the

phase effect, the direct I/F contribution relevant to our observations is ~ 0.35. In absolute terms, therefore, our estimate of the relative indirect contribution to the mean surface brightness of the ring is given by $I/F \sim 0.011 \pm 0.003$.

In order to compute the indirect solar illumination of the ring, the behaviour of Saturn as a light source must be modelled. To a first approximation, the Saturnian cloud layer will be treated as a uniform Lambert scattering surface. In addition, the planet will be taken as spherical (radius 60,400 kms); its oblateness will be ignored. Photometry indicating departures from Lambert scattering by the ball of Saturn have been published recently by Binder and McCarthy (1973). But, for our present purpose, such departures are not significant. Neither is the neglect of planetary oblateness. Determination of the equivalent Lambert surface albedo, a, is essential to the computation. Measurements of the geometrical albedo, p, can be readily converted to Lambert surface albedo, a. For example, a Lambert sphere of unit surface albedo has a geometrical albedo of 2/3. Irvine and Lane (1971) have published spectral measurements of the geometrical albedo of Saturn. For an effective observational wavelength $\sim\lambda$ 5000Å, the corresponding geometrical albedo, p (λ5012Å), was found to be 0.371. The equivalent Lambert surface albedo, a, is 0.55.

Our principal objective in the analysis is to determine if the observational results are consistent with current knowledge of the ring; if not, to explain the discrepancy. Our basic ring model will assume the system to

be opaque; radiation incident on the ring will be considered to come from one hemisphere only. More specifically, the perpendicular optical thickness of the ring will be taken as infinite. Our attention will be concentrated on ring B, since it is the most opaque portion of the system and should contribute most to the scattering of indirect solar radiation. Computations will be restricted to the mid-point of ring B, corresponding to a radial distance from the center of the planet of 1.75 Saturn equatorial radii. Two extreme optical scattering models for the ring will be examined.

In Model I, the ring scatters like an opaque Lambert surface. The scattering properties of a semi-infinite, conservative, isotropic scattering model are well approximated by Lambert's law. Model I, therefore, can be used to obtain a coarse estimate for the probable magnitude of the indirect contribution to the surface brightness of the ring. Information concerning the variation with azimuth of the indirect illumination of the ring is also provided. An estimate of the equivalent Lambert surface albedo, b, is required. Its value can be inferred from the relevant direct I/F value. For direct illumination of a Lambert surface, I/F equals $b\mu_0$, where μ_0 is the cosine of the angle of incidence with respect to the outward normal. Our observational data correspond to μ_0 equal to 0.447. For I/F equal to 0.35, the corresponding b value is 0.78. Predictions of the variation of the indirect I/F value with azimuth angle are shown in Fig. 4. Ordinates are $\frac{I}{F} \cdot \frac{1}{ab}$. With the adopted values for a and b, the maximum indirect I/F value, occurring at zero azimuth angle, is 0.017. The relative difference between the indirect I/F values for position angles 60° and 120° is 0.0051.

Note that position angle and azimuth angle are not equivalent. For the particular geometry of the situation, the position angle 60^{o} corresponds to the azimuth angle $75^{o}.5$; the position angle 120^{o}, to azimuth angle $104^{o}.5$ The prediction may be compared with the observational determination ($\sim 0.011 \pm 0.003$). Since our estimate for the surface albedo of the ring is based on the average direct $\frac{I}{F}$ for rings A and B together, the b-value will necessarily be underestimated for the mid-point of ring B. Theory and observations are therefore not inconsistent.

Model II is designed to illustrate the dependence of the indirect contribution to the surface brightness of the ring on the scattering phase function of the individual particles. It consists of a semi-infinite layer of non-conservatively scattering particles. Their scattering phase function is given by

$$p(\textcircled{H}) = \tilde{\omega}(1 + x \cos \textcircled{H})$$

where $\tilde{\omega}$ is the single scattering albedo, x is the anisotropy parameter, and $\textcircled{H}$ is the scattering angle. To maximize the influence of the individual phase function on the indirectly incident solar radiation, primary scattering alone will be considered. Scattering will tend, therefore, to be underestimated. But neglect of multiple scattering becomes progressively less significant as the single scattering albedo decreases. Variation with azimuth angle of the indirect contribution to the surface brightness of the ring is illustrated in Fig. 5. Ordinates are $\frac{I}{F} \cdot \frac{1}{a\tilde{\omega}}$. Three distinct values for the anisotropy

parameter are used. Pronounced back-scattering (x = -1), isotropic scattering (x = 0), and pronounced forward-scattering (x = 1), are all considered. On the basis of recent analyses by Price (1973, 1974) of the scattering of direct solar radiation from the ring, the most relevant combination of parameters deals with pronounced back-scattering (x = -1) for single scattering albedos greater than 0.75. In principle, discrimmination between scattering phase functions is not readily achieved by studying azimuth angles less than 60^{o}. Since effects of varying the anisotropy parameter are not pronounced in the azimuth range 60^{o} to 120^{o}, our present observational data are not suitable for determining its optimum value. However, if reliable data can be obtained at azimuth angles less than 60^{o}, excellent discrimination between scattering phase functions should be possible. Inclusion of multiple anisotropic scattering in the theoretical computations will be required to match the observations.

IV. DISCUSSION

In view of the difficult nature of the observations, our results should be considered tentative. Even so, utilizing indirect solar illumination of the ring promises to be an effective photometric technique for studying its basic scattering parameters. The technique should be particularly useful for inferring the shape of the scattering phase function of the individual ring particles. Further development of the technique is under way. Absolute areal photometry of the ring will be carried out with special attention given to minimizing problems introduced by inferior atmospheric seeing conditions. Results will be reported in due course.

ACKNOWLEDGEMENTS

It is a pleasure to thank L. Goldberg for granting telescope time for the project and for providing access to the data analysis facilities of the Kitt Peak National Observatory; A. A. Hoag for this personal assistance at the telescope to insure the success of the project; I. Furenlid for assistance in operating the Kitt Peak PDS Microdensitometer; and L. Baker for carrying out the data reduction. This research was supported by the National Aeronautics and Space Administration under contract NASW-2521.

REFERENCES

Binder, A.B. and McCarthy, Jr., D. W. (1973) "IR Spectrophotometry of Jupiter and Saturn", Astronomical J. 78, 939.

Franklin, F. A. and Cook, A. F. (1965) "Optical Properties of Saturn's Ring. II. Two Color Phase Curves of the Two Bright Rings", Astronomical J. 70, 704.

Irvine, W. M. and Lane, A. P. (1971) "Monochromatic Albedos for the Disk of Saturn", Icarus 15, 18.

Kron, G. E., Ables, H. D., and Hewitt, A. V. (1969) " A Technical Description of the Construction, Function, and Application of the U. S. Navy Electronic Camera", In "Advances in Electronics and Electron Physics", Vol. 28A. Ed. L. Morton, Academic Press, 1969, p. 1.

Lebofsky, L. A., Johnson, T.V. and McCord, T. B. (1970) "Saturn's Rings: Spectral Reflectivity and Compositional Implications", Icarus 13, 226.

Price, M. J. (1973) "Optical Scattering Properties of Saturn's Ring", Astronomical J. 78, 113.

_____ (1974) "Optical Scattering Properties of Saturn's Ring. II", Icarus (in press).

_____ (1974) "Saturn's Ring and Pioneer 11", Icarus (in press).

FIGURE CAPTIONS

Fig. 1: Geometrical aspect of Saturn on 1972 December 4/5. To an excellent approximation, the planet is taken to be at opposition (1972 December 9). Relevant planetocentric declinations of the Sun and Earth are $-26^{\circ}.56$ and $-26^{\circ}.39$, respectively. Position angles, θ, are measured from the Saturn - Sun/Earth line. Radial limits of the individual ring components are shown. South is located at the top of the diagram.

Fig. 2: First selected Kron Electron Camera image of Saturn obtained on 1972 December 4/5 with the Kitt Peak 50-inch aperture reflector. An exposure time of 3 secs. was required. Complete PDS Microdensitometer scans through the image center for position angles, θ, in the range zero through 90 degrees are shown. The sunward end of each scan is located on the left side of each profile. The microdensitometer scan utilized a nominal spatial resolution corresponding to 0.5 arc sec. Ordinates refer to the photographic density; abscissae, to distance in the image plane. Both axes are calibrated in uniform but arbitrary units. For the scan along the major axis of the ring, the peak ansae densities are ~ 2.25.

Fig. 3: Second selected Kron Electron Camera image of Saturn obtained on 1972 December 4/5 with the Kitt Peak 50-inch aperture reflector. An exposure time of 5 secs. was required. Complete PDS Microdensitometer scans through the image center for position angles, θ, in the range zero through 90 degrees are shown. The sunward end of each scan is located on the left side of each profile. The microdensitometer scan utilized a nominal spatial resolution corresponding to 0.5 arc sec. Ordinates refer to the photographic density; abscissae, to distance in the image plane. Both axes are calibrated in uniform but arbitrary units. For the scan along the major axis of the ring, the peak ansae densities are ~ 3.15.

Fig. 4: Theoretical predictions of Lambert scattering from Saturn's ring for indirectly incident solar radiation via reflection from the ball of the planet. The calculations refer to the mid-point of ring B, corresponding to a distance of 1.75 Saturn radii from the center of the planet. Saturn is taken as spherical, radius 60,400 kms. A negative planetocentric solar declination angle $26^{\circ}.56$, corresponding to 1972 December 4/5 is assumed. The Lambert surface albedo of Saturn and its ring, denoted a and b respectively, are taken as arbitrary. Ordinates are $\frac{I}{F} \cdot \frac{1}{ab}$ where I is the specific intensity of the ring surface; πF is the solar flux at Saturn. Abscissae are azimuth angles

measured in the ring plane; zero corresponds to the projected Saturn-Sun line.

Fig. 5: Theoretical predictions of anisotropic scattering from Saturn's ring for indirectly incident solar radiation via reflection from the ball of the planet. The perpendicular optical thickness of the ring is taken as infinite. Primary scattering only is considered. The scattering phase function used is of the form $\tilde{\omega}(1 + x \cos \Theta)$. Where $\tilde{\omega}$ is the single scattering albedo, Θ is the scattering angle, and x is the anisotropy parameter. Three x-values are considered, viz., pronounced back-scattering ($x = -1$), isotropic scattering ($x = 0$), and pronounced forward scattering ($x = 1$). Saturn is assumed to be at opposition. The calculations refer to the mid-point of ring B, corresponding to a distance of 1.75 Saturn radii from the center of the planet. Saturn is taken as spherical, radius 60,400 kms. Assumed planetocentric declinations of the Sun and Earth, corresponding to 1972 December 4/5, are $-26^{\circ}.56$ and $-26^{\circ}.39$ respectively. The Lambert surface albedo of Saturn, a, and the single scattering albedo, $\tilde{\omega}$, are taken as arbitrary. Ordinates are $\frac{I}{F} \cdot \frac{1}{a\tilde{\omega}}$ where I is the specific intensity of the ring surface; πF is the solar flux at Saturn. Abscissae are azimuth angles measured in the ring plane; zero corresponds to the projected Saturn-Sun line.

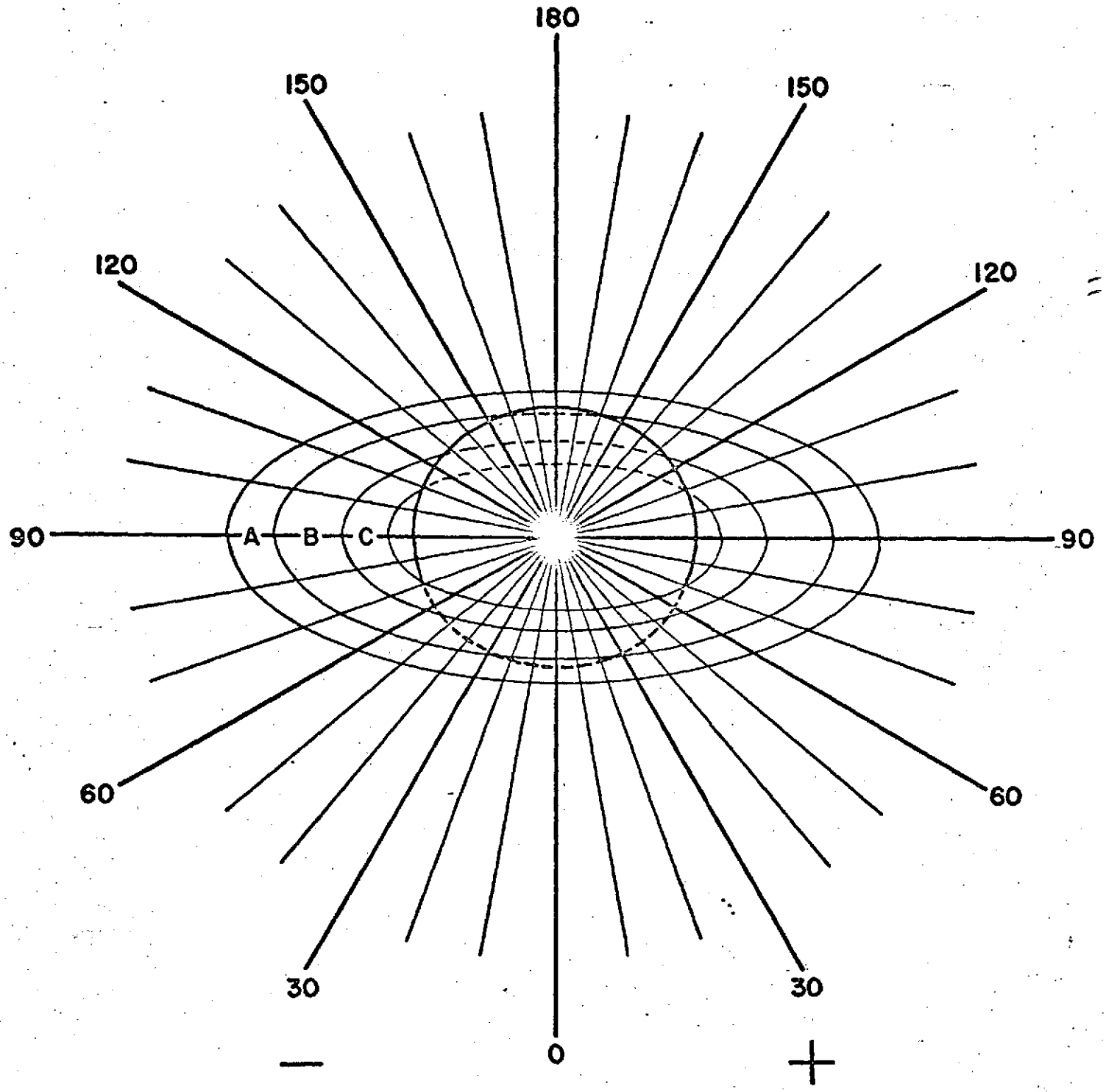

Fig. 1

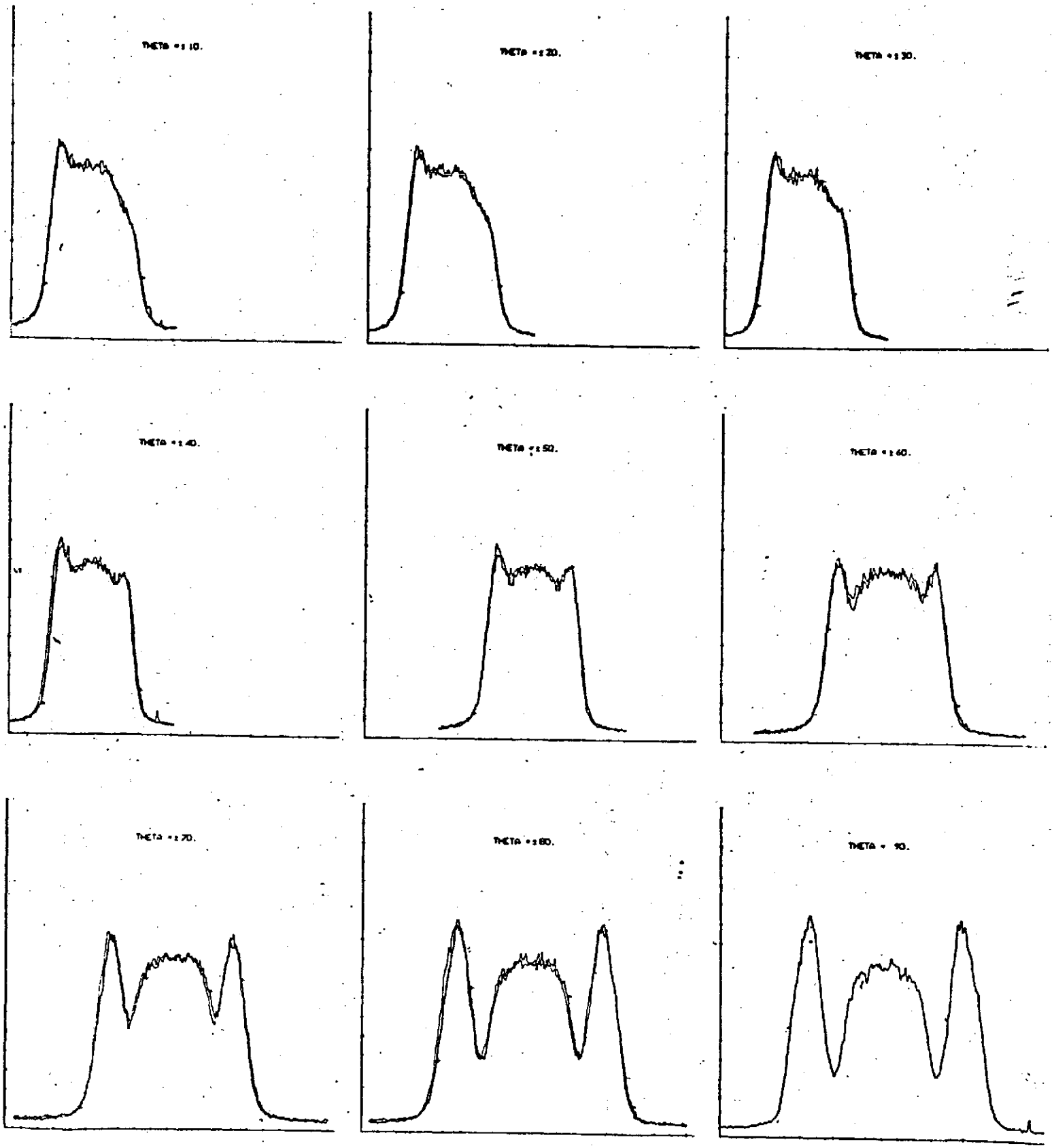
THETA = ± 10.
THETA = ± 20.
THETA = ± 30.
THETA = ± 40.
THETA = ± 50.
THETA = ± 60.
THETA = ± 70.
THETA = ± 80.
THETA = 90.

Fig. 2

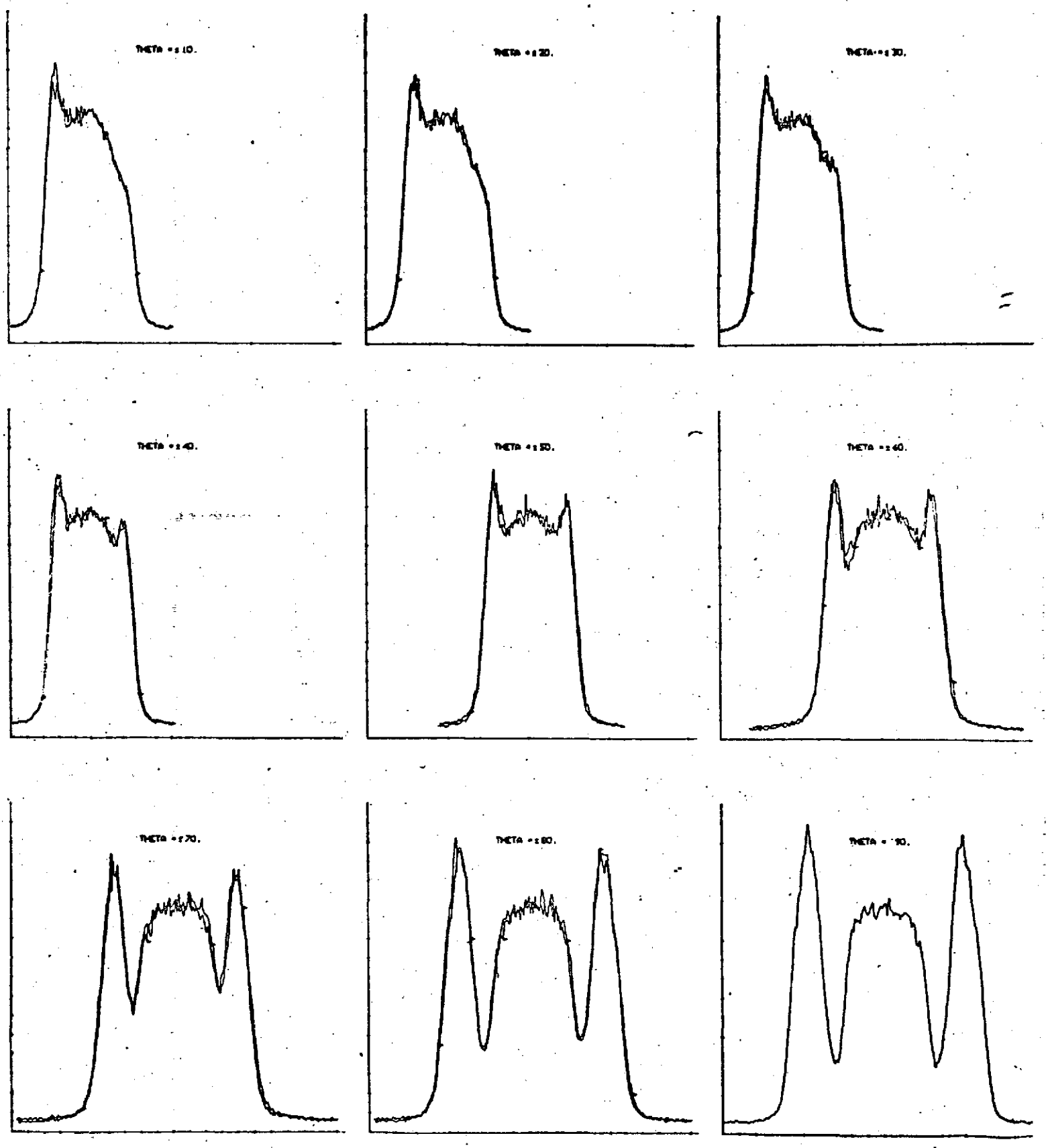
THETA = ± 10.
THETA = ± 20.
THETA = ± 30.
THETA = ± 40.
THETA = ± 50.
THETA = ± 60.
THETA = ± 70.
THETA = ± 80.
THETA = 90.

Fig. 3

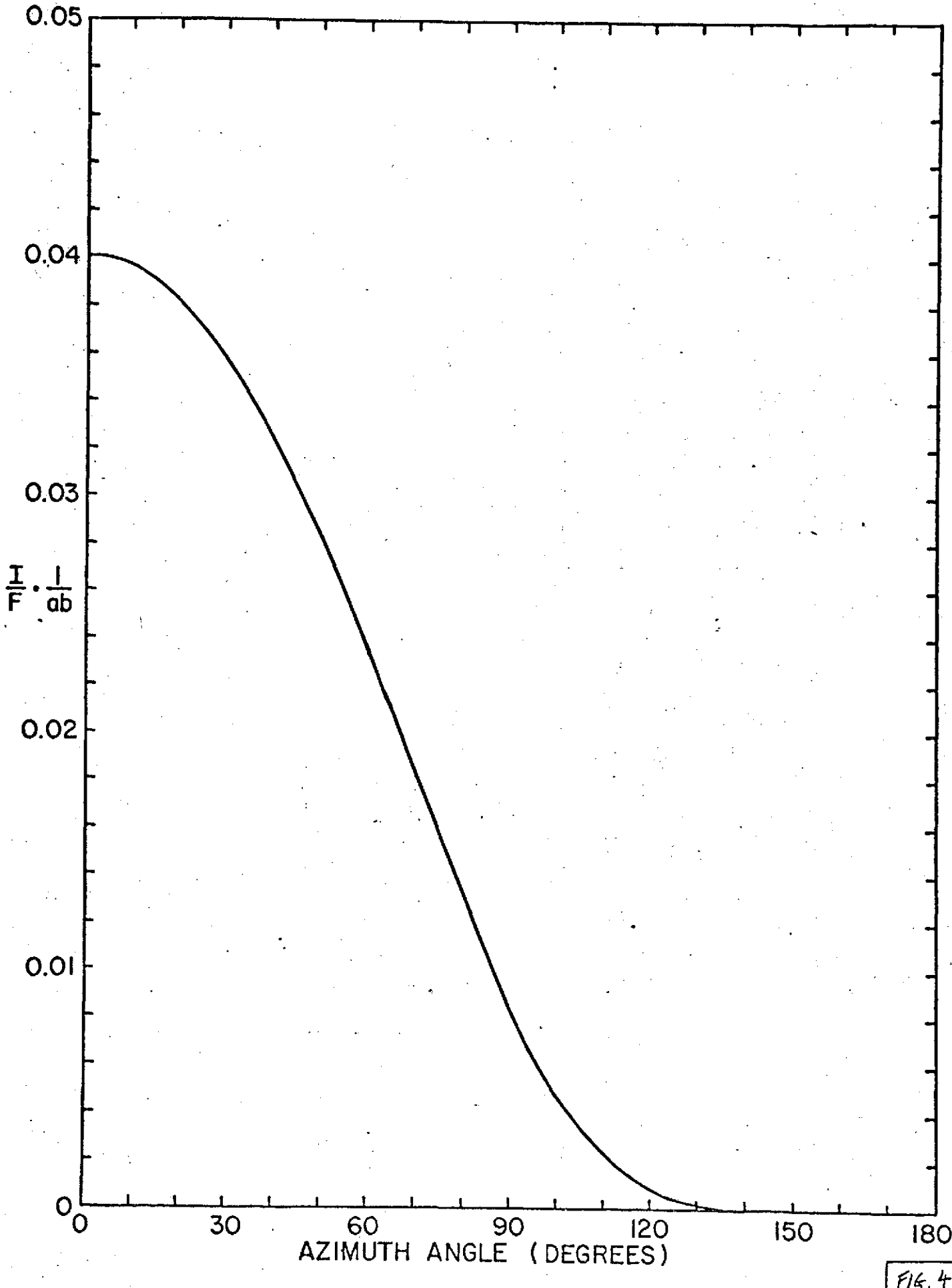
0.05
0.04
0.03
0.02
0.01
0
$\frac{I}{F} \cdot \frac{1}{ab}$
0
30
60
90
120
150
180
AZIMUTH ANGLE (DEGREES)

FIG. 4

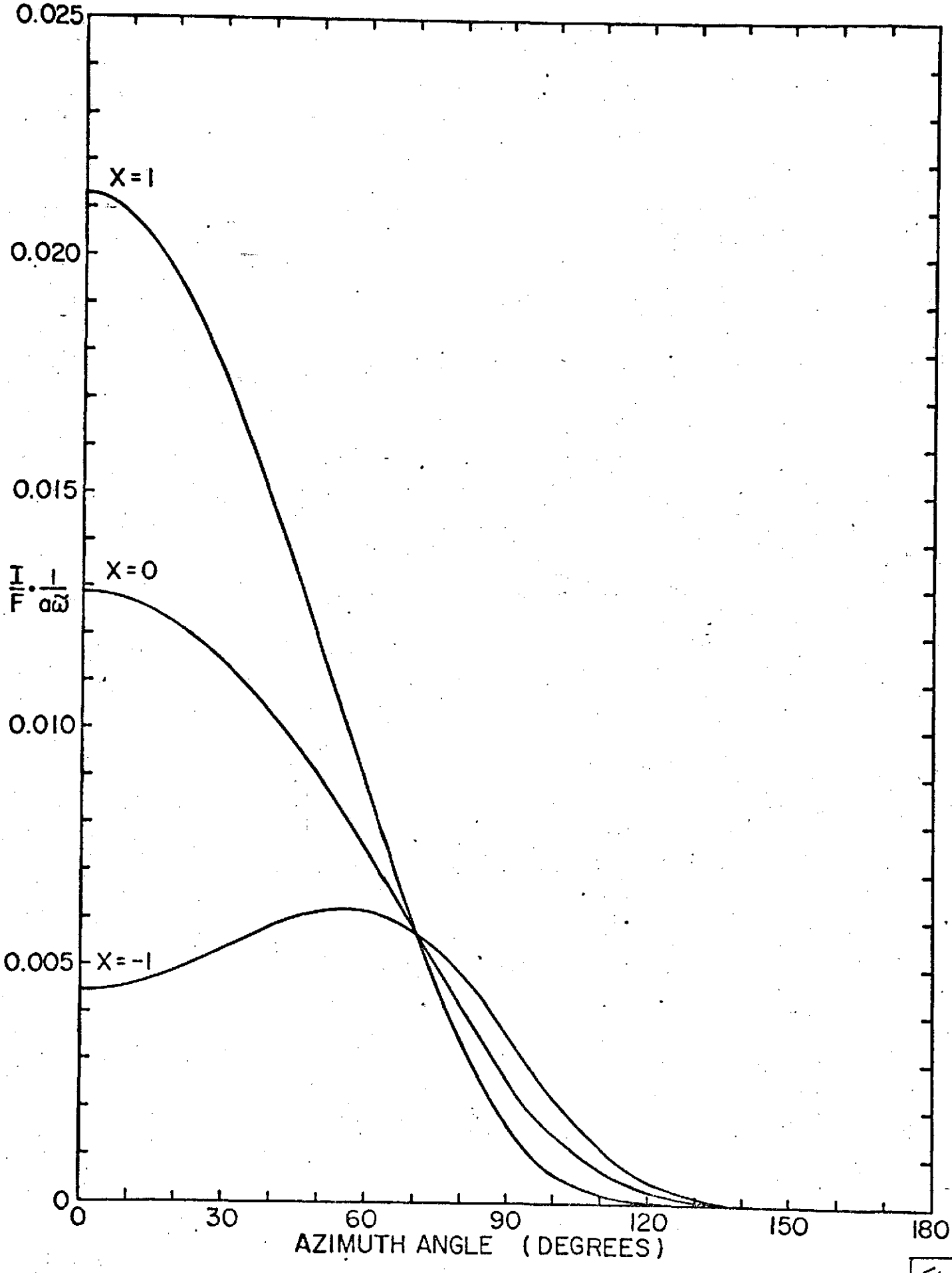
0.025
0.020
0.015
0.010
0.005
0
X = 1
X = 0
X = -1
$\frac{I}{F} \cdot \frac{1}{a\tilde{\omega}}$
0
30
60
90
120
150
180
AZIMUTH ANGLE (DEGREES)

Fig. 5

[redacted]

PLANETARY SCIENCE INSTITUTE

SMALL BODIES AND THE OUTER PLANETS

NASW-2521

Final Report

August, 1974

Submitted by:

Planetary Science Institute
252 W. Ina Road, Suite D
Tucson, Arizona 85704

William K. Hartmann
Manager

TABLE OF CONTENTS

TASKS 1 AND 3: ASTEROID RECONNAISSANCE SPECTROPHOTOMETRY AND DETAILED STUDIES OF SPECIFIC ASTEROIDS
(Principal Investigator: Clark R. Chapman)

INTRODUCTION

This section of the Final Report is devoted to the spectrophotometric observations of asteroids and their interpretation. This report will not repeat the remarks and data presented in the first three Quarterly Reports. I begin with a discussion of some of the fourth quarter work and precede to a more orderly analysis of all the data obtained and interpretations that have been made of the data and of the relationship between asteroids and meteorites.

FOURTH QUARTER RESEARCH

During the final quarter, reductions were completed for the data obtained during February 1974. As described in the Third Quarterly Report, data taken in May 1974 appear to be subject to a malfunction of the tape-recording system. There remains some hope that the data may be salvaged, but it will take more effort than is normally the case. Anyway the data are not presently available for reduction and interpretation.

In the final quarter there were two more observing runs at Kitt Peak National Observatory (on the No. 2 36-inch telescope). The first run was of ten nights duration (July 12-21, 1974) and the second run of 6 nights duration (August 1-6, 1974). The observational phases of this program are conducted jointly with T. McCord of MIT. Despite extremely bad luck with the weather conditions, data were obtained on 14 objects.

It had been intended that these runs would be devoted to detailed studies of (a) spectral variations with rotation and (b) infrared absorption bands. All clear periods were restricted to a few hours duration so that rotation studies were difficult to do; nevertheless asteroids 1, 2, 3, 8, and 19 were studied in this manner. The quality of the skies did not permit the detailed absorption band studies contemplated, although the data obtained should yield improved absorption band data incidentally.

Improved observations were also obtained for asteroids 18 and 115, both previously observed. Additionally, observations were obtained for 7 objects never previously observed: 45, 54, 56, 103, 124, 694, and 737.

There has been insufficient time as of this writing to reduce the July and August data, but they will be reduced and studied during the forthcoming year as part of another contract originating from the same NASA office.

Much of the final quarter was spent doing a variety of theoretical and interpretational studies which are reflected in the sections below. It will be

seen that great promise in understanding the early history of the solar system may be derived from these observations.

THE OBSERVATIONS

Spectrophotometry of minor planets in the visible and near-infrared has revealed a diversity of asteroid compositions with significant implications for the early history of the solar system. In a series of papers (the latest ones being McCord and Chapman, 1975a, b), Chapman and McCord have presented spectral reflectance curves for 67 asteroids. These observations have been interpreted and related to meteorites in another group of articles, the more recent ones being: Chapman and Salisbury (1973); McCord and Gaffey (1974); Gaffey (1974); Gaffey and McCord (1974); Chapman, Morrison, and Zellner (1975); Chapman (1974); and Chapman (1975).

I report here further spectrophotometric observations of nine asteroids previously observed and of 31 additional asteroids. The total number of asteroids observed by this technique is now 98. The data were obtained at Kitt Peak National Observatory on the 1.3-meter reflector during two observing runs: September 24-30, 1973 and February 11-14, 1974.

As I will describe below, several asteroids we observed have unusual and important spectra. In particular, 349 Dembowska has an absorption band as deep as that of Vesta, but appears to closely resemble LL6 type ordinary chondrites in spectral reflectance characteristics. More than a third of the new asteroids studied have spectra resembling laboratory spectra of type 2 carbonaceous chondrites; several of these have also been found to have very low albedos by Zellner et al (1974). It now appears that this dark, carbonaceous compositional class may be the dominant one in the asteroid belt.

The instrumentation, observing procedures, and data reduction techniques are similar to those previously described (McCord and Chapman, 1975a; Chapman et al, 1973a), except for the following modifications: The narrowband interference filter set was augmented so as to improve our spectral resolution in the near-infrared. S-1 and S-20 detectors were used during both observing runs. Also during the September run we frequently used a gallium-indium-arsenide "B" photomultiplier, sensitive to about 0.95 μm. Usually the S-1 data were taken in the last ten filters in a sequential mode of 45-second integrations per filter. These data were scaled to unity at 0.56 μm by matching to the overlapping S-20 or gallium-arsenide observations.

The spectral reflectance data for the 31 new asteroids are presented in Figure 1. They are scaled to unity at 0.56 μm. The lines are eye fits to the data. The error bars were determined from the internal consistency of individual runs except that they are never reduced to less than $\pm$ 0.03 in order to reflect my estimates of the systematic biases potentially existing in the calibration. A possible example of such a calibration problem is the

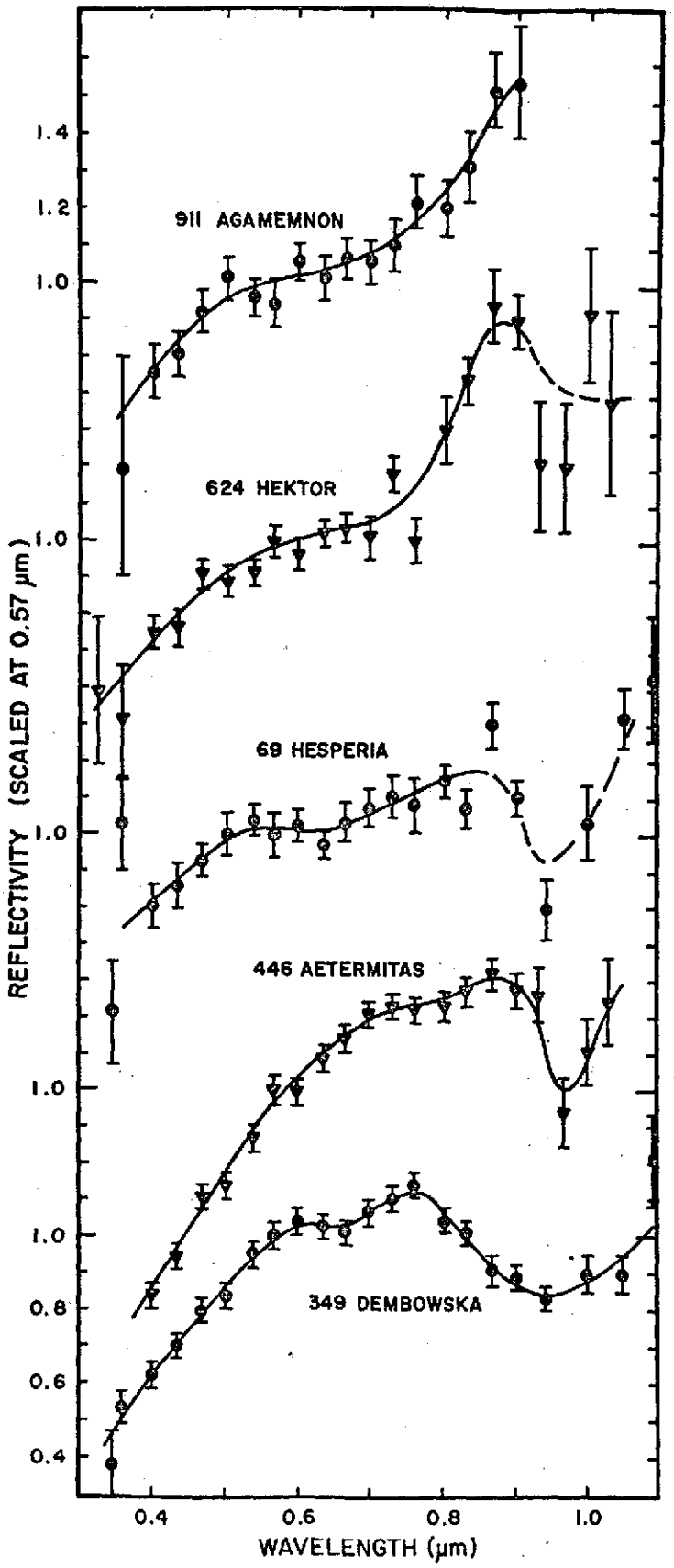
911 AGAMEMNON
624 HEKTOR
69 HESPERIA
446 AETERMITAS
349 DEMBOWSKA
REFLECTIVITY (SCALED AT 0.57 μm)
WAVELENGTH (μm)
1.4
1.2
1.0
1.0
1.0
1.0
1.0
0.8
0.6
0.4
0.4
0.6
0.8
1.0

FIGURE 1a

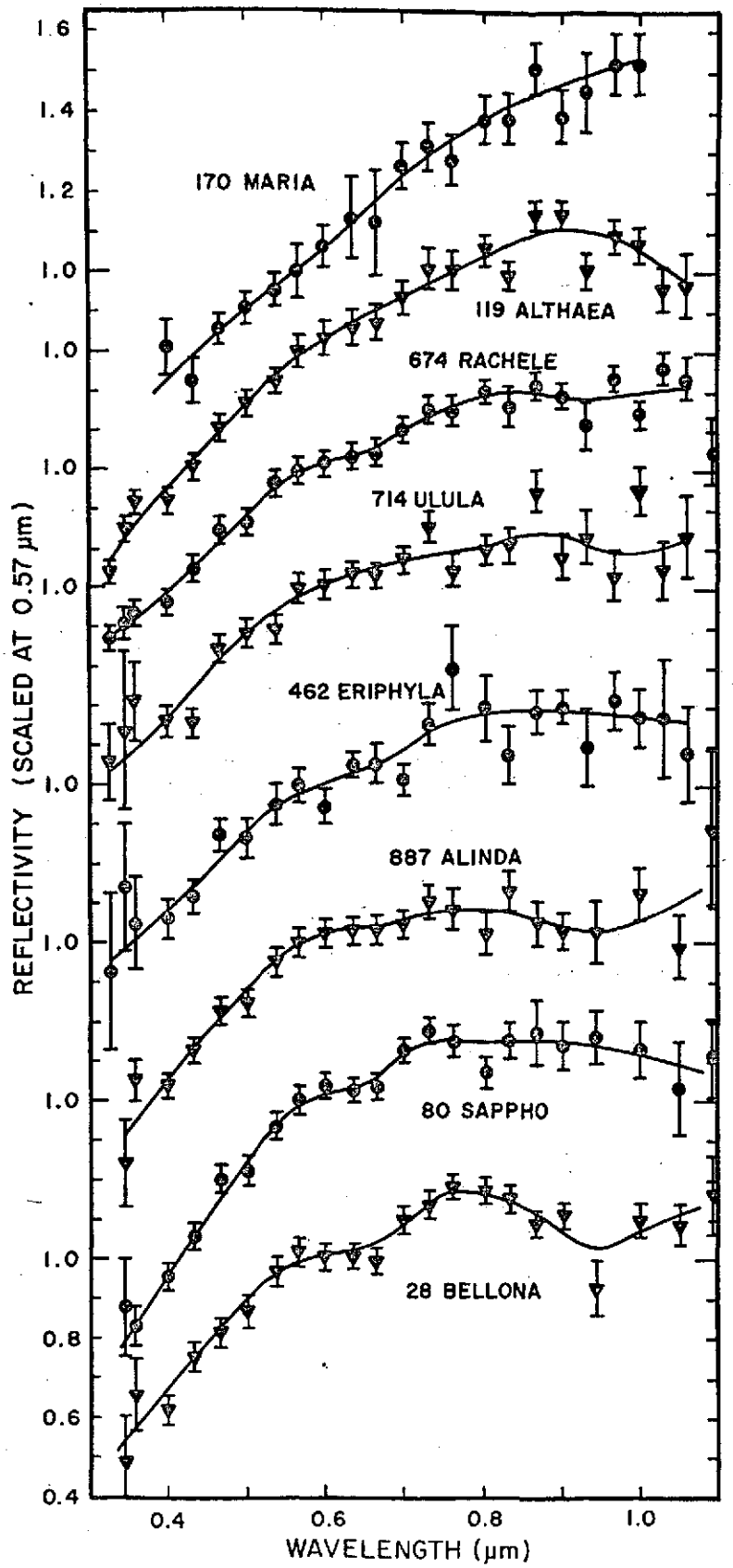
170 MARIA
119 ALTHAEA
674 RACHELE
714 ULULA
462 ERIPHYLA
887 ALINDA
80 SAPPHO
28 BELLONA
REFLECTIVITY (SCALED AT 0.57 μm)
WAVELENGTH (μm)
1.6
1.4
1.2
1.0
1.0
1.0
1.0
1.0
1.0
0.8
0.6
0.4
0.4
0.6
0.8
1.0

FIGURE 1b

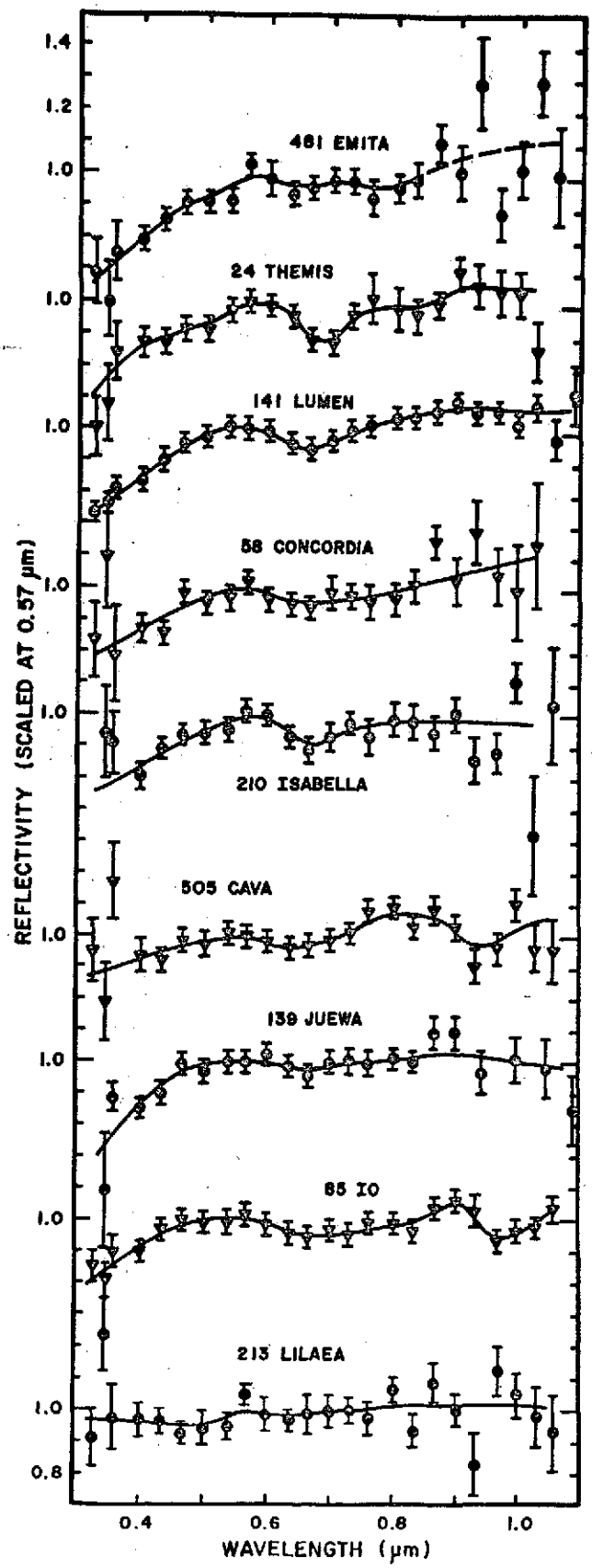
461 EMITA
24 THEMIS
141 LUMEN
58 CONCORDIA
210 ISABELLA
505 CAVA
139 JUEWA
85 IO
213 LILAEA
REFLECTIVITY (SCALED AT 0.57 μm)
WAVELENGTH (μm)
0.4
0.6
0.8
1.0
0.8
1.0
1.2
1.4

FIGURE 1c

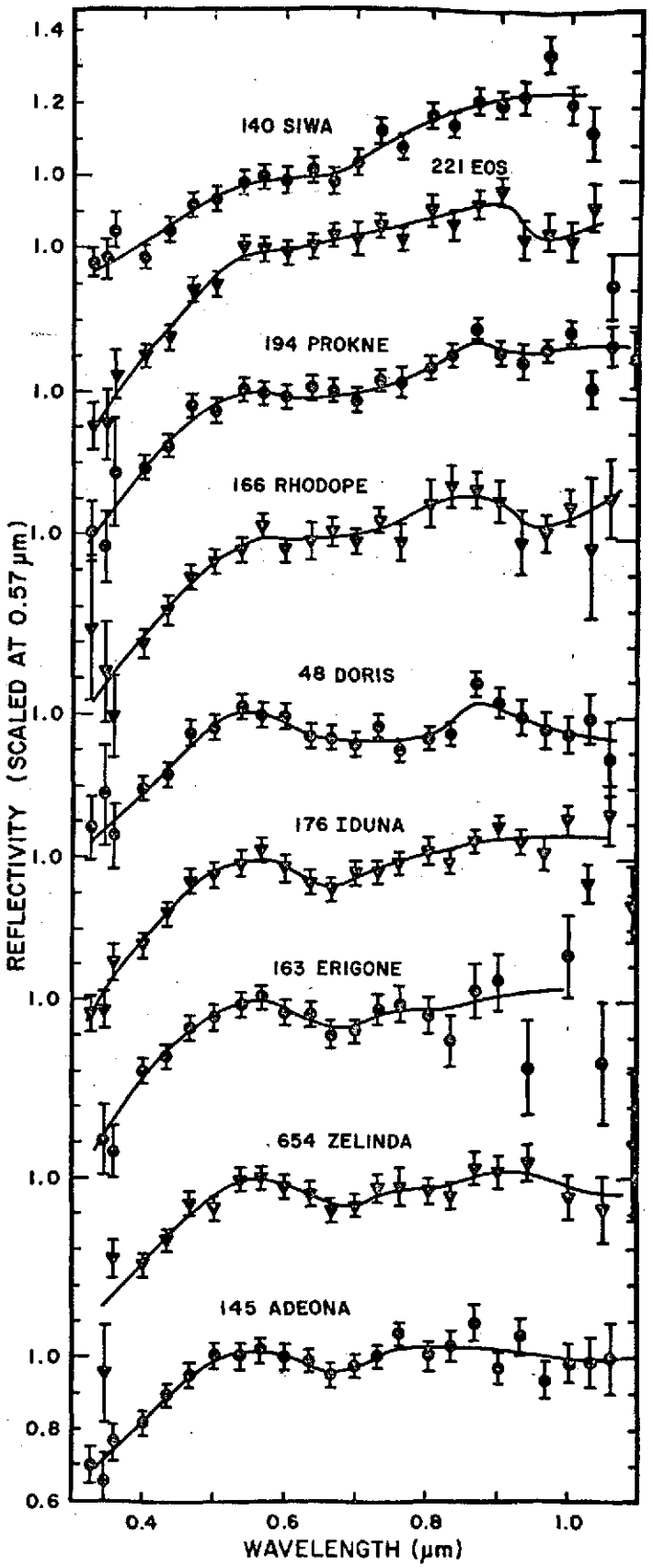
140 SIWA
221 EOS
194 PROKNE
166 RHODOPE
48 DORIS
176 IDUNA
163 ERIGONE
654 ZELINDA
145 ADEONA
REFLECTIVITY (SCALED AT 0.57 μm)
WAVELENGTH (μm)
0.4
0.6
0.8
1.0
0.6
0.8
1.0
1.2
1.4

FIGURE 1d

slight absorption feature near 0.65 μm which exists to some degree in the spectra of nearly all asteroids we have measured. The presence of this feature in the spectra of asteroids of obviously different mineralogy, and its absence in the laboratory spectra of most meteorites and rocks, suggests that it is partly a spurious feature. On the other hand, some asteroids show the feature much more strongly than others, especially those that otherwise resemble C2 meteorites. C2 meteorites usually do show a weak feature (Gaffey, 1974) at that wavelength. Thus the 0.65 μm feature is probably partly real, but the extent to which its presence in the spectra of most asteroids is spurious cannot be reliably judged until a reanalysis of our calibrations, currently underway, is complete.

The spectral reflectance data for the new observations of nine asteroids previously observed are presented in Figure 2. In this figure, the data points and error bars are for the new data only, but the lines are fits to appropriately weighted averages of the new data and the previous data and thus represent the best available reflectance curves for those asteroids.

SPECTRAL CHARACTERISTICS

McCord and Chapman (1975a) defined nine spectral parameters that can be measured from spectral reflectance curves that are compositionally significant or empirically distinguish among asteroid spectra (also see First Quarterly Report on this Contract). We tabulated the four best determined parameters: R/B (reflectance at 0.7 μm divided by that at 0.4 μm); "Bend" (a measure of positive curvature of the visible part of the spectrum); "IR" (an infrared slope parameter sensitive to olivine); and a pyroxene absorption band depth parameter. In Table 1 we tabulate the same parameters for our new sample of asteroids. Asterisks indicate asteroids previously observed; the tabulated values are improved values based on the lines in Figure 2.

All nine parameters can be employed to define apparent groupings of spectral curves in a "nine-dimensional classification space". Such spectral types may indicate distinctive mineralogy or perhaps different mixtures of several fundamental components. Approximately 27 significantly different groups were recognized by McCord and Chapman (1975a), although membership of individual asteroids to the groups was deemed not always significant.

The new asteroid sample has yielded nine new spectral types. Eight of the original groups have been augmented and much improved observations of one previously observed asteroid (14 Irene) has shifted it to a different group. Let me first describe the nine new spectral types, since several of these are of great importance.

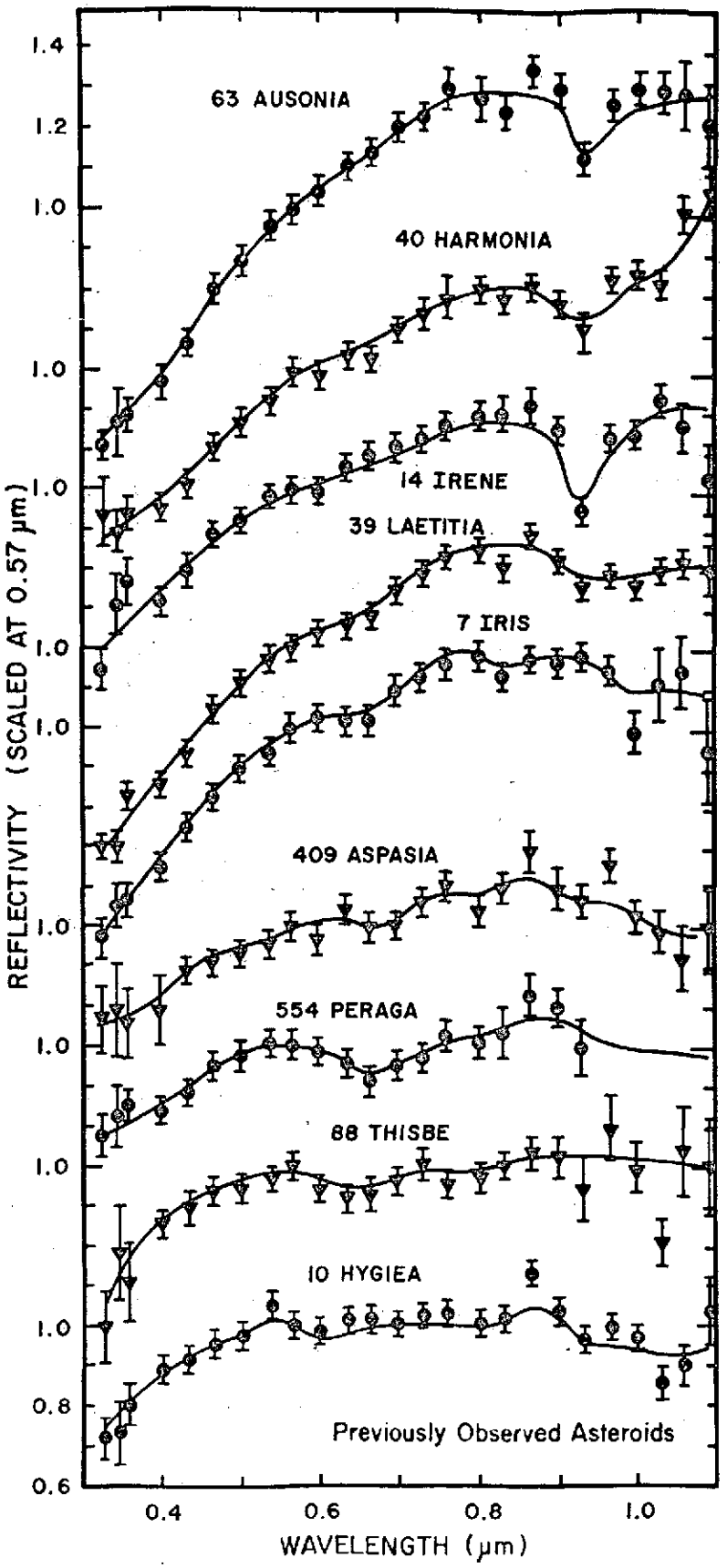
63 AUSONIA
40 HARMONIA
14 IRENE
39 LAETITIA
7 IRIS
409 ASPASIA
554 PERAGA
68 THISBE
10 HYGIEA
Previously Observed Asteroids
REFLECTIVITY (SCALED AT 0.57 μm)
WAVELENGTH (μm)
1.4
1.2
1.0
0.8
0.6
0.4
0.6
0.8
1.0

FIGURE 2

TABLE 1: ASTEROID SPECTRAL REFLECTANCE PARAMETERS

No.	Asteroid	R/B	Bend	IR	IR Band Depth
* 7	Iris	1.639	.170	-.045	~1
* 10	Hygiea	1.143	.120	-.080	?
* 14	Irene	1.470	.133	.093	.83
24	Themis	1.041	.175	(.100)	~1
28	Bellona	1.639	.175	.010	(.877)
* 39	Laetitia	1.742	.160	.010	.933
* 40	Harmonia	1.652	.155	.150	.934
48	Doris	1.200	.295	.015	~1
58	Concordia	1.103	.155	(.145)	~1
* 63	Ausonia	2.069	.180	.045	.892
69	Hesperia	1.309	.13	(.170)	(.791)
80	Sappho	2.036	.270	-.060	~1
85	Io	1.056	.145	.070	.900
* 88	Thisbee	1.135	.135	(.020)	~1
119	Althaea	1.735	.145	.015	~1
139	Juewa	1.152	.150	.000	~1
140	Siwa	1.290	.080	(.140)	~1
141	Lumen	1.155	.165	.080	~1
145	Adeona	1.189	.200	.000	~1
163	Eripone	1.192	.260	(.080)	~1
166	Rhodope	1.443	.265	(.080)	(.929)
170	Maria	1.697	-.010	(.245)	~1
176	Iduna	1.258	.265	(.100)	~1
194	Prokne	1.282	.200	.125	~1
210	Isabella	1.101	.200	-	-
213	Lilaea	1.036	.030	(.010)	~1
221	Eos	1.500	.225	(.045)	.912
349	Dembowska	1.718	.260	-.150	.75
*409	Aspasia	1.245	.105	-.070	~1
446	Aetermitas	2.644	.250	(.07)	(.774)
462	Eriphyla	1.615	.140	(.025)	~1
481	Emita	1.241	.215	(.-35)	~1
505	Cava	1.076	.045	(.045)	.807
*554	Peraga	1.120	.167	(.010)	~1
624	Hektor	1.448	.150	(.305)	?
654	Zelinda	1.225	.289	.010	~1
674	Rachele	1.625	.170	(.070)	~1
714	Ulula	1.629	.215	(.035)	?
887	Alinda	1.631	.265	(.025)	(.954)
911	Agamemnon	1.437	.120	-	-

* Means that these values are improved by incorporating new data with previous data.

Asteroid 349 Dembowska shows a striking spectral reflectance curve, so far unique among the sample of 98 asteroids. It exhibits an infrared absorption band fully as deep as that of Vesta. However the center of the absorption band is at a longer wavelength than that of Vesta and the shape of the curve in the visible is dramatically different. In the important respects, Dembowska's spectral reflectance is identical to that of laboratory measurements of highly metamorphosed ordinary chondrite meteorites (e.g. Gaffey, 1974; Chapman and Salisbury, 1973). The shape and position of the absorption band suggests a high olivine content with a pyroxene/olivine proportion most similar to that of type LL6 chondrites in the Van Schmuss and Wood (1967) classification. L-type chondrites cannot be ruled out but H-types are excluded. One slightly discrepant characteristic of the Dembowska reflection spectrum is the slight dip near 0.65 μm; this may be a stellar calibration artifact, as suggested above. Dembowska is only the second asteroid to be identified as having surface mineralogy similar to that of the most common meteorites, the ordinary chondrites. The other one is 1685 Toro (Chapman et al, 1973b) which most closely resembles type L5 chondrites but has a somewhat lower albedo than is typical for these meteorites. Unlike Toro, which is an Apollo asteroid, Dembowska is located in the outer part of the main asteroid belt near 2.92 A.U.

887 Alinda made a close approach to the earth in early 1974. Although weather conditions kept me from completing the detailed measurements I contemplated making of this object, the data obtained indicate a spectral reflectance curve significantly different from most asteroid spectra in one important respect: the degree to which the spectrum changes from a reddish slope in the UV and blue to a horizontal slope in the red and infrared. This is a common property of laboratory measurements of silicate-rich meteorites but is unusual among asteroids. In all respects, Alinda's spectrum matches that of laboratory spectra of the relatively unquilibrated ordinary chondrites such as Bremervörde (type H3). Unfortunately, the quality of the data is only marginally sufficient to demonstrate the presence of the weak pyroxene absorption feature characteristic of these meteorites and is insufficient to specify the band position which would be necessary to yield a definitive interpretation of the type of pyroxene and proportion of olivine present on the asteroid surface.

80 Sappho is a fairly small asteroid located near the inner edge of the main asteroid belt. Its spectrum is similar to Alinda's in many respects and I place it in the same spectral grouping. However it is slightly redder than Alinda, shows no evidence of an absorption feature, and it probably has a lower albedo than Alinda (Matson, 1971, compared with Zellner et al, 1974, and Morrison, 1974). One meteorite measured by Hunt and Salisbury (1970) is a reasonable match to Sappho; it is Lancé, a type C3O. But it is a somewhat atypical sample of such meteorites and Sappho's spectrum must be

regarded as undiagnostic, although resembling some relatively metamorphosed carbonaceous chondrites.

Asteroid 446 Aetermitas shows by far the reddest spectrum yet measured for an asteroid. A deep but unusually narrow absorption feature centered near 0.97 μm is indicated. An equally unusual asteroidal spectrum is that of 170 Maria. It is rather steeply sloping and reddish, virtually identical to spectral reflectances of many lunar maria soils. The spectrum is distinctive among asteroids but is not diagnostic of composition.

Asteroid 69 Hesperia shows some spectral characteristics similar to those of some achondrite meteorites. Unfortunately the data are inadequate to define these characteristics precisely; further observations are warranted. Asteroids 166, 194, and 221 resemble each other but not any previously observed asteroids. Asteroid 48 seems to represent still another new type. Asteroid 213 has a virtually horizontal reflection spectrum throughout the 0.32 to 1.06 μm range and is therefore also a new type.

Improved observations of 14 Irene show a moderately deep but narrow infrared absorption feature, and an overall spectrum similar to spectral characteristics for 89 Julia. Therefore I assign it to the same spectral group as Julia and move the one other asteroid with which it had been grouped (79 Eurynome) into the Juno-group. One new asteroid also has a spectrum similar to that of Juno: 28 Bellona.

Other groups previously defined that have been augmented by the new asteroid sample are: the group of 12 Victoria (119); the group of 9 Metis (462, 674, and 714); the group of 51 Nemausa (145, 163, 176, and 654); the group of 324 Bamberga (141, 58, 210, 481, 24, and 505); the group of 10 Hygiea (85); and the group of 511 Davida (139 Juewa).

A particularly striking characteristic of the new sample is that such a large percentage of the new asteroids fall into the Nemausa and Bamberga groups. These asteroids have spectral characteristics that have been previously likened to laboratory measurements of primitive carbonaceous chondrites (type C2). In all cases where radiometric or polarimetric observations have yielded albedos, these asteroids are found to be dark or extremely dark (Chapman et al, 1975). As we extend the spectral reconnaissance survey to fainter magnitudes, it seems clear that asteroids of this type will eventually predominate since they are biased against in samples of bright asteroids. They are already more numerous than the Juno-type asteroids which were most common in our initial sample (Chapman et al, 1973a).

The histogram of R/B values for our entire sample of 98 asteroid (Figure 3) continues to show the bimodal pattern McCord and Chapman (1975a) had previously noted, which is also apparent in other photometric parameters, such as albedo (Chapman et al, 1975) and minimum polarization(Zellner et al, 1974). But the low R/B group, composed predominantly of members of the Nemausa and Bamberga spectral types, is now beginning to exceed the reddish group.

The question of how many additional spectral types may exist in the asteroid belt can be examined from our sampling statistics. McCord and Chapman (1975a) previously noted that fainter main belt asteroids were predominantly falling into spectral types already recognized and that most new spectral types were arising from the dwindling number of unobserved bright asteroids. The new sample presented in this Final Report shows the same overall trend, but not as strongly as before. In addition to the non-belt asteroids which McCord and Chapman anticipated might be spectrally different (and were: the Trojans and 887 Alinda), several of the new spectral types are due to 13th magnitude objects (170 Maria, 446 Aetermitas, and 213 Lilaea). Thus the total number of spectral types in the asteroid belt probably exceeds the earlier estimate of 40 to 50, but it is definitely limited.

CORRELATION OF SPECTRAL PARAMETERS WITH ORBITAL ELEMENTS

I now comment briefly on correlations of spectral parameters with various orbital parameters in order to augment similar discussions in previous data papers (Chapman et al, 1973a; McCord and Chapman, 1975a). More comprehensive considerations of these correlations are given by Chapman et al (1975) and by Hartmann et al (1975).

Reliable approximate colors (R = red, M - medium, F = flat spectrum) can be derived for 147 asteroids using the R/B parameter for the 98 observed asteroids and other colorimetry as given in Table IX of Chapman et al, 1973a, and augmented by the UVB photometry of Dunlap (1974) and Howes and Gehrels (1974). Figure 4 shows spectral parameters for 147 asteroids plotted versus semi-major axis and proper eccentricity (as kindly provided by Williams). Asteroids having aphelia (maximum orbital distances) beyond 3.45 A.U. are almost never reddish in color and many resemble carbonaceous chondrites, which are the meteorites believed to have accreted in the coolest environment. But there are many exceptions to the gross correlation of color with semi-major axis: while one of two asteroids with spectra resembling the most common meteorites (ordinary chondrites) has a very small semi-major axis (1685 Toro) in agreement with the model of Lewis (1974), the other one, 349 Dembowska, orbits in the outer part of the belt. Condensation/accretion sequences during early solar system history might plausibly have varied with solar distance or distance above the central plane of the nebular disk. They may be reflected

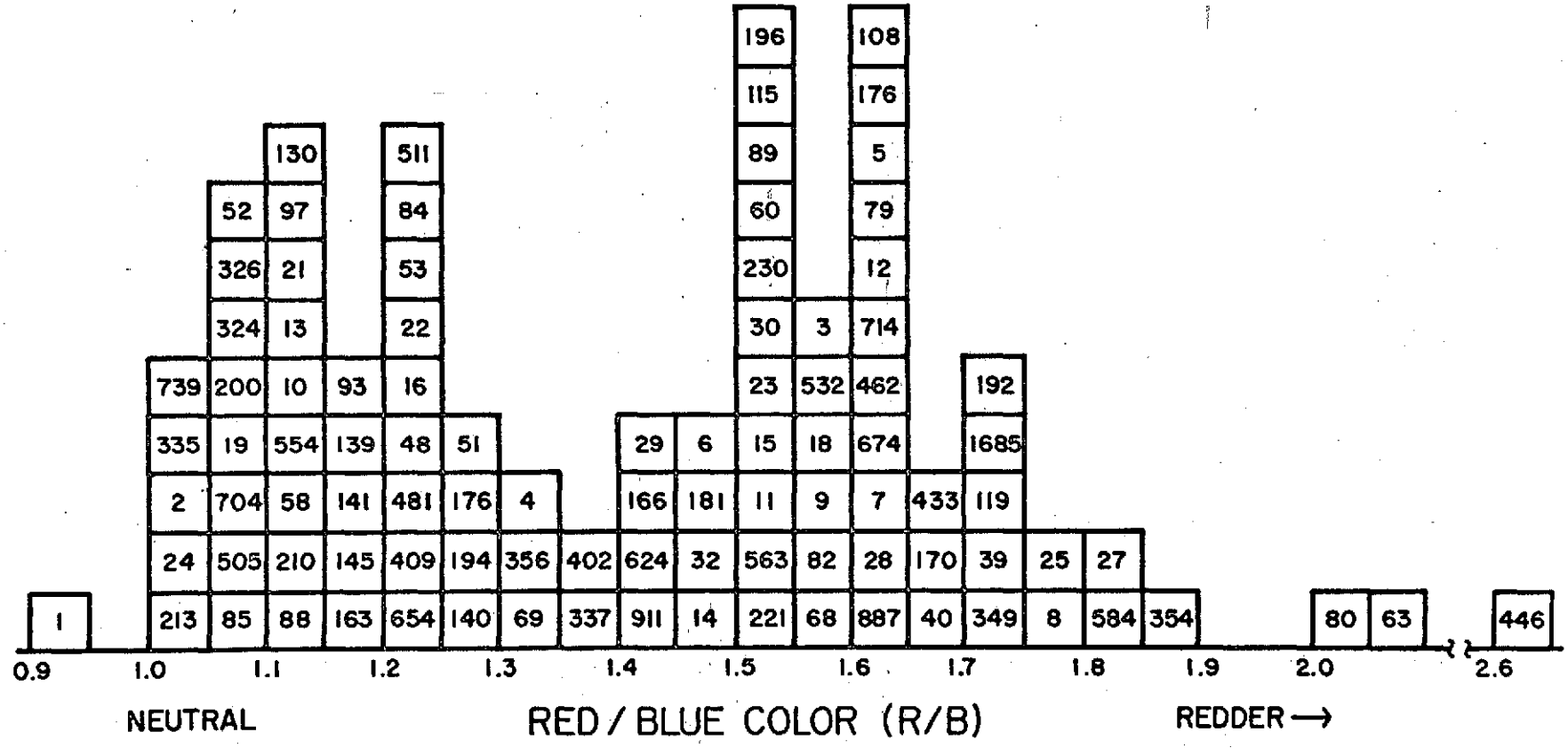
0.9
1.0
1.1
1.2
1.3
1.4
1.5
1.6
1.7
1.8
1.9
2.0
2.6
NEUTRAL
RED / BLUE COLOR (R/B)
REDDER →

FIGURE 3

CAPTION TO FIGURE 4

Spectral parameters are plotted as a function of semi-major axis and proper eccentricity for 147 asteroids. Symbols in black are the 98 asteroids measured by Chapman and McCord; those in dotted lines are objects for which overall colors are known, but no other spectral information. Asteroid diameter is indicated by three sizes of symbols (largest for diameters over 200 km; smallest for diameters under 100 km). Approximate colors are given by symbol shape: triangles for reddish objects with R/B color indices of 1.5 or greater; squares for intermediate colors; circles for nearly neutral colors (R/B less than 1.25). The presence of the 0.95 μm pyroxene absorption band is indicated by filled symbols; half-filled symbols are for weaker bands. The IR spectral parameter indicative of olivine is shown by vertical lines; two vertical lines suggests considerable olivine (no infrared data exists for asteroids indicated by dots under the symbols). Another spectral parameter ("bend") indicated by horizontal lines, indicates the degree to which asteroid spectra curve or bend in the visible; the greatest bending is indicated by two horizontal lines.

Evidently there is considerable diversity of all spectral parameters both as a function of the orbital parameters and as a function of family membership. But few objects with aphelia exceeding 3.45 A.U. are red and other vague correlations may be present. Asteroids bordering Kirkwood gaps (certain semi-major axes, indicated by arrows, where few asteroids exist due to Jupiter perturbations) seem to be predominantly reddish in color, although it is not known why this is true. Nine asteroids plot off scale; those to the lower right approach closely to the earth and the three to the upper left are Trojans.

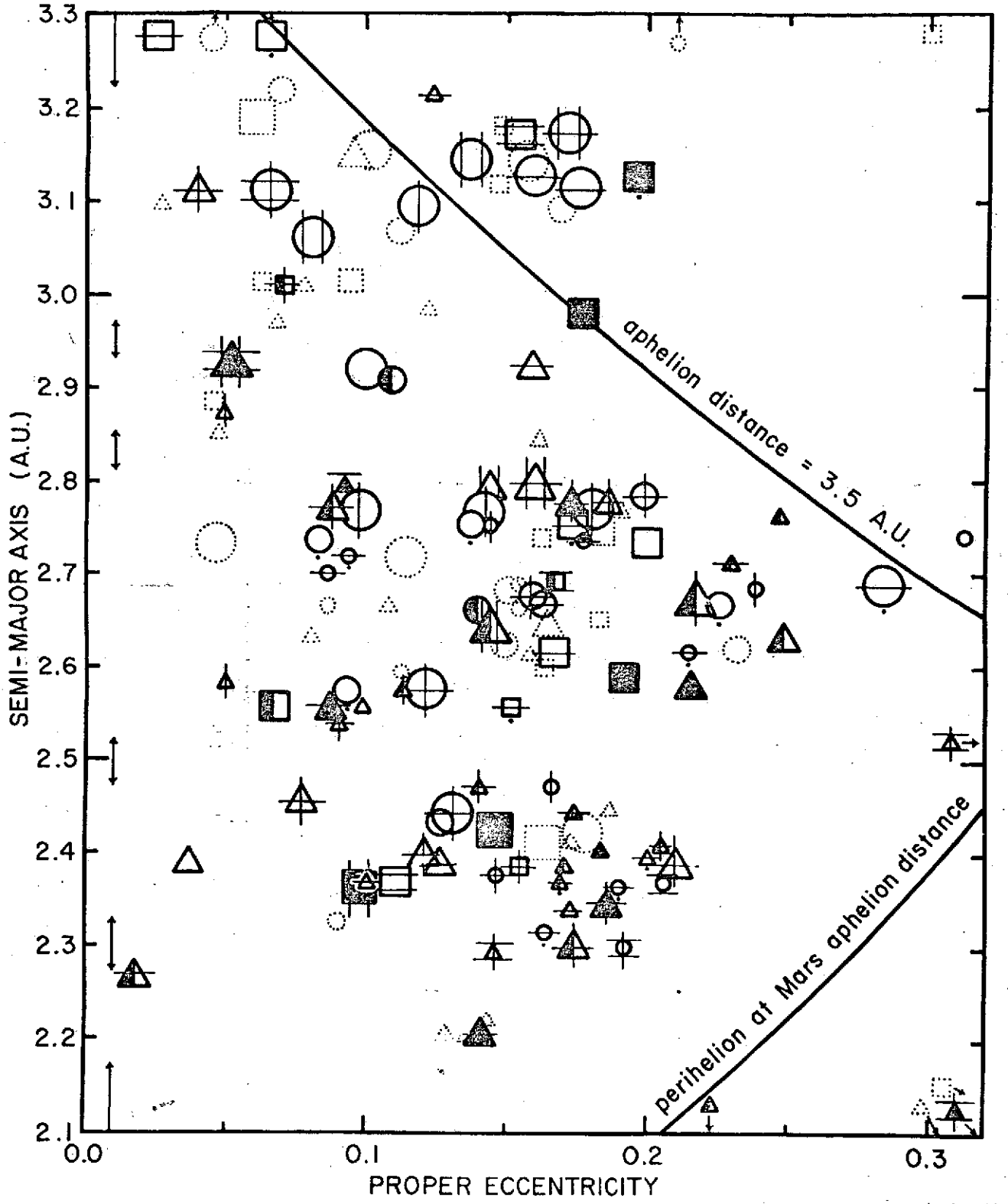
3.3
3.2
3.1
3.0
2.9
2.8
2.7
2.6
2.5
2.4
2.3
2.2
2.1
SEMI-MAJOR AXIS (A.U.)
0.0
0.1
0.2
0.3
PROPER ECCENTRICITY
aphelion distance = 3.5 A.U.
perihelion at Mars aphelion distance

FIGURE 4

today in variations of asteroid spectral properties with orbital distance. But presumably gravitational forces "stirred the pot" subsequent to accretion. On the otherhand the early radial distributions may be preserved better than it seems if we are being confused by fragments of geochemically differentiated parent bodies. Some asteroids might show their original surfaces while others might be core or mantle fragments with different spectra. As shown in Figure 5, reddish asteroids predominate inside of 2.3 A.U. and are very rare beyond 3.0 A.U. Flat spectra tend to be common in the outer half of the asteroid belt. This is an important relationship since flat spectra are dominantly due to low-albedo carbonaceous material believed to condense in cooler parts of the solar nebula. However the color/semi-major axis relationship is seriously affected by sampling biases in the following manner: because of the low albedos generally associated with F and M colors, the small F and M type asteroids are discriminated against and even moderate-sized F and M objects are missed at large semi-major axes. Examination of the color vs a distribution for the largest 28 asteroids (diameters calculated, or inferred through the color/albedo correlation by Chapman et al, 1975) suggests that only 5% to 20% of asteroids beyond 2.7 A.U. are R, while perhaps 30% to 50% of those within 2.5 A.U. are R (see Figs. 6 and 7). Thus the dominant surface compositions of asteroids are carbonaceous, especially in the outer half of the belt.

I have examined our sample of 98 asteroids for semi-major axis variations of some other spectral parameters. A trend related to the color correlation shown in Figs. 5-7 suggests that many asteroids ($\sim$ 70%) with $a < 2.3$ A.U. have infrared absorption bands, whereas few asteroids ($\sim$ 10%) beyond 3.0 A.U. have bands (see Fig. 8).

There is a significant tendency for the "bend" parameter to average lower for $a < 2.5$ A.U. (Fig. 9). McCord and Gaffey (1974) argue that "bend" increases with increasing proportions of silicates: thus asteroids at small semi-major axes have lower proportions of opaques (metals in the case of R asteroids as in Fig. 10, carbon in the case of non-R asteroids).

The "IR" parameter, low or negative values of which tend to indicate olivine, shows little variation with a among the 83 asteroids for which the parameter has been measured (Fig. 11).

COMPOSITIONAL IMPLICATIONS: RELATIONSHIPS TO METEORITES

During the past five years, several new kinds of astronomical observations of asteroids have provided data of potentially great importance to the understanding of the relationship between meteorites and asteroids. The spectral curves discussed in previous sections of this final report have been augmented by absolute reflectivity (or albedo) measurements of asteroids by the radiometric technique (Allen, 1971; Cruikshank and Morrison, 1973; Morrison, 1974) and the polarimetric technique (Veverka and Noland, 1973; Bowell and Zellner, 1974; and Zellner et al, 1974).

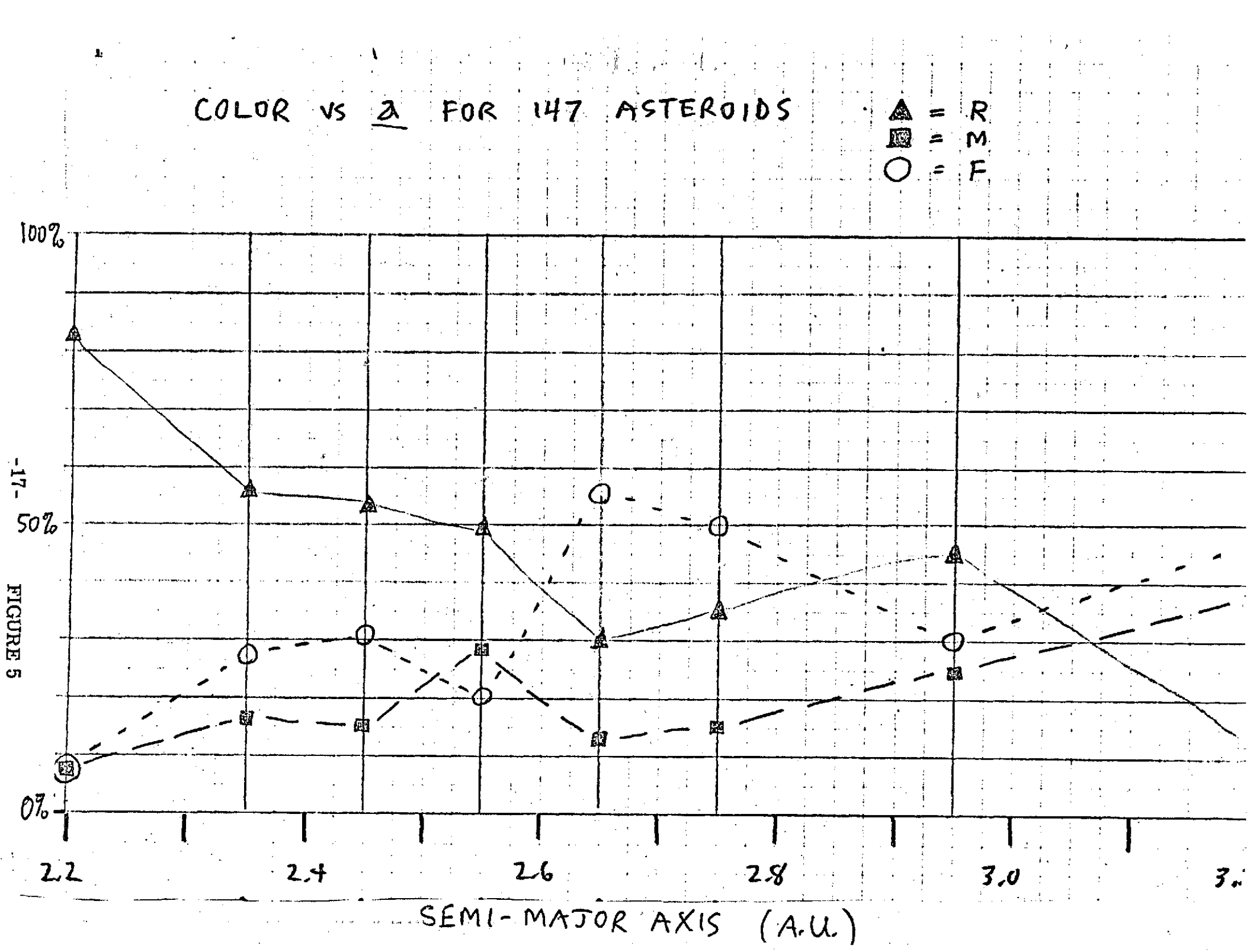
COLOR VS a FOR 147 ASTEROIDS
▲ = R
▣ = M
○ = F
100%
50%
0%
2.2
2.4
2.6
2.8
3.0
SEMI-MAJOR AXIS (A.U.)

FIGURE 5

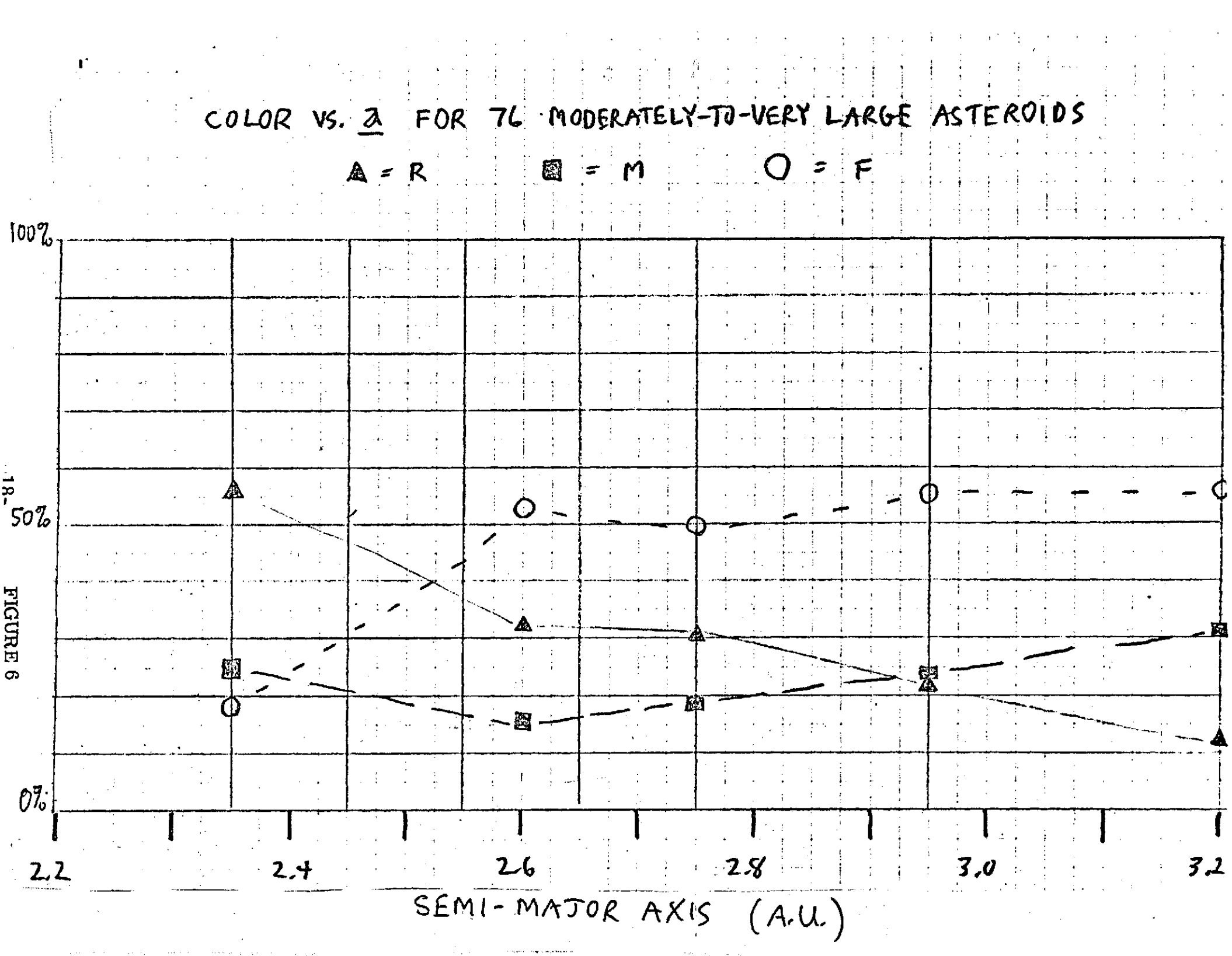
COLOR VS. a FOR 76 MODERATELY-TO-VERY LARGE ASTEROIDS
▲ = R
■ = M
○ = F
100%
50%
0%
2.2
2.4
2.6
2.8
3.0
3.2
SEMI-MAJOR AXIS (A.U.)

FIGURE 6

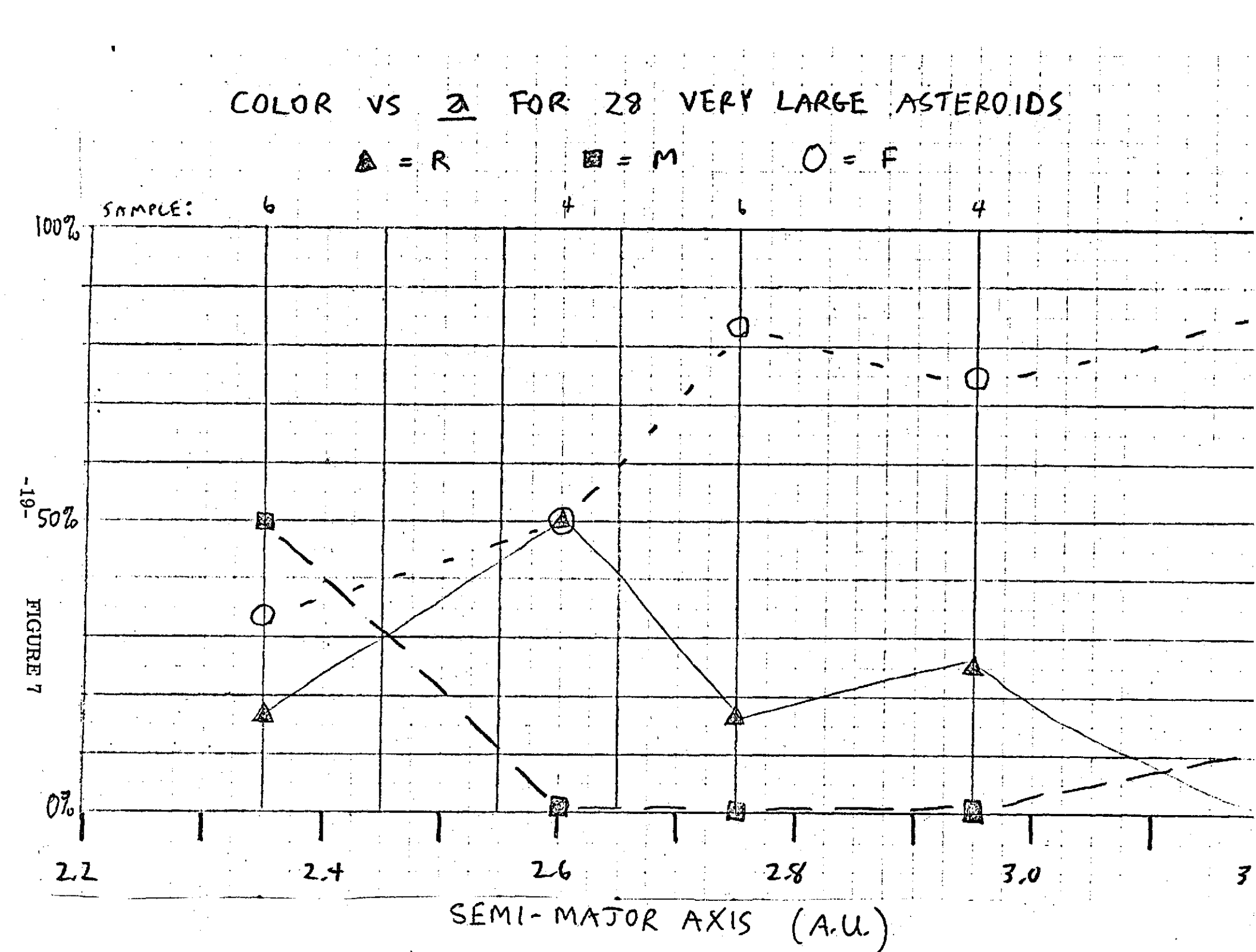
COLOR VS a FOR 28 VERY LARGE ASTEROIDS
▲ = R
■ = M
○ = F
SAMPLE:
6
4
6
4
100%
50%
0%
2.2
2.4
2.6
2.8
3.0
3
SEMI-MAJOR AXIS (A.U.)

FIGURE 7

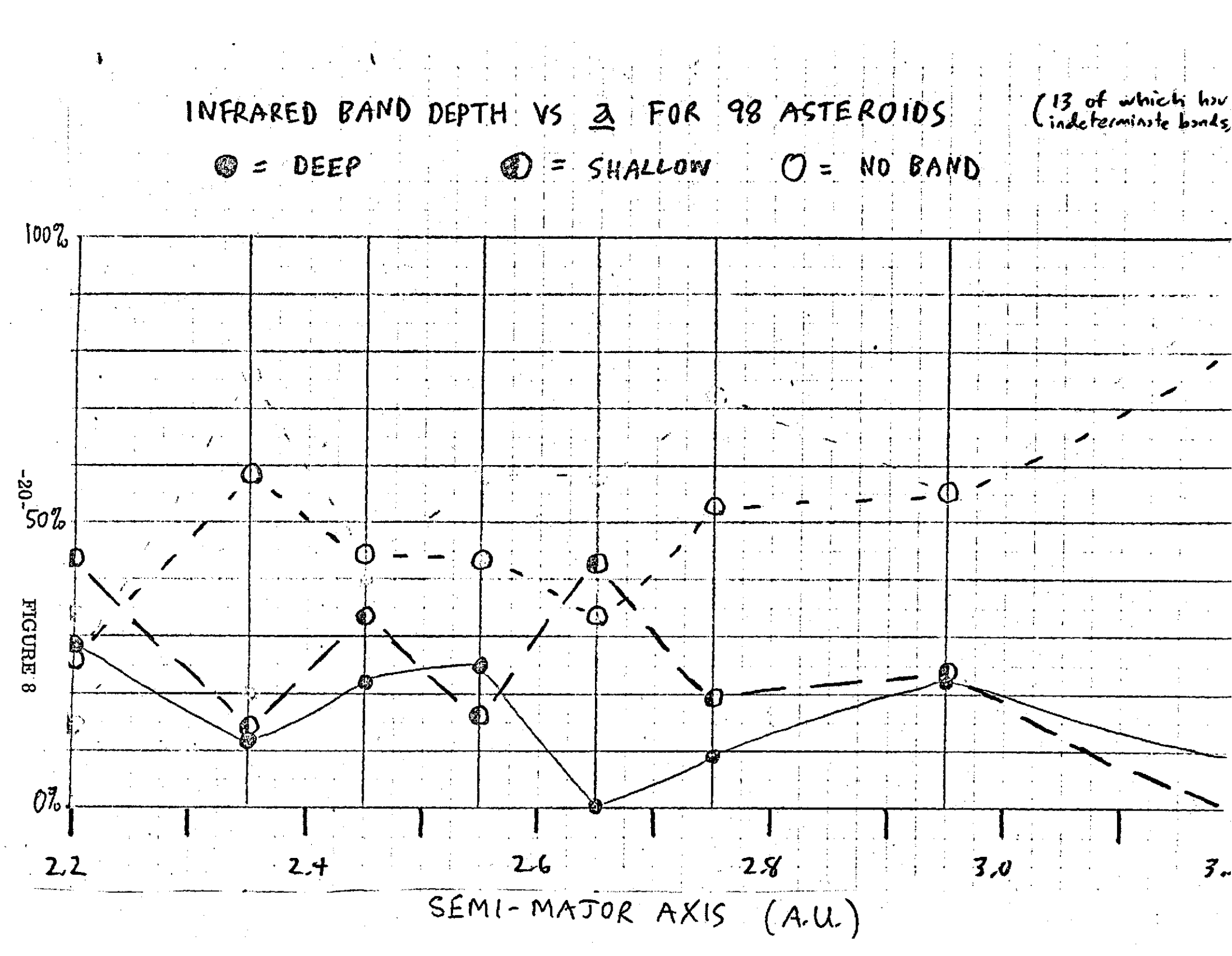
INFRARED BAND DEPTH VS a FOR 98 ASTEROIDS
(13 of which hav
indeterminate bands
● = DEEP
◐ = SHALLOW
○ = NO BAND
100%
50%
0%
2.2
2.4
2.6
2.8
3.0
SEMI-MAJOR AXIS (A.U.)

FIGURE 8

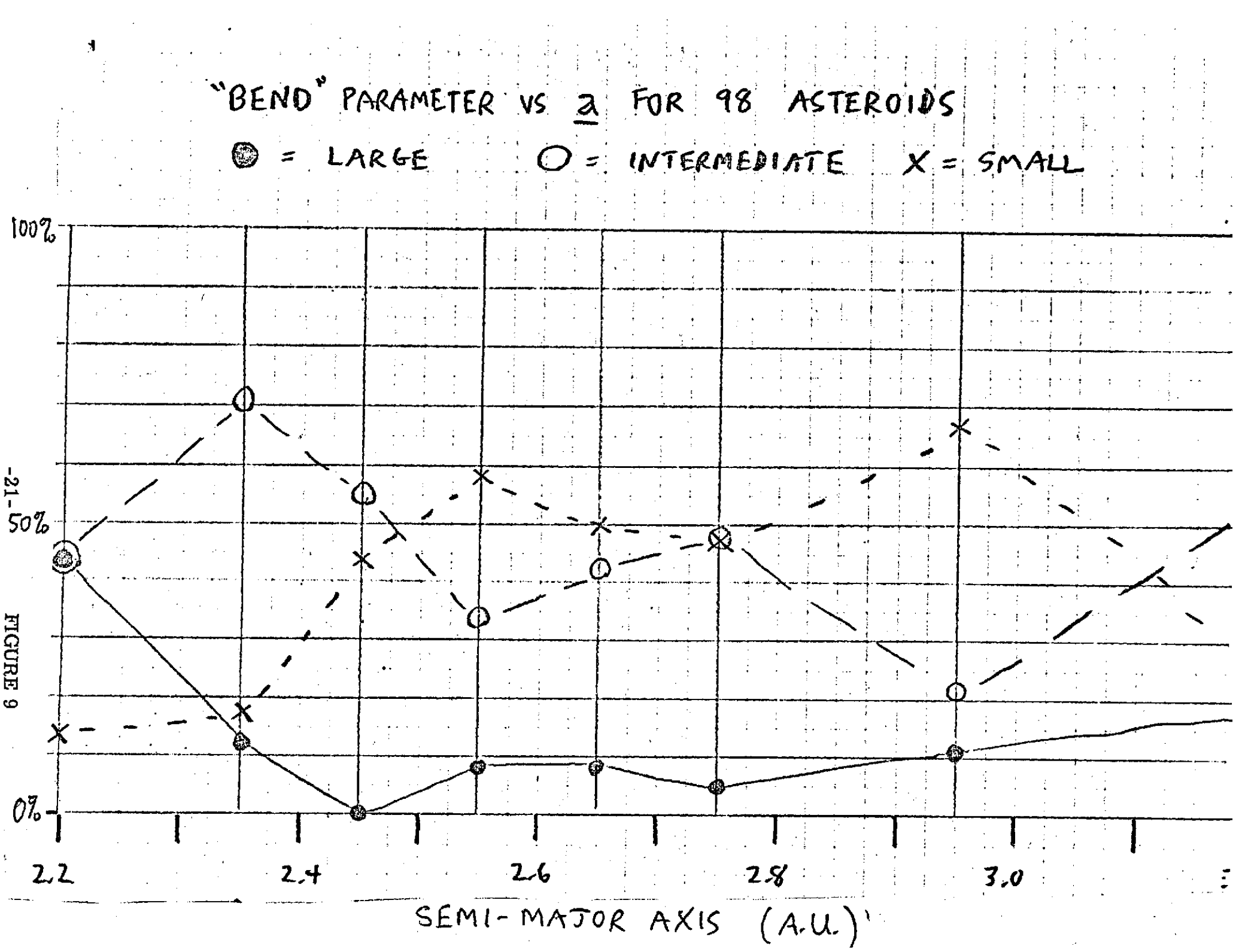
"BEND" PARAMETER VS a FOR 98 ASTEROIDS
● = LARGE
○ = INTERMEDIATE
X = SMALL
100%
50%
0%
2.2
2.4
2.6
2.8
3.0
SEMI-MAJOR AXIS (A.U.)

FIGURE 9

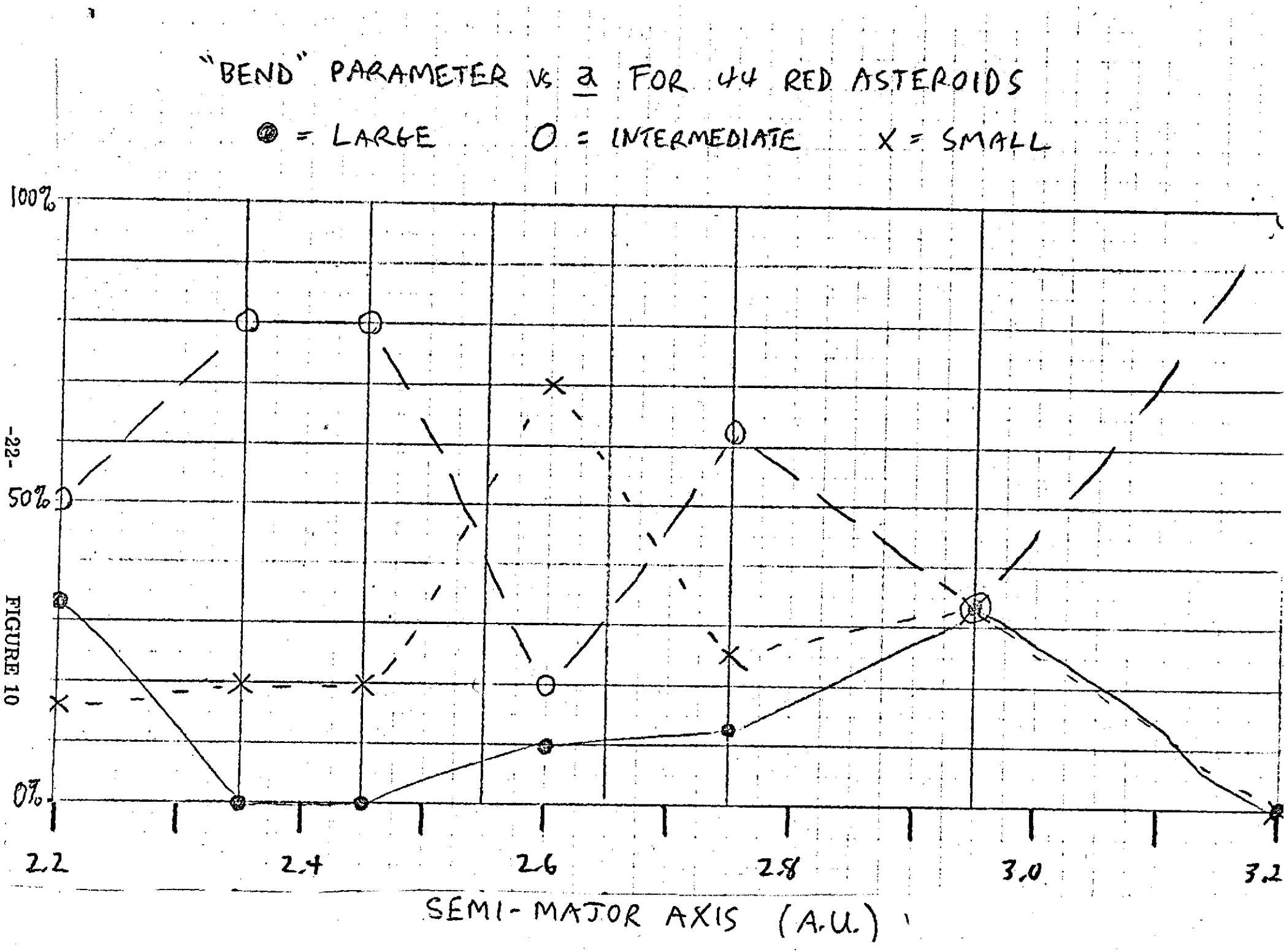
"BEND" PARAMETER vs a FOR 44 RED ASTEROIDS
◉ = LARGE
O = INTERMEDIATE
X = SMALL
100%
50%
0%
2.2
2.4
2.6
2.8
3.0
3.2
SEMI-MAJOR AXIS (A.U.)

FIGURE 10

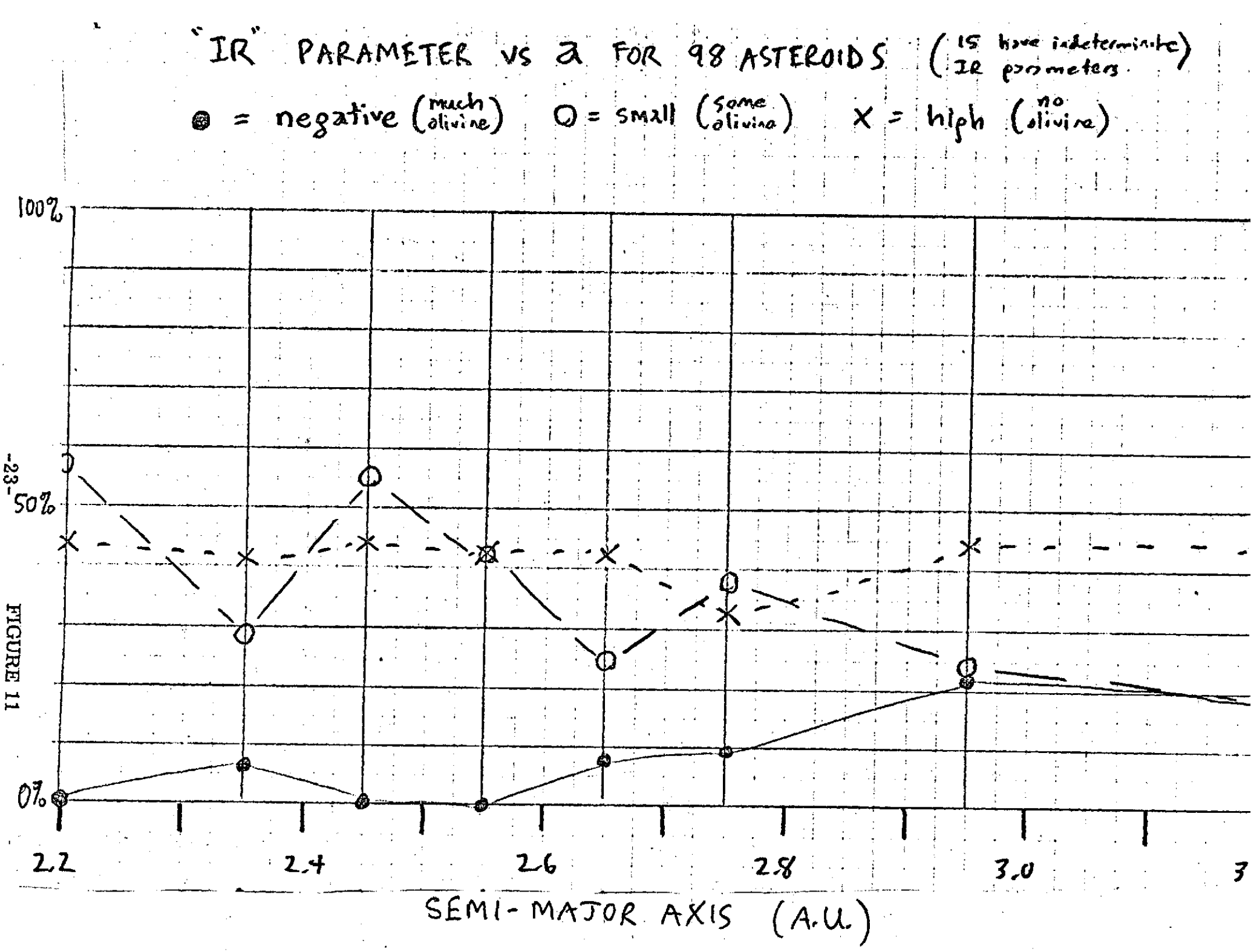
"IR" PARAMETER vs a FOR 98 ASTEROIDS (15 have indeterminate IR parameters.
● = negative (much olivine) O = small (some olivine) X = high (no olivine)
100%
50%
0%
2.2
2.4
2.6
2.8
3.0
3
SEMI-MAJOR AXIS (A.U.)

FIGURE 11

Spectral absorption features in asteroid spectra may be interpreted using crystal-field theory and identified with particular electronic transitions within crystal lattices of particular minerals. Asteroid spectra also may be interpreted by comparison with a library of laboratory measurements of the spectral reflectances of various mineral assemblages, including meteorites. Some initial attempts to interpret the compositions of asteroid surface mineralogy and to relate it to meteorites were done by Chapman and Salisbury (1973); Johnson and Fanale (1973); Egan et al (1973); McCord and Gaffey (1974); Gaffey (1974); and Gaffey and McCord (1975).

The results published in the literature cited above have established that most asteroid surfaces are dominantly composed of mineral assemblages similar to those of many classes of meteorites (most commonly carbonaceous chondrites). It is also clear that potential asteroidal parent-bodies for many meteorite classes are rare, and in any case not yet found. Without delving into the caveats that must accompany any serious attempt to interpret mineralogy using these remote-sending techniques (they are dealt with in articles cited above), I will adopt the working hypothesis that close similarity between certain compositionally important spectral reflectance parameters of the asteroid data and laboratory measurements of meteorites implies mineralogical similarity.

From this basis, I intend in this section to elaborate on possible implications for meteorite parent bodies that emerge from these and other related astronomical studies of asteroids. I demonstrate that there is a strong case for the meteorites indeed being asteroidal fragments, as has been argued since the time of Olbers but in the last decade has been seriously disputed (Opik, 1964; Wetherill, 1971).

COMPARISONS OF METEORITE AND ASTEROID SPECTRA

A fairly comprehensive library of laboratory spectral albedo curves for meteorites now exists. The first, but smaller, study was that of Salisbury and Hunt (1974) which was presented in a more relevant context by Chapman and Salisbury (1973): Several dozen meteorite powders were measured with greatest emphasis on the variety of ordinary chondrites. Johnson and Fanale (1973) measured about a dozen carbonaceous chondrites. The most comprehensive laboratory measurement program by far is that of Gaffey (see Gaffey, 1974; McCord and Gaffey, 1974; Gaffey and McCord, 1975). In that program all major classes of meteorites were represented (usually with several individual examples), including each of the chondrite classifications of Van Schmuss and Wood (1967). Several other researchers have measured a few meteorites, but the three studies just described, especially that of Gaffey, forms the foundation of meteorite laboratory comparisons. Only the irons and stony-irons have been relatively neglected because of problems of sample preparation, but it is relatively easy to model the likely reflectance spectra of such metal-silicate mixtures. The laboratory measurements are deemed to be highly reliable, although terrestrial

weathering of some meteorites is noticeable in the spectra. The particle-size distribution in the prepared meteorite powders can appreciably affect the absolute reflectivity (albedo) but the spectral properties are not greatly altered, so comparisons with asteroid surfaces which are probably at least partly dusty or particulated are reasonable.

Fig. 12 shows comparisons of spectral reflectance data for 9 asteroids and spectral reflectance curves of some similar meteorites. Albedos are not known for all of the asteroids, but in cases where they are known they agree approximately with the albedos of the meteorites with which they are compared. It can be seen that the matches are reasonably good in all cases, generally within the errors of the astronomical observations. In most cases, the spectral characteristics are dominated by one or a very few optically-important minerals, generally pyroxenes for the brighter spectra and opaques (carbon) for the darker spectra. With respect to such optically-important minerals (which are not necessarily the dominant minerals in terms of weight since some, such as plagioclase, exert a minor affect on spectra unless present in overwhelming quantities -- Nash and Conel(1974)), the similarity of the meteorite and asteroid spectra shown in Fig. 12 bespeak similar compositions.

It is not my intention to treat the mineralogical interpretation of asteroid spectra in detail in this report, since that is being covered by other authors (e.g. Gaffey and McCord, 1975). But I will give a brief overview of the probable mineralogy of asteroids derived on the general assumption that if an asteroid spectrum resembles the laboratory spectrum of a meteorite, its surface is probably like that meteorite. This approach is a fruitful one, as will be seen, but it ignores the strict question of uniqueness. It can also be misleading if carelessly interpreted. For instance, as previously discussed, 349 Dembowska can be reliably interpreted as having roughly the same mix of orthopyroxenes, olivine, and opaques as LL (or maybe L) chondrites of petrologic type 6 (or maybe 5). Very plausibly its surface is indeed composed of LL6 chondrites. On the otherhand, a rock composed of the same minerals but completely lacking in chondrules would be spectrally indistinguishable from an LL6 chondrite, and obviously the reflection spectrum says nothing about trace elements and other characteristics which may be important in the classification of a meteorite.

Spectral albedo curves may be plotted for those asteroids with known geometric albedos and compared with laboratory measurements of meteorites. Asteroid spectra span roughly the same range of albedos (from very dark to moderate) that pertain to meteorites. However the distribution of asteroid spectra is decidedly non-representative of meteorites in a numerical sense. Thus the most common meteorites -- the ordinary chondrites -- are represented by at most two of the 98 asteroids so far observed. Nevertheless most asteroids have plausible, or at least possible, meteorite analogs.

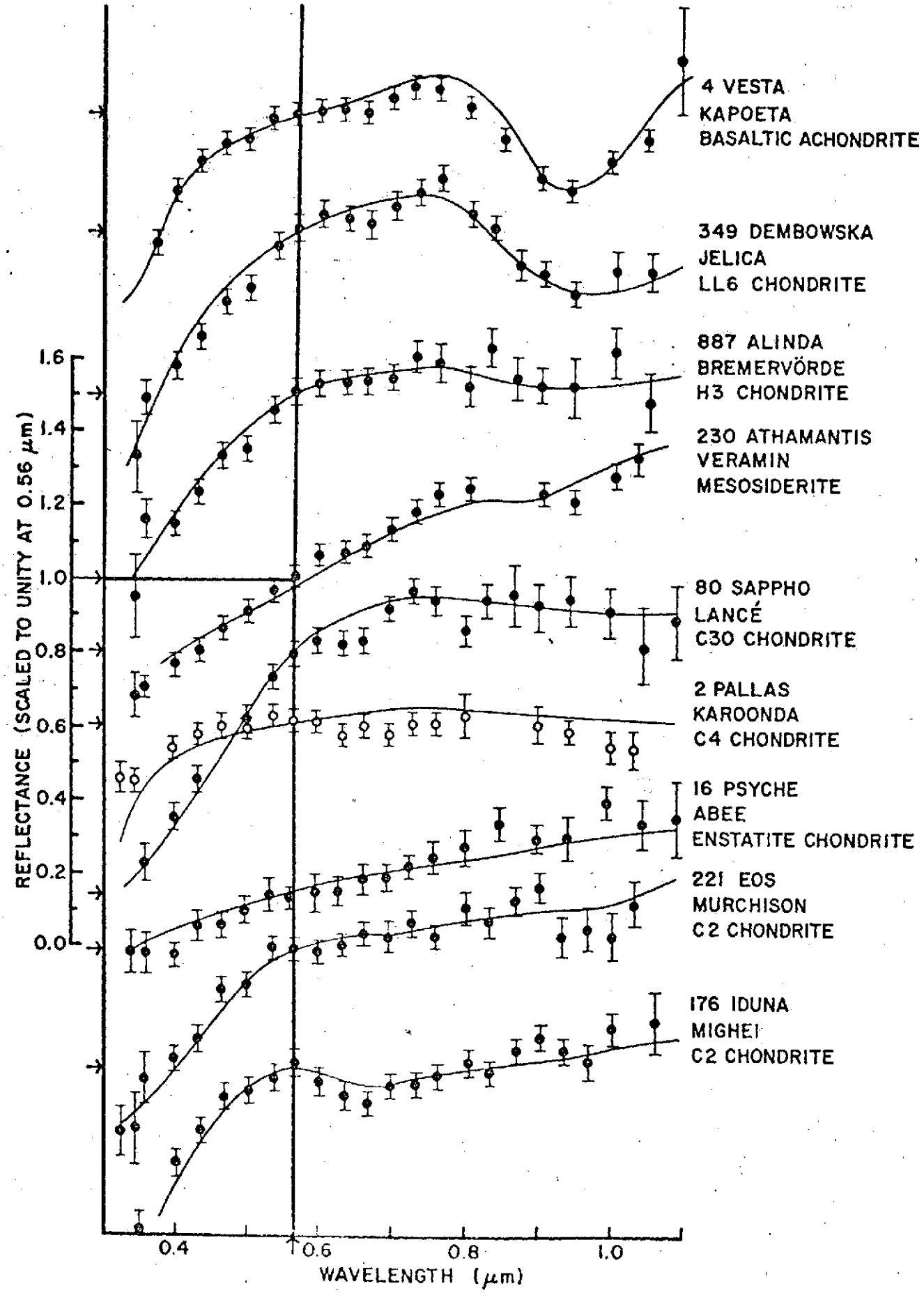
4 VESTA
KAPOETA
BASALTIC ACHONDRITE
349 DEMBOWSKA
JELICA
LL6 CHONDRITE
887 ALINDA
BREMERVÖRDE
H3 CHONDRITE
230 ATHAMANTIS
VERAMIN
MESOSIDERITE
80 SAPPHO
LANCÉ
C30 CHONDRITE
2 PALLAS
KAROONDA
C4 CHONDRITE
16 PSYCHE
ABEE
ENSTATITE CHONDRITE
221 EOS
MURCHISON
C2 CHONDRITE
176 IDUNA
MIGHEI
C2 CHONDRITE
REFLECTANCE (SCALED TO UNITY AT 0.56 μm)
1.6
1.4
1.2
1.0
0.8
0.6
0.4
0.2
0.0
0.4
0.6
0.8
1.0
WAVELENGTH (μm)

FIGURE 12

Vesta, the brightest asteroid, has a unique spectrum almost certainly diagnostic of a basaltic achondritic composition with dominant pigeonite pyroxene (though once again, as a final caution, if Vesta's surface material were formed of round "chondrules" of this mineralogy, we would never know it). This important compositional inference (first made by McCord et al 1970) stands regardless of more detailed compositional inferences that can be made from detailed consideration of Vesta's spectrum that might distinguish between eucrites and howardites, for instance (see Chapman, 1971; Gaffey, 1974; Larson and Fink, 1975; Johnson and Matson, 1975).

The darkest asteroids are almost certainly of carbonaceous composition, and most closely resemble laboratory measurements of C2 meteorites (there are inadequate data on C1's because of the paucity of samples).

The reddish asteroids are common among the brighter asteroids. Most of them show relatively weak infrared absorption features, mostly due to pyroxenes, but some due to olivine, and some perhaps due to calcic pyroxenes or mixtures of pyroxenes and olivines. Unfortunately, it is not yet possible to infer the precise mineralogy of the silicates causing these features because the bands are so weak. However, this will be possible in the future when the stellar calibrations for the asteroid photometry are improved and better infrared data are obtained. The overall reddish color of these asteroids cannot be ascribed to most plausible minerals and is certainly not represented among measured stony meteorites. However Gaffey has argued persuasively that an admixture of nickel-iron, in abundances exceeding those found in ordinary chondrites, would yield spectra of this type. Very possibly these asteroid surfaces resemble pallasites, mesosiderites, or other plausible stony-iron compositions.

Approximately two asteroids have straight, gently-sloping, reddish spectra (albedo about 10%) which is not a diagnostic spectrum but does match laboratory spectra of enstatite chondrites, especially those containing abundant metal. An alternative interpretation is that these asteroids are of pure iron; although such an interpretation cannot be ruled out until we have better understanding of the probable physical state of an iron asteroid surface subject to space bombardment, it appears that the albedos of these asteroids (e.g. 16 Psyche) are more like those of enstatite chondrites than irons.

There are several other asteroidal spectral types, including some asteroids resembling C3 meteorites, one resembling an ordinary chondrite of low petrological type, and a few of unexciting but as-yet-unidentified composition.

The last remaining spectral type to be described is represented by 4 asteroids (1 Ceres, 2 Pallas, 10 Hygiea, and 511 Davida). These spectra have fall-offs in the ultraviolet, but have nearly neutral colors in the visible, and spectra which extend horizontally well into the ultraviolet. The albedos are

quite low (5% to 8%), but not as low as those for asteroids exhibiting the C2-type spectra. As shown on Fig. 11, one of these asteroids approximately matches laboratory spectra for the unusual C4 meteorite Karoonda. An alternative interpretation for these spectra is the suggestion of Johnson and Fanale (1973) and Matson et al (1974) of a carbonaceous chondrite composition (perhaps C1 or even more primitive). No good meteorite match has actually been found, however, and some laboratory spectra of certain ultrabasic terrestrial basalts (Ross et al, 1969) also resemble these asteroids.

A clue to the composition may be the fact that these four asteroids plus Vesta are almost certainly the largest five asteroids in the belt. If the largest asteroids were heated the most and geochemically differentiated, then the suggestion that these spectra are of basalt is plausible, though the basalt must differ greatly from that which is on Vesta. But there is a fatal objection to this interpretation: Mass measurements of Ceres (Schubart, 1974) combined with diameter measurements by the radiometric and polarimetric techniques yield a density for Ceres of about 2 gm cm^{-3} (and almost certainly no higher than 2 1/2). The density for Pallas is higher than for Ceres, but is probably (though not certainly) less than the value of 3.6 + 0.6 which has been measured for Vesta (mass from Hertz, 19). Ceres can hardly have a bulk density of C1 chondrites and yet be covered with a surface layer of basalts. Thus it is most plausible that Ceres and the other three asteroids have carbonaceous surfaces. Whether they are spectrally different from smaller carbonaceous asteroids because of regolith processes on these large objects or because of conversion to C4-type material perhaps by minor heating, or because they somehow were initially formed with a slightly different kind of carbonaceous material (perhaps C1 or ultraprimitive) cannot now be decided.

METEORITE PARENT-BODIES AND EVOLUTION OF THE ASTEROIDS

Vesta presents an interesting example of the relationship between asteroid spectrophotometry and meteoritics. Brian Mason, of the Smithsonian Institution, has constructed a model meteorite parent-body shown in Fig. 13. The basaltic achondritic meteorites, high in the pyroxene mineral pigeonite, would come from the "crust". The hypersthene "mantle" would yield the diogenites (hypersthene achondrites). The metals and olivine in the core would contribute the irons and the pallasites (stony-irons composed of olivine and nickel-iron). There are caveats concerning all models and hypotheses for meteorite origins, but it is widely agreed that achondrites, irons, and stony-irons originate from geochemically differentiated bodies of chondritic composition. The density of Mason's model asteroid is about 3.66, in agreement with the measured density of Vesta which contains pigeonitic-basalts on its surface.

A different parent-body model is required for ordinary chondrites, which have not been melted but show different degrees of metamorphism by heat. Perhaps they originate from asteroids too small to have heated sufficiently for differentiation; or in the interior of a body heated from the outside. Or perhaps

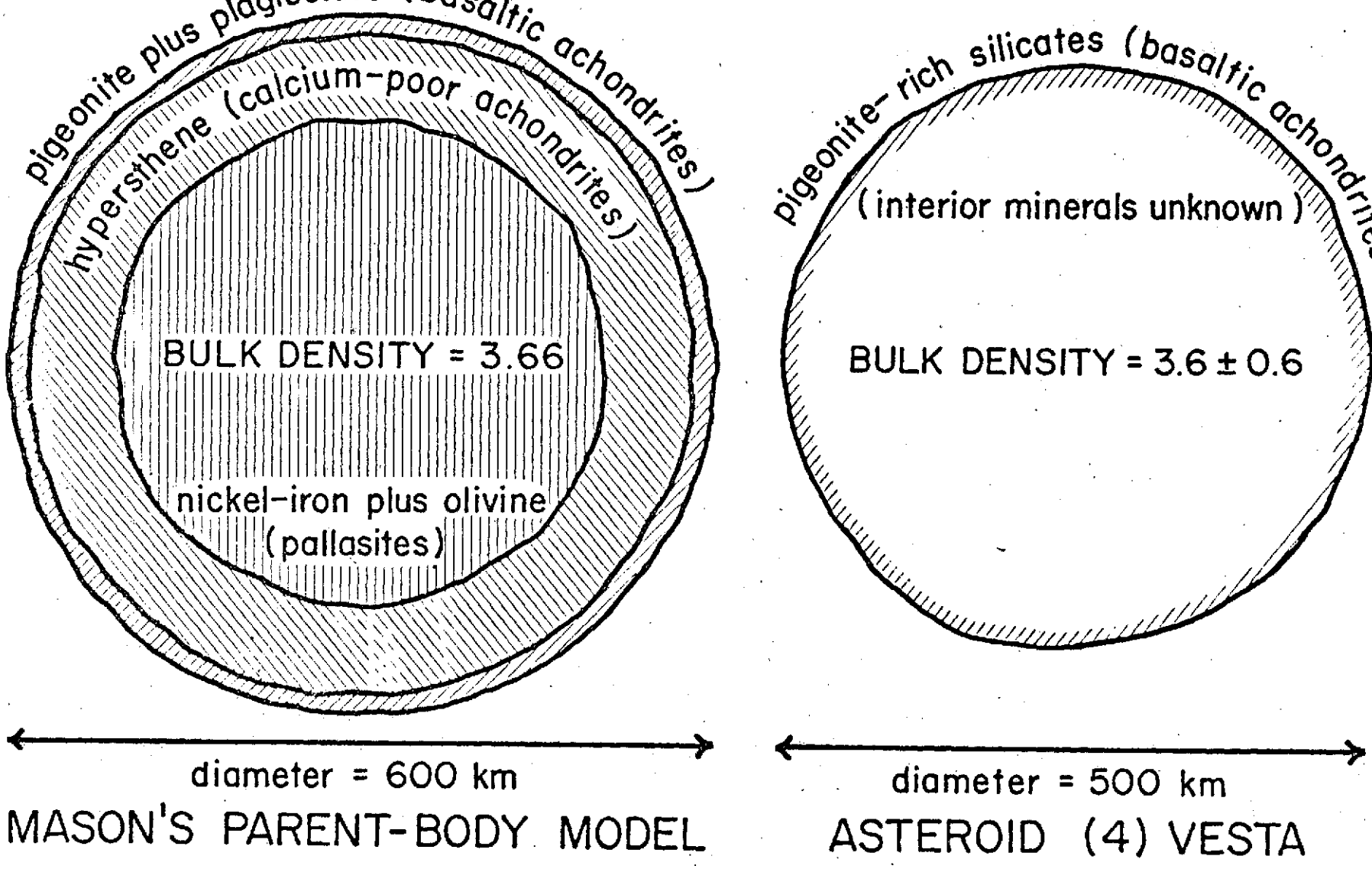
pigeonite plus plagioclase (basaltic achondrites)
hypersthene (calcium-poor achondrites)
BULK DENSITY = 3.66
nickel-iron plus olivine
(pallasites)
diameter = 600 km
MASON'S PARENT-BODY MODEL
pigeonite-rich silicates (basaltic achondrites)
(interior minerals unknown)
BULK DENSITY = 3.6 ± 0.6
diameter = 500 km
ASTEROID (4) VESTA

FIGURE 13

the agglomerating chondritic meteorite material was heated prior to incorporation in larger bodies. A critical question is the source of parent-body heating. Asteroids are too small to be appreciably heated by the gravitational energy of accretion or by radioactive decay processes responsible for heating the earth. The novel idea that some now-extinct short-lived radionuclide caused an early heating episode in rocky objects no longer seems tenable for want of a suitable candidate. Simple heating by the sun, even during the luminous Hayashi phase prior to the arrival of the sun on the stellar main-sequence (a color/luminosity relation that exists for all newly-formed stars) could heat chondritic matter in small bodies, but would be entirely ineffective in heating larger objects. Sonett (1971) has proposed that parent bodies may have been heated by induced electrical currents due to large interplanetary electrical and magnetic fields accompanying a powerful early solar wind. Such a massive solar wind and accompanying rapid solar spin may be a natural phase in the development of a solar-type star, as evidenced by the unusual T Tauri stars. While such ohmic heating processes could melt asteroids, specific predictions are not yet possible about the variation in effectiveness with the object's solar distance, radius, and composition. For instance, the process depends strongly on the electrical conductivity of the material, which is highly temperature-dependent; but the electrical properties of meteoritic materials are only now being measured. It is not even certain whether the dominant heating would be on the outside or the inside of objects of various sizes.

The heating process is constrainted by the necessity to heat Vesta to melting temperatures well in excess of 1000°K while heating Ceres and other asteroids far less. We must also account for the evidence of Papanastassiou and Wasserburg (1974) and others that at least two achondrites may have been formed by magmatic processes a full billion years after the origin of the solar system. It is uncertain whether the magmatic activity continued on or within large asteroids during the entire duration of lunar mare flooding, or whether giant impact melts could have formed these meteorites. Possibly the rubidium-strontium clock used to date these meteorites has been reset by a large impact event and the rocks were really formed earlier in solar system history.

Impact processes certainly have played a major role in shaping many meteorites. Besides the "brecciated" stony meteorites previously described, the mesosiderite stony-irons are physical mixtures of roughly equal parts of nickel-iron and achondrite-like silicates, perhaps produced by the smashing together of an iron body and an achondritic body. Were these brecciated meteorites formed on asteroid surfaces? Perhaps in the distant past, but not recently.

Today, the mean relative impact speed between asteroids is about 5 km/sec. Since asteroids have very small gravitational fields, the spray of material (or "ejecta") from an impact -- which contains 100 to 1000 times the volume of the original particle -- almost entirely escapes into space, though a small residue may remain on the asteroid surface. For millimeter to meter sizes there are many more smaller interplanetary debris particles than larger ones; they continually sandblast away whatever residue has been left by impacts as well as fresh asteroidal rock. Thus, for all except the largest asteroids like Ceres, asteroid soils are thin and poorly developed. Apparently some dust exists, to produce the observed negative polarizations of reflected light, but there is not much of an environment today for creating brecciated, gas-rich meteorites.

Measurements of cosmogenic nuclides show that meteorites have been typically exposed to cosmic rays for about 10^7 years and hence were evidently ejected from their parent bodies about 10^7 years ago. We can calculate from the asteroid size distribution (see Fig. 14) that the greatest fraction of meteorites were produced by the largest few impacts on source asteroids during this 10^7 year duration. These impacts excavated to depths of at least hundreds of meters or possibly a kilometer or more. Since even a meter-deep regolith would constitute only a negligible fraction of ejected mass from such deep excavations, most of the common meteorite breccias were not produced on, and cannot have come from, modern-day asteroid regoliths. Rather, the upper layers of the asteroids must have been already brecciated, either from the later stages of accretion or from the "cataclysmic" period when many meteorites seem to have been degassed by impacts. The solar gasses must have been implanted earlier when these rocks were on the surfaces of accreting bodies.

More recently than 4 aeons ago, the impact rate has declined and the largest asteroids have not been fragmented. But smaller ones occasionally collide and all asteroids are losing mass from cratering at a variety of scales. Some fragments come from originally brecciated parts of the asteroids, others from interior regions exposed to space late in the bombardment period. Breccia layers are being sandblasted away by small-scale impacts and thin layers may be entirely removed revealing reasonably "pure" unbreeciated material.

This, at least, is a tentative picture emerging from a synthesis of meteoritical studies and astronomical data on asteroids. Chondritic matter accreted in the asteroid belt and, at least during later periods of accretion, carbonaceous material predominated beyond 2.3 A.U. Some of the larger objects, of which Vesta is the prime remaining example, were melted or metamorphosed. Many of the others were fragmented or stripped of their exteriors revealing interiors of metals and silicates, accounting for most of the "reddish" asteroids with absorption bands. The relative difficulty of fragmenting metallic cores compared to the friability of the rocky and carbonaceous mantles accounts for the bump in the frequency-relation of Fig. 14 near 150 km diameter. The figure elaborates on an early suggestion of Edward Anders: Imagine the asteroid size-spectrum arose from fragmentation of an initially bell-shaped distribution of accreted planetesimals,

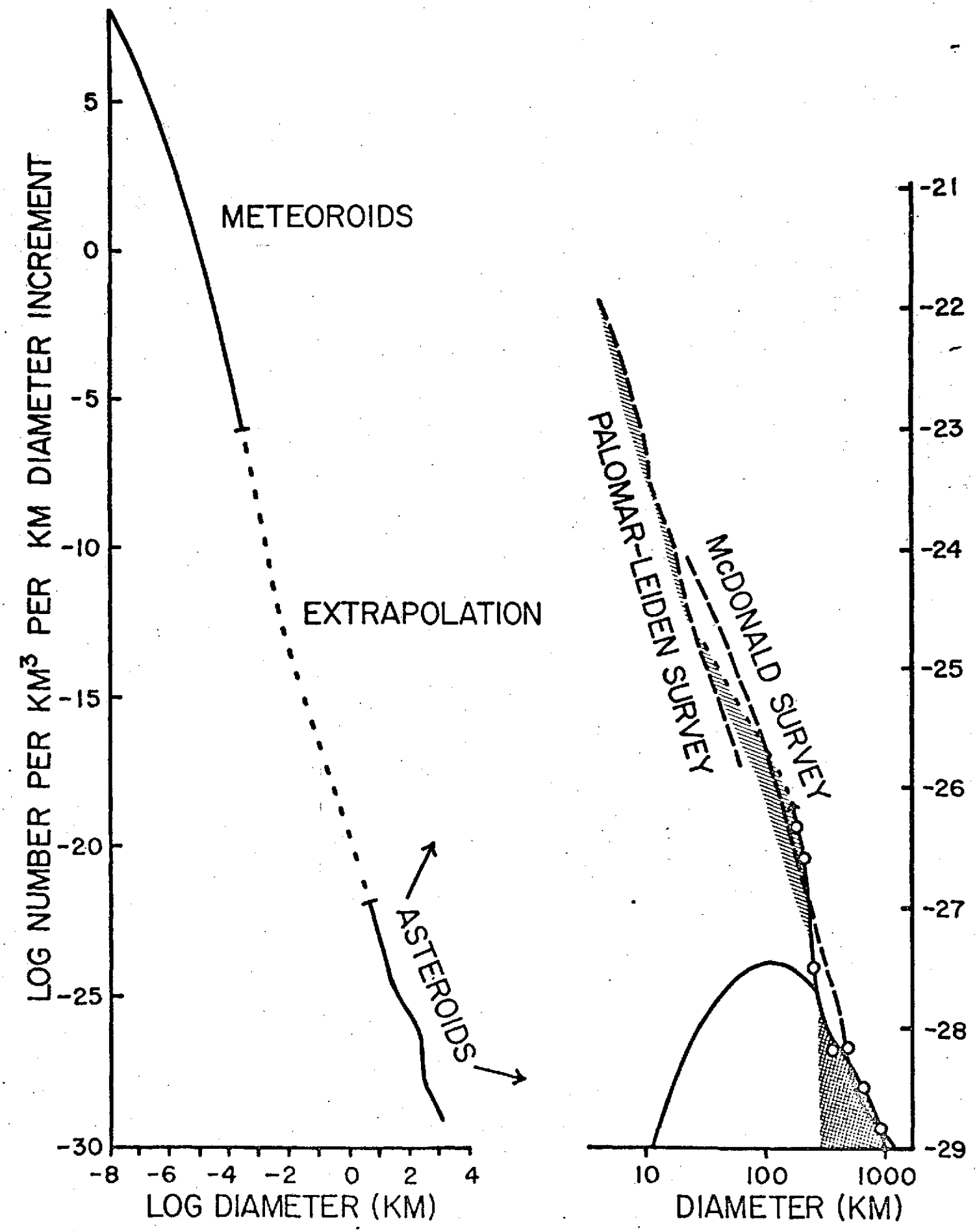
METEOROIDS
EXTRAPOLATION
ASTEROIDS
PALOMAR-LEIDEN SURVEY
McDONALD SURVEY
LOG NUMBER PER KM³ PER KM DIAMETER INCREMENT
LOG DIAMETER (KM)
DIAMETER (KM)
5
0
-5
-10
-15
-20
-25
-30
-8
-6
-4
-2
0
2
4
-21
-22
-23
-24
-25
-26
-27
-28
-29
10
100
1000

FIGURE 14

which were of largely carbonaceous composition at smaller sizes but were differentiated and metamorphosed at diameters exceeding 200 km (cross-hatched area). Most asteroid fragments would be of carbonaceous composition, but the less-easily-fragmented silicates and metals would predominate around 100 km diameter (shading).

Surprisingly few individual asteroids have been found which show a plausible cross-section of layers from one side to the other -- perhaps ranging all the way from primitive, unaltered, carbonaceous chondritic matter to iron core material. The search is underway for such asteroids since these would be ideal targets for geological study by some future asteroid space mission.

REFERENCES

Allen, D. (1971) NASA SP-267, 41.

Bowell, E. and Zellner, B. (1974) in Planets, Stars, and Nebulae Studied with Photopolarimetry (ed. T. Gehrels, U of Ariz. Press), p. 381.

Chapman, C. (1971) PhD thesis, MIT.

Chapman, C. R. and Salisbury, J. W. (1973) Icarus, 19, 507.

Chapman, C. R., McCord, T. and Johnson, T. V. (1973a) A.J., 78, 126.

Chapman, C. R., McCord, T. and Pieters, C. (1973b) A.J., 78, 502.

Chapman, C. R. (1974) Presentation at Meteoritical Society Meeting, UCLA, August, 1974; also Scientific American, in press.

Chapman, C. R. (1975) in preparation

Chapman, C. R., Morrison, D. and Zellner, B. (1975) in preparation.

Cruikshank, D. and Morrison, D. (1973) Icarus, 20, 477.

Dunlap, J. L. (1974) A.J., 79, 324.

Egan, W. G., Veverka, J. Noland, M. and Hilgeman, T. (1973) Icarus, 19, 358.

Gaffey, M.(1974) PhD thesis, MIT.

Gaffey, M. and McCord, T. (1974, 5) in preparation.

Hartmann, W. K., Chapman, C.R. and Williams, J. G. (1975) Rev. Geoph., in preparation.

Hertz, H.G. (1968) Science 160, 299.

Howes, M. L. and Gehrels, T. (1974) A.J., in press.

Hunt, G. R. and Salisbury, J. W. (1970) Mod. Geol., 1, 283.

Johnson, T. V. and Fanale, F. P. (1973) J. Geoph. Res., 78, 8507.

Johnson, T.V. and Matson, D. L. (1975) in preparation.

Larson, H. and Fink, U. (1975) in preparation.

Lewis, J. (1974) Sci. Am., in press.

Matson, D. L. (1971) California Institute of Technology thesis.

Matson, D.L., Veeder, G. and Johnson, T.V. (1974), in preparation.

McCord, T., Adams, J. B. and Johnson, T. V.(1970) Science, 168, 1445.

McCord, T. and Gaffey, M. (1974)Science, in press.

McCord, T. and Chapman, C. R. (1975a) Ap. J., in press.

McCord, T. and Chapman, C. R. (1975b), in preparation.

Morrison, D. (1974) Ap.J., in press.

Nash, D. B. and Conel, J.E. (1974) J. Geoph. Res., 79, 1615.

Opik, E.J. (1966) Adv. Astron. Astrophys., 4, 302.

Papanastassiou, D. and Wasserburg, G. (1974) Geophys. Res. Lett., 1, 23.

Ross, H. P., Adler, J., and Hunt, G.R. (1969) Icarus, 11, 46.

Salisbury, J.W. and Hunt, G.R. (1974) Mod. Geo., in press.

Schubart, J. (1974) Astron. and Astrophys., 30, 189.

Sonett, C. P. (1971) NASA SP-267, 239.

Van Schmuss, W.R. and Wood, J.A. (1967) Geochim. Cosmochim. Acta, 31, 747.

Veverka, J. and Noland, M. (1973) Icarus, 19, 130.

Wetherill, G. (1971) NASA SP-267, 447.

Zellner, B., Gehrels, T., and Gradie, J. (1974), A.J., in press.

TASK 2: ASTEROID ORBITAL CORRELATIONS
(Principal Investigator: Donald R. Davis)

The purpose of this task was to examine possible correlations of asteroid spectral reflectivity characteristics and orbital parameters. An initial report on this project was presented at the April meeting of the Division of Planetary Science of the AAS in Palo Alto. The number of asteroids whose spectral curves have been measured has increased from 68 to 94 since that report. The results of this investigation are described in a preprint of a paper prepared for submission to Icarus and contained in Appendix I.

TASK 4: LABORATORY SPECTROPHOTOMETRIC PROGRAM
(Principal Investigator: Donald R. Davis)

This task proposed to utilize a spectrophotometric goniometer, developed by the IIT Research Institute (IITRI) under a previous contract (NASW 2-280-71-001-73), to measure the photometric function of a series of selected rock and soil samples. The project was somewhat hampered by the fact that the instrument as received from IITRI was far from complete and had never been completely assembled and tested as was assumed in the initial proposal. Nonetheless it was possible to complete the instrument and to make preliminary measurements on several rock and soil samples. At the time of the initiation of this effort, the project stood in the following condition:

(1) The basic machine shop work had been done on the framework.

(2) The main components had been purchased for the optical system.

(3) The electronic equipment (amplifiers, recorders, power supplies) had not been designated or supplied.

(4) The narrowband (optical) filter system had not been obtained.

The initial effort required that sufficient electronics and filters be obtained in order to have a functioning instrument. This was accomplished through the loan of the following equipment:

(1) D.C. Power Supply

(2) A.C. Preamplifier and Amplifer

(3) Brown Strip Chart Recorder

(4) Narrowband Interference Filters

Unfortunately, the principal difficulties were with the borrowed parts of the system, and so the capital investment in effort involved in solving the problems will not be retained. The investment was necessary, however, in order to prove out the design of the projected system and to obtain measurements.

Briefly, the problems encountered were:

(1) Zero point drift of the D.C. amplifer; 10% of full scale deflection on a timescale of minutes (more at higher gains).

(2) Voltage drift of the (unregulated) lamp power supply; 10% (corresponding to light intensity drift of 20%) on a timescale of tens of minutes.

(3) Preamp saturation at signal levels corresponding to the white reflectance standard with highly filtered illumination.

(4) Apparent long-term variation in the relative gains of the amplifier at different 40% on a timescale of months.

(5) Insufficient coverage of the spectrum by the borrowed filter collection; many had such low transmission as to bury the signal in . Other filters potentially usable were not available at the time when measurements were being carried out but would be available for future measurements.

Nevertheless, enough of these problems were corrected to enable us to compensate for the others (by taking measurements as rapidly as possible consistent with long integration times) enough to develop measurements of rock and powder samples at a confidence level of about 5%. These measurements consist of reflectivity measurements at various angles of reflectance (phase angles) in terms of the reflectivity of a quantity of Eastman white reflectance standard at near normal incidence/emergence. These measurements were made at two narrow regions of the spectrum, 5680Å (yellow-green) and 8900Å (near IR). Measurements were also made in unfiltered white light (with the spectral character of an incandescent lamp), and with a Wratten 29 "red" filter (a low-pass filter cutting off at about 7000Å). The samples chosen were: a specimen of lava from the Pinacate volcanic region, in Sonora, Mexico, a limonite-stained granite from the Santa Catalina mountain range, and two samples of orangish-ochre desert soil chosen for possible similarity to

The figures 1-4 represent the spectral reflectivities vs reflectance angle for the samples. There is a discontinuity in many of the curves at 50°, where the reflectance angle was reversed in sign, giving an idea of the irregularities of the sample. The spectral coverage is poor, because of the filter problems mentioned. Nevertheless, the data on the whole is consistent with their general appearance.

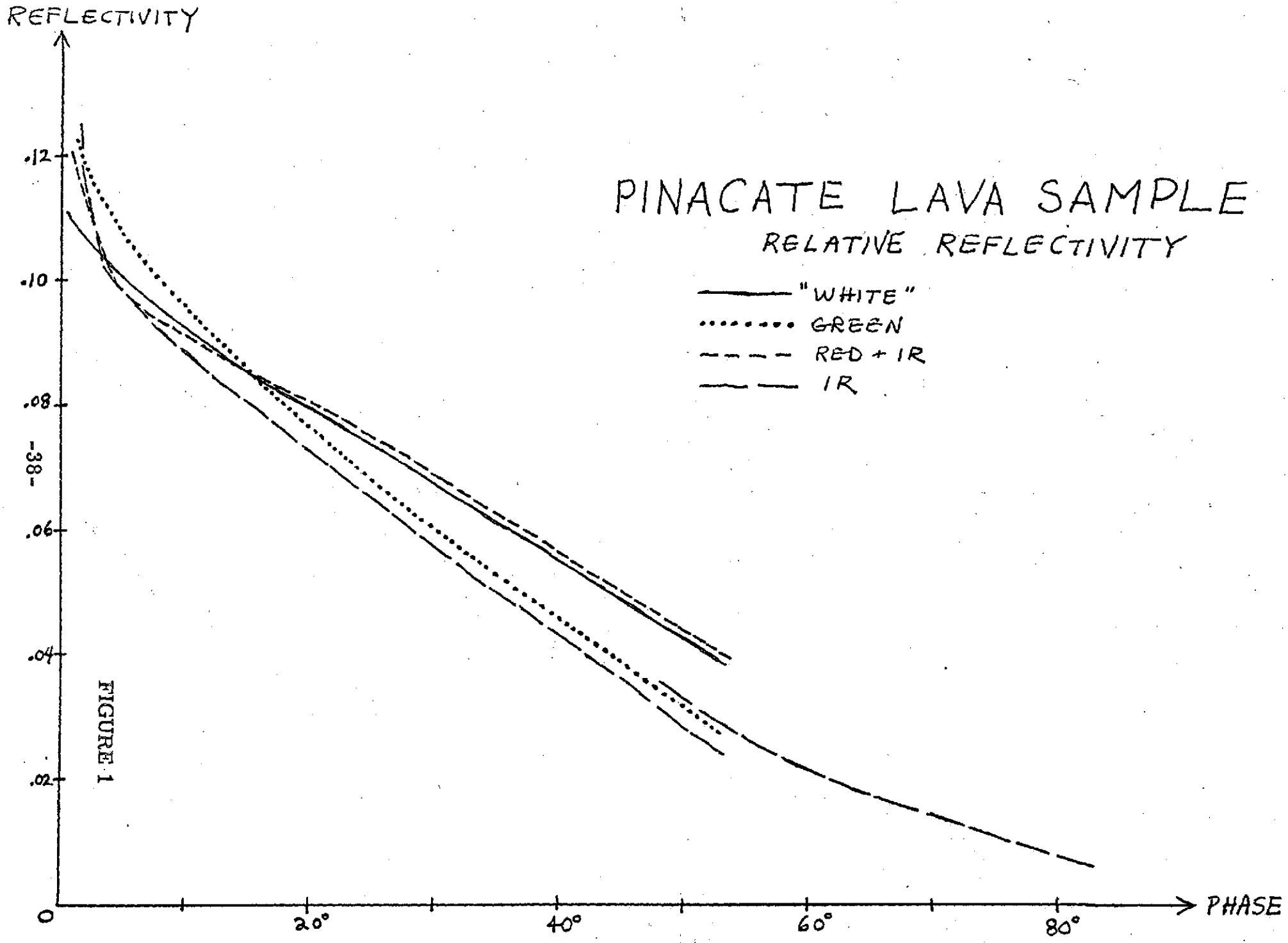
REFLECTIVITY
.12
.10
.08
.06
.04
.02
0
20°
40°
60°
80°
PHASE
PINACATE LAVA SAMPLE
RELATIVE REFLECTIVITY
"WHITE"
GREEN
RED + IR
IR

FIGURE 1

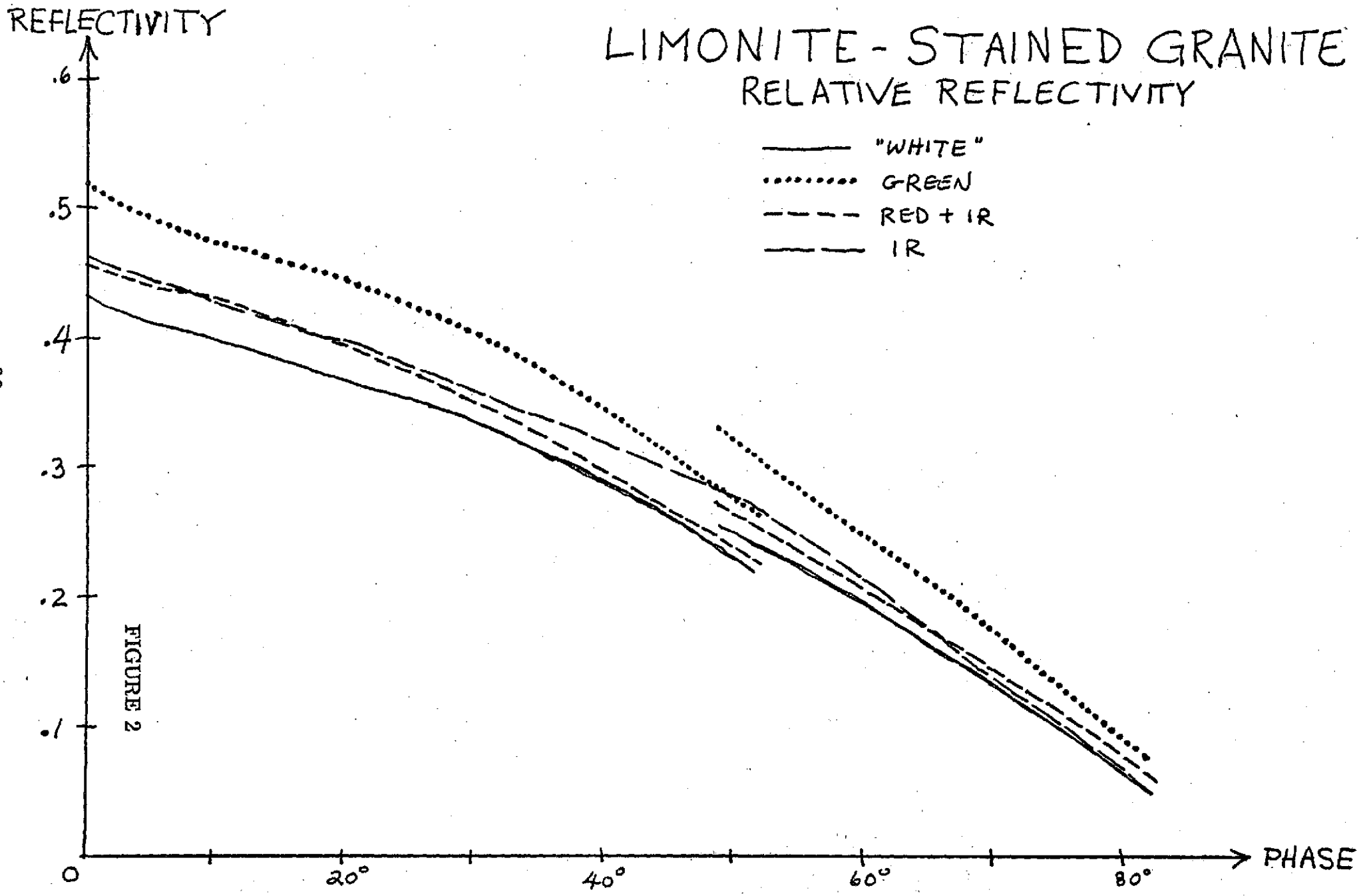
LIMONITE - STAINED GRANITE
RELATIVE REFLECTIVITY
"WHITE"
GREEN
RED + IR
IR
REFLECTIVITY
.6
.5
.4
.3
.2
.1
0
20°
40°
60°
80°
PHASE

FIGURE 2

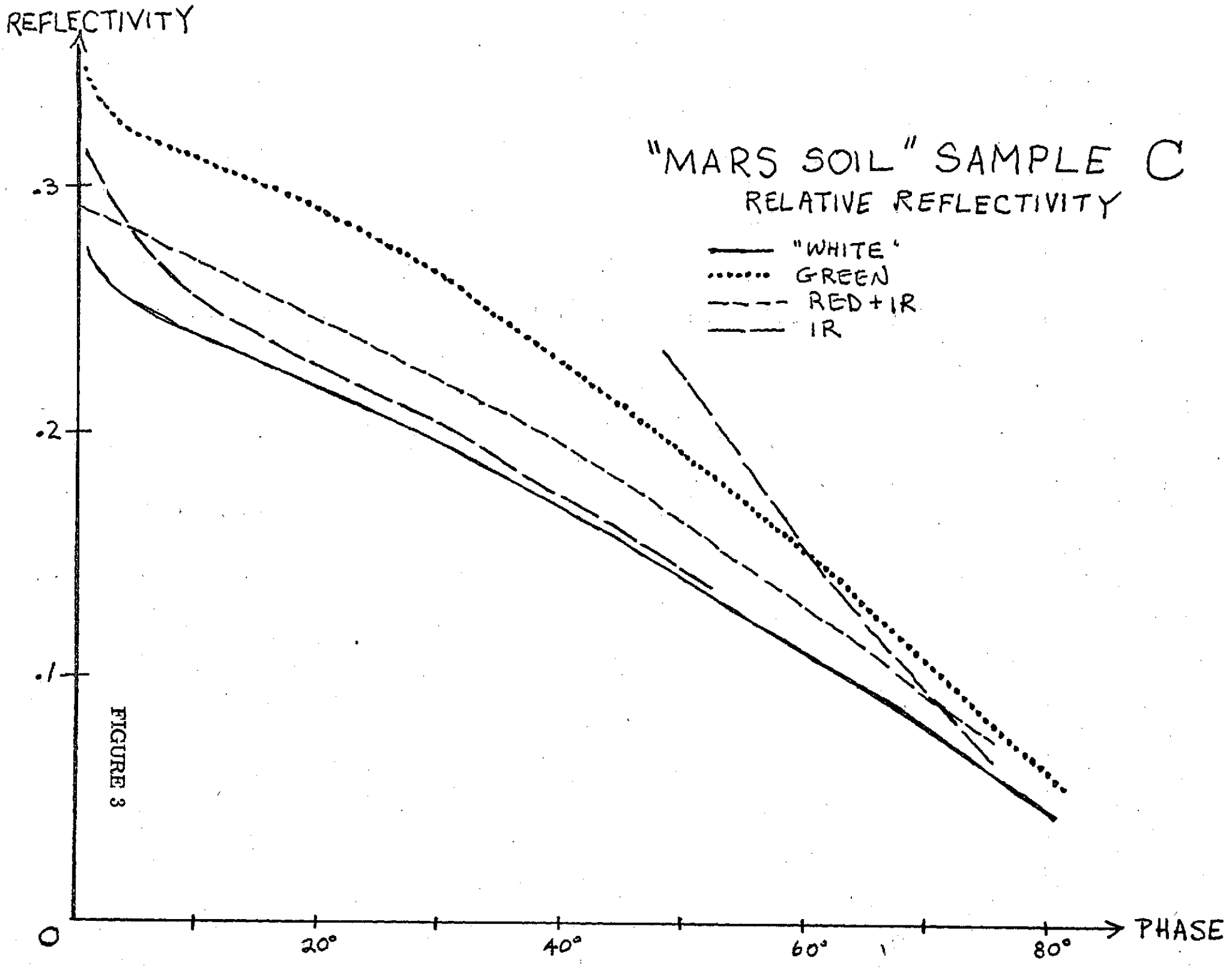
REFLECTIVITY
"MARS SOIL" SAMPLE C
RELATIVE REFLECTIVITY
"WHITE"
GREEN
RED + IR
IR
.3
.2
.1
0
20°
40°
60°
80°
PHASE

FIGURE 3

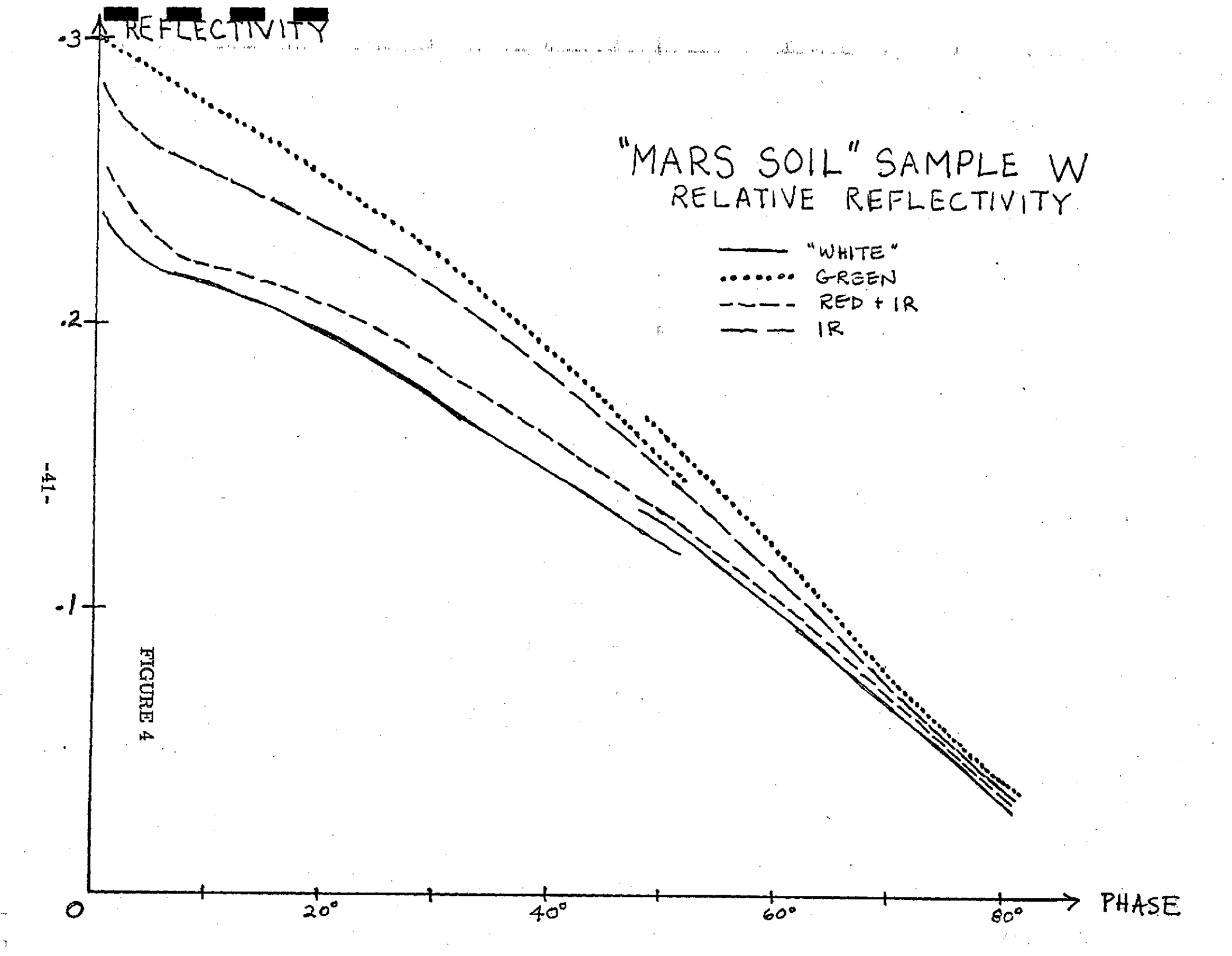
REFLECTIVITY
.3
.2
.1
0
20°
40°
60°
80°
PHASE
"MARS SOIL" SAMPLE W
RELATIVE REFLECTIVITY
"WHITE"
GREEN
RED + IR
IR

FIGURE 4

The Pinacate lava sample, a highly vesicular rock, showed at all wavelengths the rapid decline of reflectivity with increasingly oblique angle of reflectance. Its somewhat neutral color (a reddish-purple brown) is reflected in the similarity of the curves in various colors. The "red" (red + IR) and "white" (all wavelengths, weighted by lamp spectral emissivity) reflections are the strongest, while the IR and green are lower.

The limonite-stained granite, an orange rock with relatively smooth surfaces, has a much slower decline of reflectivity with increasing phase. The highest reflectivity is in the yellow-green, with red + IR, and IR, at about the same lower reflectance level. Lowest of all is the "white" suggesting a strong fall-off in the blue is indicated.

The two soil samples' decline in reflectivity with increasing phase was intermediate between that of the vesicular lava and the smooth granite. Their orange-ochre color is again reflected in the prominence of the yellow-green reflectivity. Sample "C", a more saturated orange, has a red + IR reflectance well above the IR and "white". Sample "W", on the otherhand, a duller and browner material, has a relatively higher IR reflectance with red + IR and "white" depressed. The inference one might draw from this is that there are strong dips in the reflectivity at the red and blue wavelengths. This is somewhat at variance with the visually evident lack of color saturation.

All the samples (and indeed the white standard itself) show a strong peak in reflectivity at near normal incidence. This could conceivably be specular reflection in the instrument (such an effect was, in fact, discovered and removed prior to these observations) but its inconsistency from sample to sample and color to color makes this seem unlikely. More probably, it results from the effect, well-known in rough objects, of disappearance of mutual shadowing at small phase angles.

The principal output from this task has been the completion and initial preliminary utilization of the laboratory spectrophotogoniometer. This instrument is now capable of reflectivity measurements over a wide range of wavelengths (0.4 μm - 2.4 μm) with both the angle of incidence and angle of emission being separately variable. With more suitable electronics and filters, measurements are certainly feasible to an accuracy level of 1%. Given the roughness and irregularities found in most rock and soil samples, more accuracy is not needed and it is questionable that even this level is required. Potential future uses for the instrument are sample measurements for comparison with data returned from the viking Lander Camera and sample measurements for comparison with asteroid spectral reflectivity data.

TASKS 5 AND 6: INTRODUCTORY REMARKS
(Principal Investigator: Michael J. Price)

Investigation of physical models of the Saturn ring system was successfully carried out. First, photometric function data at visual wavelengths were analyzed using multiple scattering theory. Simple anisotropic scattering models were used. Results indicate that the ring particles are pronounced back-scatterers of radiation, the single scattering albedo being greater than 75 percent. The mean perpendicular optical thickness of the ring system (rings A and B only) is greater than 0.7. Macroscopic ice-particles (radii ~ 1-2 cms.) are consistent with the data. But more significant, however, is our rejection of the concept of mutual shadowing among the ring particles. By so doing, theoretical studies of the detailed scattering properties of Saturn's ring become feasible. Complete results are reported in a paper entitled "Optical Scattering Properties of Saturn's Ring II.", which will appear shortly in Icarus. Our ring model can be tested by utilizing the Pioneer 11 spacecraft. Quantitative predictions of the visual appearance of the ring system, as viewed from the spacecraft, have been made. In view of the generality of the predictions, they will also be relevant to the pair of 1977 Mariner Jupiter-Saturn missions. Full details are reported in a paper entitled, "Saturn's Ring and Pioneer 11", which will be submitted for publication in Icarus. Second, initial development of a novel technique for inferring the scattering phase function of the individual ring particles has been completed. In essence, the technique utilizes indirect solar illumination of the ring, via the ball of the planet, to increase the phase angle coverage; scattering angle is a function of azimuth in the ring plane. Detection of the indirect contribution to the surface brightness of the ring has been achieved using electronography. Complete details of the observations, and their analysis, is contained in a paper, entitled "Indirect Illumination of Saturn's Ring via the Ball of the Planet. I. Detection," which will be submitted for publication in Icarus. Preprints of the three Saturn ring papers written during the contract period are included later in this report as Appendix II.

Two additional outer planet tasks were carried out during the current contract. The atmospheric study of Titan attempted using high-dispersion image-tube spectrography was not successful. Although Titan was successfully observed, the spectrograms were not of sufficient quality to provide new information on its atmosphere. By contrast, study of the optical scattering properties of the Uranus atmosphere was quite a success. Initial application of photoelectric area-scanning to the investigation of the limb-brightening phenomenon was satisfactorily carried out. Indications of limb-brightening in the λ6190Å CH_4 band were discovered. More complete descriptions of both projects are included in this report.

TASK 5: SATURN RING SYSTEM: INVESTIGATION OF PHYSICAL MODELS
(Principal Investigator: Michael J. Price)

Preprints of papers written during the contract period summarize the results. Their titles are:

1. "Optical Scattering Properties of Saturn's Ring. II."

2. "Saturn's Ring and Pioneer 11."

3. "Indirect Illumination of Saturn's Ring by the Ball. I. Detection."

TASK 6: TITAN: ATMOSPHERIC STUDIES USING HIGH-DISPERSION IMAGE-TUBE SPECTROPHOTOMETRY
(Principal Investigator: Michael J. Price)

1. Introduction

Indirect determination of the H_2 columnar-abundance on Titan can be made by using a technique developed by Owen and Mason (Ap. J. 154, 317, 1968; J. Atmos. Sci. 26, 870, 1969) and by Owen (Icarus 10, 355, 1969) for inferring an upper limit to the helium abundance in the Jovian atmosphere. By measuring the half-widths of individual lines in the λ6190Å CH_4 band, the presence of gases other than CH_4 can be detected. If methane molecules predominate, the half-width will be the result of Doppler and self-broadening; if H_2 molecules predominate, the half-width will be determined largely by pressure-broadening.

2. Observations

High dispersion (4Å/mm) Titan spectrograms of the λ6190Å CH_4 band region were obtained during the Fall of 1972 using the KPNO 84-inch reflector/No. 6 coudé camera system. Spectra were recorded using an ITT image tube (S-20 photocathode; 40 mm diameter). Kodak IIaD plates were used, calibration being achieved with a spot sensitometer. The phosphor screen of the ITT tube was calibrated using the moon as a light source. The same equipment and observational technique was used earlier in 1972 to determine the scattering mean free path in the Uranus atmosphere from spectrophotometry of the H_2 quadrupole lines. Complete details of the observational method have been published by Price (1973, Icarus 20, 455). The Titan observing log is shown in Table I.

TABLE 1

OBSERVING LOG FOR TITAN PROJECT: SUMMARY OF PLATES

1. 1972 November 9. Focus plate. Neon 5 secs. Developed alone in D-19 for 5 minutes.

2. 1972 November 13. Focus plate. Neon 5 secs. Developed alone in D-19 for 5 minutes.

3. 1972 November 14. D-3424. Test exposure. Moon 30 secs. Decker #8. Neon comparison 5 secs. Developed alone in D-19 for 5 minutes.

4. 1972 November 14. D-3425. Moon 45 secs. Decker #8. Neon comparison 5 secs. Developed with D-3426 and Spot Sensitometer Calibration in D-76 for 15 minutes.

5. 1972 November 14. D-3426. Titan 3^h0^m. Decker #9. Neon comparison 5 secs. Untrailed exposure. Developed with D-3425 and Spot Sensitometer Calibration in D-76 for 15 minutes.

6. 1972 November 14. Spot Sensitometer Calibration for D-3425 and D-3426. Exposure 45 minutes. Developed with D-3425 and D-3426 in D-76 for 15 minutes.

7. 1972 November 14. D-3427. Titan 3^h48^m. Decker #8. Neon comparison 5 secs. Trailed. Developed with Spot Sensitometer Calibration in D-76 for 15 minutes. Seeing $< 1''$ arc.

8. 1972 November 14. Spot Sensitometer Calibration in D-3427. Exposure 45 minutes. Developed with D-3427 in D-76 for 15 minutes.

9. 1972 November 15. D-3428. Moon 45 secs. Decker #8. Neon comparison 5 secs. Developed alone in D-76 for 15 minutes.

10. 1972 November 16. D-3429. Moon 120 secs. Decker #8. Neon comparison 5 secs. Developed with Spot Sensitometer Calibration in D-76 for 15 minutes.

11. 1972 November 16. Spot Sensitometer Calibration for D-3429. Exposure 45 minutes. Developed with D-3429 in D-76 for 15 minutes.

12. 1972 November 17. D-3430. Moon 45 secs. Decker #8. Neon comparison 5 secs. Developed with D-3431 and Spot Sensitometer Calibration in D-76 for 15 minutes.

13. 1972 November 17. D-3431. Titan 4^h0^m. Decker #8. Neon comparison 5 secs. Developed with D-3430 and Spot Sensitometer Calibration in D-76 for 15 minutes.

14. 1972 November 17. Spot Sensitometer Calibration for D-3430 and D-3431. Exposure 45 minutes. Developed with D-3430 and D-3431 in D-76 for 15 minutes.

3. Data Analysis

Thorough examination of the observational data showed that plates #12, #13 and #14 were unusable because of uneven development. In addition, because of geometrical distortion produced in the image tube, the spectrogram on plate #5 is too narrow for reliable microdensitometry. Our analysis was restricted to plates #4 and #6, and to plates #7 and #8. Microdensitometry was carried out using the KPNO Joyce-Loebl machine. The data for plate #7 are shown in Figs. 1a, 1b, and 1c. Top tracings correspond to spectrogram density as a function of wavelength. Bottom tracings are scans giving the background noise level of the tube; they refer to the region of the spectrogram displaced perpendicular to, but parallel and immediately adjacent to, the Titan spectrum. Note that the ordinate scale is truncated at its lower base. In fact, the tracings have a signal/noise level ~3 only. The background noise level of the tube was a factor 2-3 greater than expected. Predicted positions of the CH_4 lines listed in Table 2 are shown. Each position has been corrected for the Doppler effect (-0.102Å); line strengths refer to the Saturn spectrum. Equivalent widths of the individual CH_4 lines are expected to be small. For comparison, Owen and Mason (1968) found that the corresponding lines in the Jupiter spectrum had equivalent widths ~10mÅ. Because the ratio S/N is so low, detection of the individual CH_4 lines was not achieved. Reasons for the high background noise are not clear. Although special precautions were taken to eliminate electronic problems, coronal discharges may have caused the excessive background level.

TASK 7: URANUS: ATMOSPHERIC OPTICAL SCATTERING PROPERTIES

(Principal Investigator: Michael J. Price

1. Introduction

To investigate the degree of clarity of the Uranus atmosphere, we proposed to observe the presence of limb-darkening/limb-brightening as a function of wavelength and position on the disk. To check predictions by Belton and Price (Astrophys. J. 179, 965, 1973) we originally proposed to obtain high-dispersion spectrograms of Uranus taken under excellent seeing conditions to insure sharp spatial resolution perpendicular to the dispersion. By holding the image of Uranus steady on the spectrograph slit, the edges of the spectrogram would correspond to the limb of the planet, while the mid-length point would correspond to the center of the disk. By studying the variation with wavelength of the intensity perpendicular to the dispersion, the wavelength at which changeovers from limb-darkening to limb-brightening occur would be obtained. Fundamental to the success of the project would be excellent seeing, maximum image scale, an excellent high dispersion spectrograph, and reliable photometric calibration of the spectrograms obtained. On the basis of these considerations, we proposed to secure the necessary data at Cerro Tololo Inter-American Observatory, utilizing the 60-inch aperture telescope/coudé spectrograph.

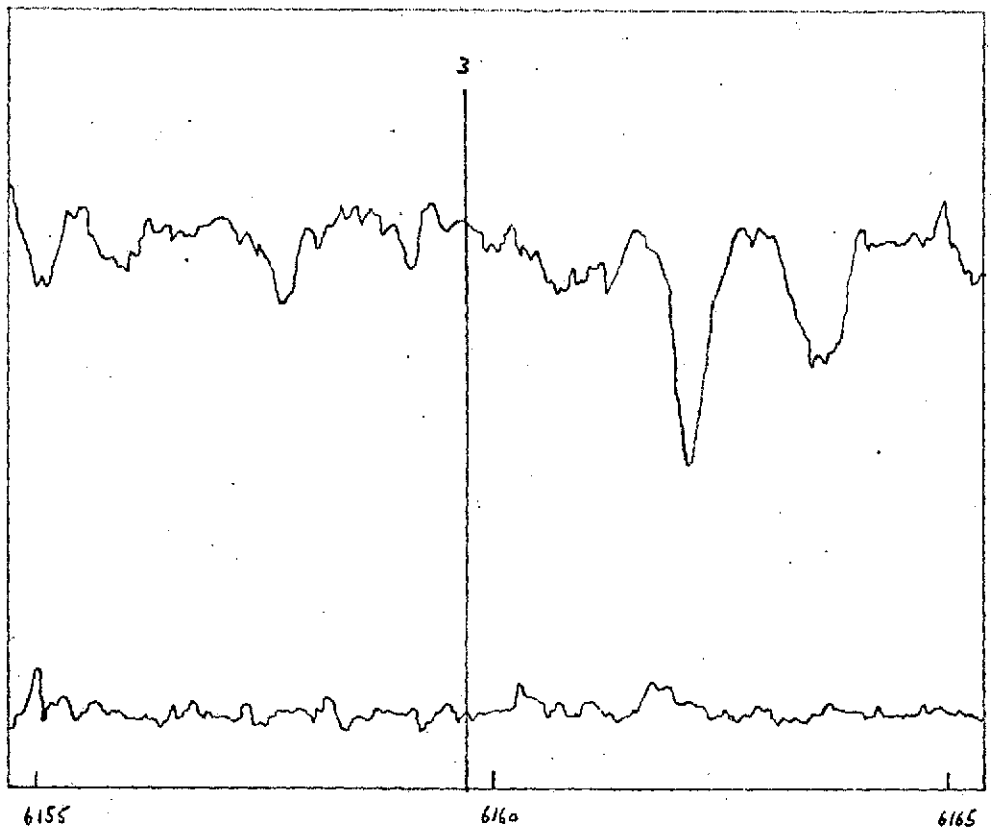

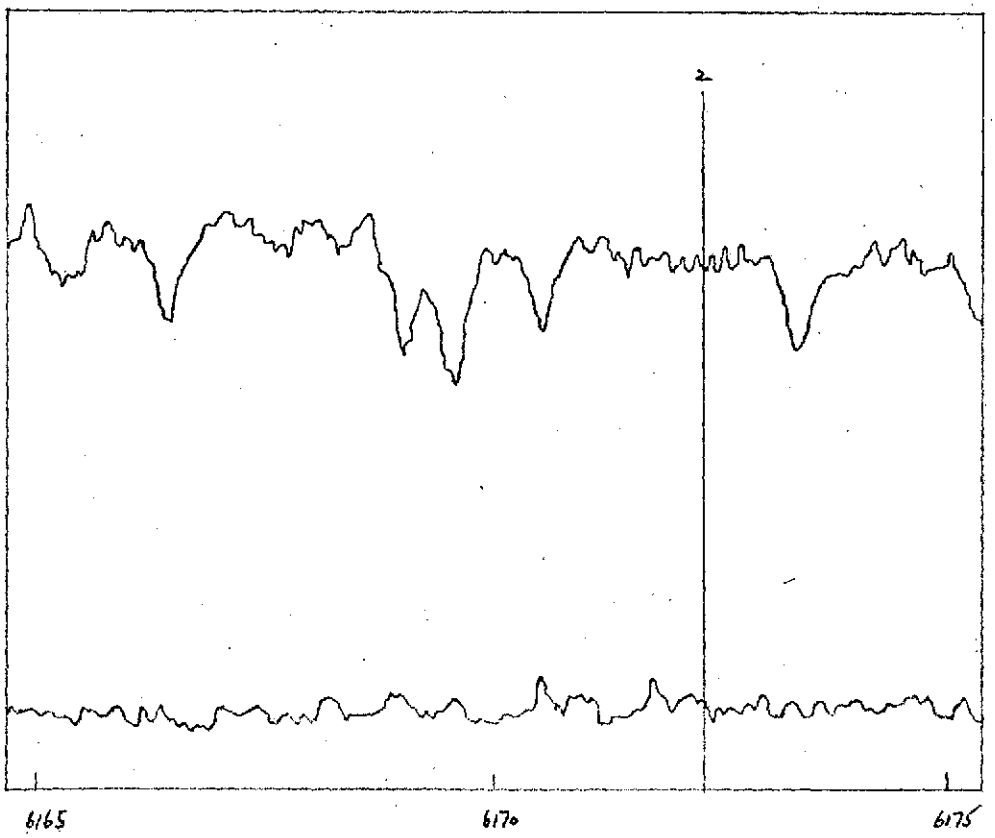

TITAN

Fig. 1a

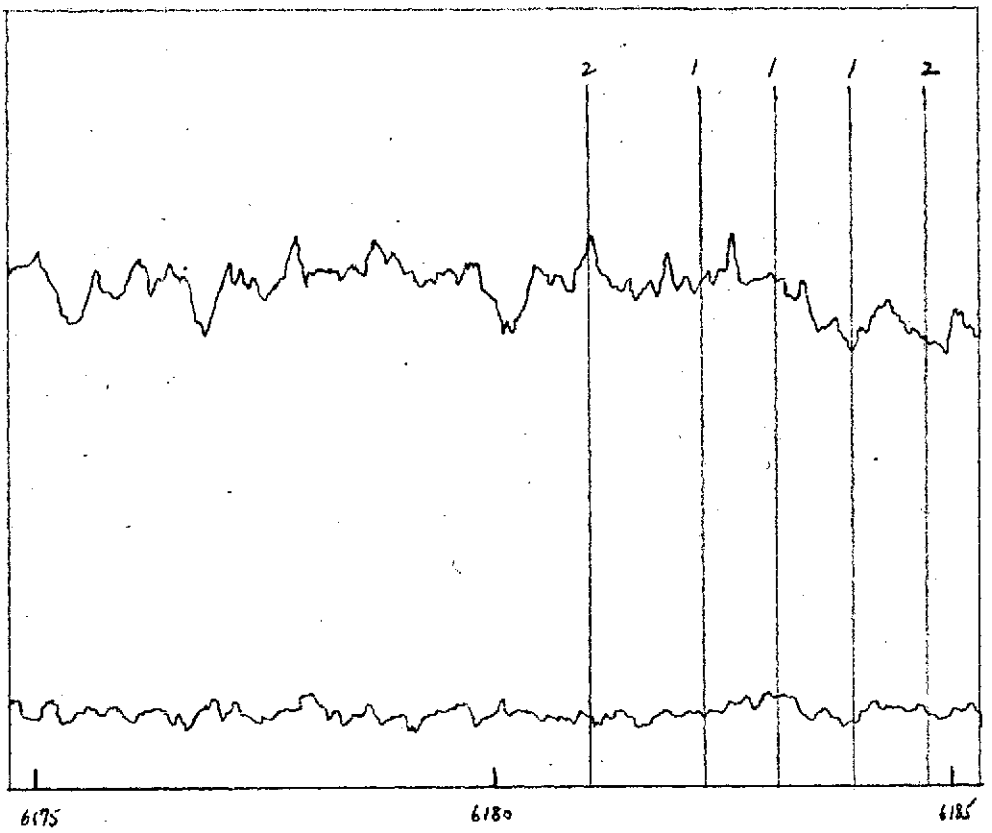

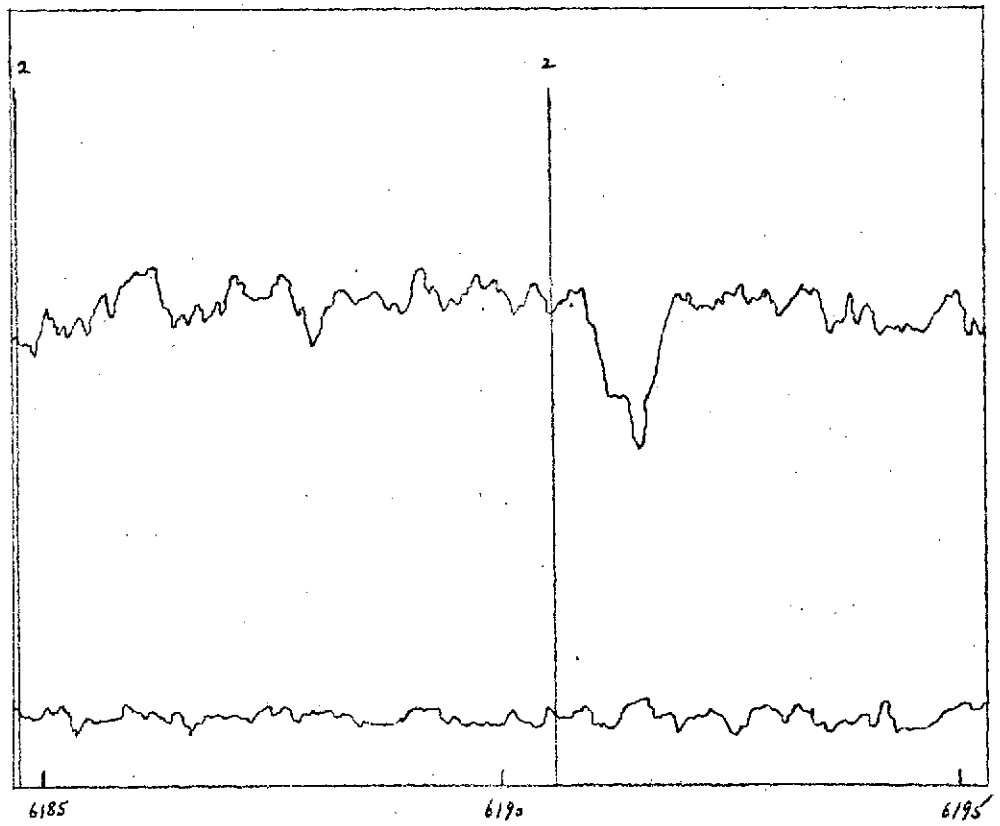

TITAN

Fig. 16

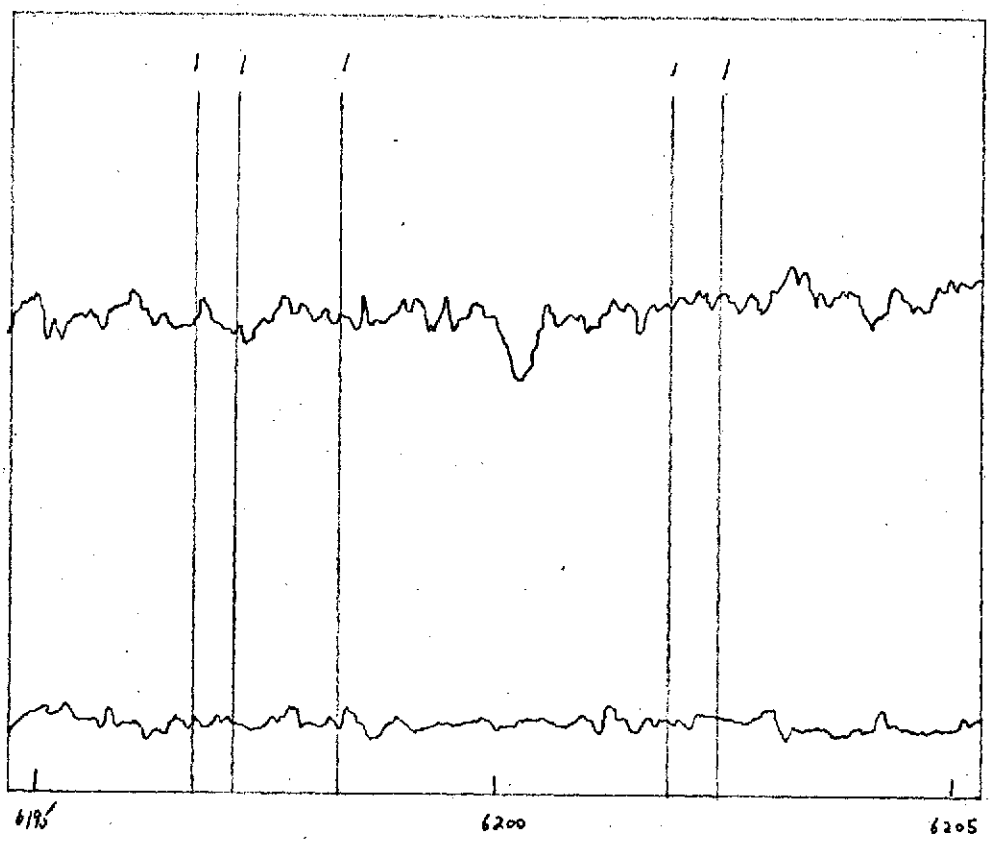

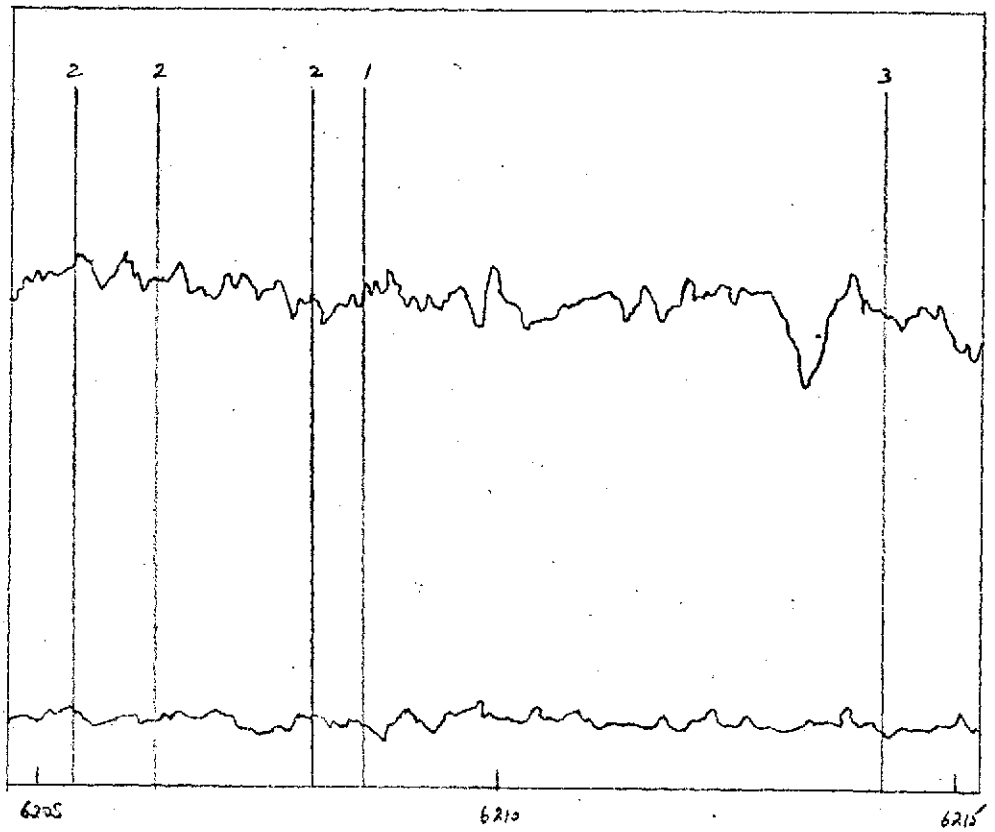

TITAN

Fig. 1c

TABLE 2

INDIVIDUAL LINES IN λ6190Å CH_4 BAND: CANDIDATES FOR SEARCH*

Wavelength (Å)	Laboratory Strength (300 °K)	Jupiter Strength (150 °K)	Saturn Strength (88 °K)
6159.71	3	3	3
6172.29	3	3	2
6180.98	2	3	2
6182.22	1	2	1
6183.04	1	2	1
6183.92	2	1	1
6184.75	2	3	2
6190.66	1	2	2
6196.86	1	2	1
6197.37	2	2	1
6198.45	1	2	1
6201.97	2	2	1
6202.51	2	1	1
6205.49	2	2	2
6206.39	2	2	2
6208.07	2	2	2
6208.71	3	2	1
6214.27	3	1	3

* Information taken from Spinrad and Trafton (1963, Icarus 2, 19). Line strengths on a scale strong (1), weak (3). Wavelengths are the averages for the Laboratory and Saturn.

Since making our original proposal, however, a far better technique for investigating the limb-brightening phenomenon became available. Because photographic spectrophotometry requires extremely accurate plate calibration to be reliable, photoelectric study of the Uranus spectrum is infinitely preferable. Plans, approved by NASA, were made to investigate the limb-brightening phenomenon in collaboration with Dr. Otto Franz at Lowell Observatory using a photoelectric scanner designed for photometric and astrometric observations of visual double stars; it is eminently suitable for the Uranus project. Descriptions of the device, of the associated data acquisition system, and examples of typical double star scans are given in Lowell Observatory Bulletin No. 154 (1970 December 15). To accurately define (±10%) the geometrical albedo of Uranus at which changeovers of its center-to-limb characteristics occur, scanner observations at up to nine characteristic wavelengths were planned during the first half of 1974 (cf: Fig. 1). Characteristic wavelengths could be selected by intermediate-band (±100Å) filters (cf: Table I). Observations would be made primarily with the 72-inch aperture Perkins reflector. By incorporating the Uranus project into his regularly scheduled program of double star observations, Dr. Franz would have available a minimum of ~60 nights to attempt the observations. Good seeing condtions should therefore occur not infrequently.

2. Equipment

Our basic instrument was the photoelectric area-scanner, designed and built for double-star observations by Franz (1970, Lowell Observatory Bulletin No. 154), mounted on the 72-inch aperture Perkins reflector at Lowell Observatory. Two replacement modules, designed specifically to expedite the Uranus observations were built. First, a special-purpose filter-box capable of holding six 1-inch circular or square narrow-band optical filters was constructed. Second, a photomultiplier cold-box capable of holding an EMI 9558 S-20 tube was constructed; use of a red-sensitive photocathode is essential. We were fortunate enough to secure the long-term loan of a pair of EMI 9558 tubes from the Ohio State University. Costs for both modules were borne by Lowell Observatory.

Optimum scanning of the Uranus image requires that the signal area-scanning slit be replaced by a circular pin-hole aperture. Two pinholes were obtained with diameters of 100 μm (0.65 arc sec.) and 200 μm (1.3 arc sec.), respectively. Table I lists the narrow-band filters finally selected for the Uranus project. Each filter has a half-width ~100Å.

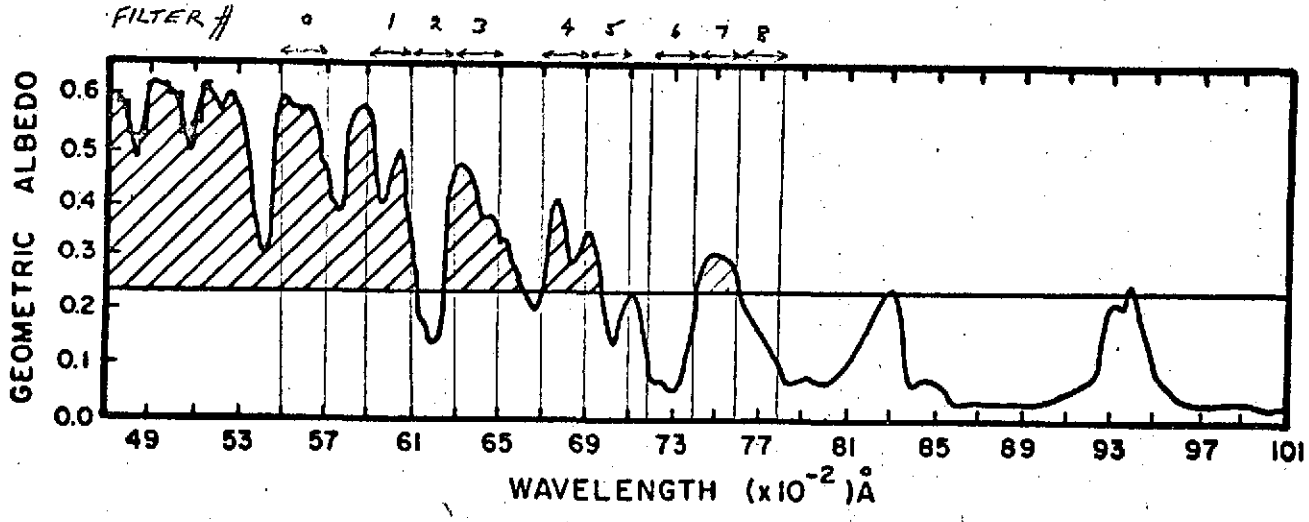

Fig. 1: The variation of geometric albedo on Uranus with wavelength (after R. L. Younkin, 1970, thesis, University of California, Los Angeles). The line at p = 0.23 shows where changeovers of the center-to-limb characteristics are expected to occur. The shaded portions of the diagram correspond to limb-darkening; the unshaded to limb-brightening.

TABLE I

URANUS PROJECT FILTERS

No.	Effective Wavelength (Å)
0	5600
1	6000
2	6200
3	6400
4	6800
5	7000
6	7300*
7	7500*
8	7700

Filters marked with an asterisk were purchased from Infrared Industries, Inc., Waltham, Mass. All others were obtained from Optical Coating Laboratory, Inc., Santa Rosa, California. Filter and pinhole costs were borne by Planetary Science Institute under the current NASA Planetary Astronomy contract.

3. Observations

Manpower effort assigned to the Uranus project during the current contract was extremely limited. Careful selection of the observational program was, therefore, required in order to insure securing important new results. We determined to limit the observational program to an investigation of limb-brightening in the λ6190Å CH_4 band only. Not only would detection of limb-brightening be a direct observational check of the Belton and Price (1973) predictions, but it would also convincingly demonstrate the applicability of the Franz area-scanner to a thorough, detailed investigation of the limb-brightening phenomenon, proposed for the forthcoming Fiscal Year.

Uranus observations were concentrated in three filters only - #1 (λ6000Å), #2(λ6200Å), and #3(λ6400Å). Limb-brightening was predicted for filter #2; limb-darkening for filters #1 and #3. Reliable area-scanning of the Uranus disk was carried out on three individual nights. In every case, observing conditions were less than optimum. The "seeing" (~2 arc sec.) was worse than usual for Flagstaff. In addition, some observations were made through thin, high, cirrus clouds. Throughout, the 200 μm aperture (1".3 diameter) was used, together with a 1-second scan speed. Integration times in the range 5-100 seconds were used. The observational technique is described by the following sequence of filter numbers: 1232123212321 etc.

4. Data Analysis

Data obtained during each night were analyzed using the Lowell Observatory computer facilities. In view of the "seeing" quality, Gaussian curves were found to provide the most satisfactory fit to the observed profiles over the Uranus disk. Immediately, an extraordinary effect was noticed. In the case of filter #2 (λ6200Å), the 1/e-width was consistently 2-5 percent wider than for either of the adjacent filters, #1 (λ6000Å) and $3 (λ6400Å). The discrepancy becomes more significant, the better the "seeing". The apparent widening of the Gaussian profile can be explained only by relative limb-brightening. For the effect to show even under mediocre observing conditions, it must be very prominent in the unsmeared Uranus image.

Fig. 2 illustrates relative limb-brightening at λ6200Å. Data were taken on 1974 June 5. Normalized radial profiles of Uranus are shown for filter #2, and for the mean of filters #1 and #3. To reduce the influence of "seeing" broadening, maximum time resolution was used. Integration times for the individual scans were limited to 5 seconds only. Ten scans were summed to obtain the filter #2 profile; nine and seven, to obtain the profiles of filters #1 and #3, respectively. Error bars overlying the mean of the filter #1 and #3 profiles indicate the relative consistency of the two individual curves.

5. Concluding Remarks

Two major results were obtained:

1. Indication of limb-brightening in the deep λ6190Å CH_4 band, in qualitative agreement with predictions by Belton and Price (1973, Astrophysical J. 179, 965).

2. Satisfactory demonstration of the ability of the Franz area-scanner to completely investigate the variation with wavelength of the limb-darkening/brightening phenomenon on Uranus.

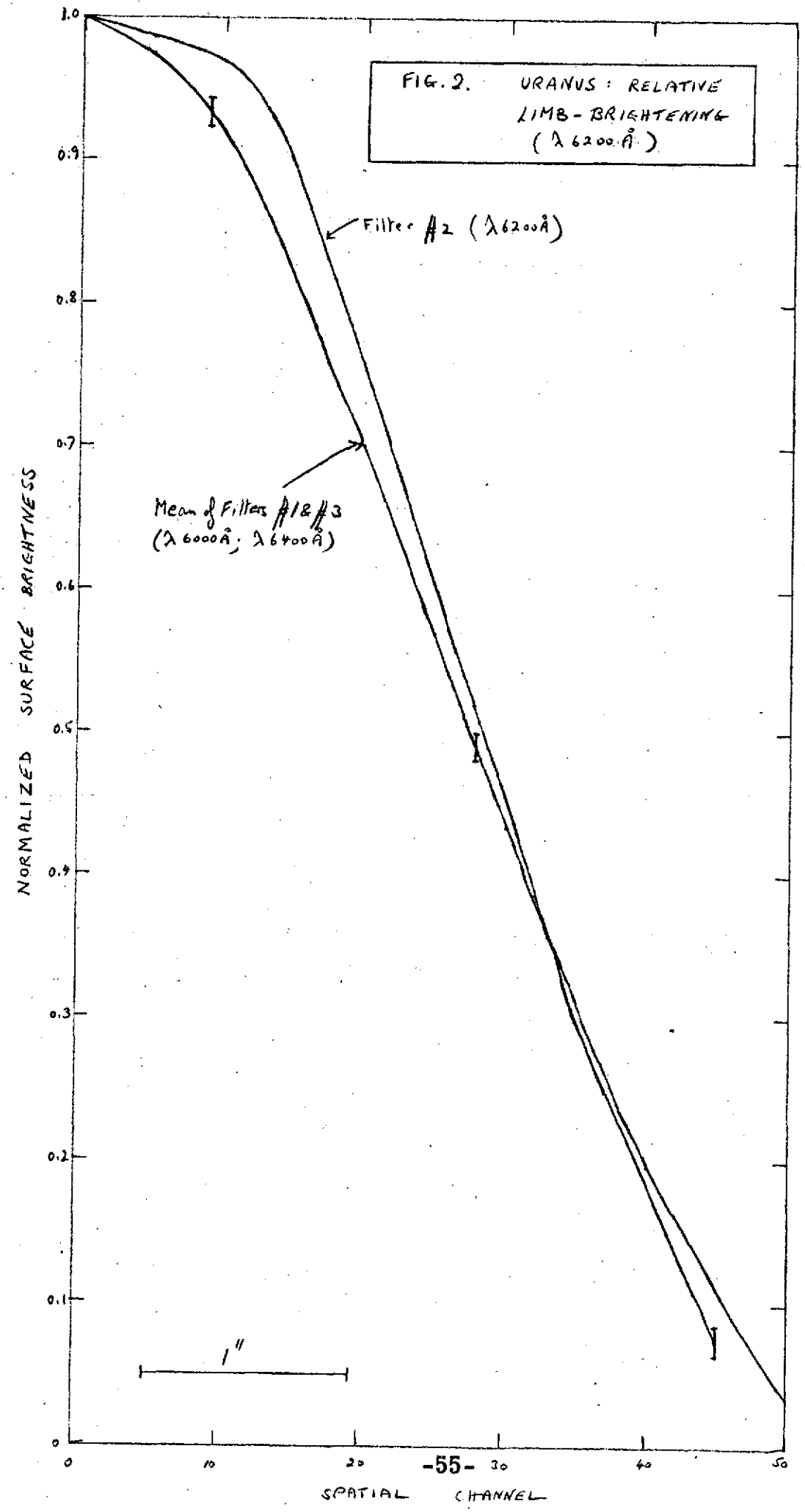
FIG. 2. URANUS : RELATIVE LIMB-BRIGHTENING (λ 6200 Å)
Filter #2 (λ6200Å)
Mean of Filters #1 & #3 (λ 6000Å ; λ 6400 Å)
1"
NORMALIZED SURFACE BRIGHTNESS
SPATIAL CHANNEL
1.0
0.9
0.8
0.7
0.6
0.5
0.4
0.3
0.2
0.1
0
0
10
20
30
40
50